CHARACTERIZATION OF RESIDUAL STRESSES IN BIREFRINGENT MATERIALS APPLIED TO MULTICRYSTALLINE SILICON WAFERS

A Dissertation
Presented to
The Academic Faculty

By

Kevin Skenes

In Partial Fulfillment
Of the Requirements for the Degree
Doctor of Philosophy in the
School of Mechanical Engineering

Georgia Institute of Technology

December, 2014

CHARACTERIZATION OF RESIDUAL STRESSES IN BIREFRINGENT MATERIALS APPLIED TO MULTICRYSTALLINE SILICON WAFERS

Approved by:

Dr. Steven Danyluk, Chair
School of Mechanical Engineering
Georgia Institute of Technology

Dr. Shreyes Melkote
School of Mechanical Engineering
Georgia Institute of Technology

Dr. Peter Hesketh
School of Mechanical Engineering
Georgia Institute of Technology

Dr. William Wepfer
School of Mechanical Engineering
Georgia Institute of Technology

Dr. Laurence Jacobs
School of Civil and Environmental Engineering
Georgia Institute of Technology

Dr. Ajeet Rohatgi
School of Electrical and Computer Engineering
Georgia Institute of Technology

Date Approved: October 15, 2014

ACKNOWLEDGEMENTS

I would first like to express my sincere gratitude to my adviser, Dr. Steven Danyluk, and his continued support of the research necessary for this dissertation. I also would like to acknowledge and thank the other members of my committee for their help and commitment: Dr. Shreyes Melkote, Dr. Peter Hesketh, Dr. William Wepfer, Dr. Laurence Jacobs, and Dr. Ajeet Rohatgi.

I am also indebted to all of my lab and office mates, particularly Guru Prasath and Arka Kumar, for their help with my research and for many excellent conversations over countless topics. Special thanks go to Fang Li for passing on his knowledge about the photoelasticity project.

Finally, I have the greatest appreciation for my parents, my sister Carol, and my wife Krista, all of whom provided endless encouragement, support, and love through the entire process.

TABLE OF CONTENTS

LIST OF TABLES

LIST OF FIGURES

LIST OF SYMBOLS AND ABBREVIATIONS

σ_1, σ_2	Largest and smallest in-plane principal normal stresses
σ_x, σ_y	Normal stresses in the x and y direction
τ	Shear stress
τ_{max}	Maximum shear stress
τ_{yx}	Shear stress in the yx plane
δ	Phase retardation (isochromatic)
θ	Isoclinic angle (isoclinic)
t	Effective material thickness
n	Index of refraction
V_0	Speed of light in a vacuum
λ	Wavelength of incident light
C	Relative stress-optic coefficient
h	Planck's constant
ω	Incidence angle of beam during X-ray diffraction
a_0	Atomic lattice constant
I_i	Photoelastic intensity of the i^{th} image
I_b	Intensity of background light
I_a	Photoelastic intensity with all optic axes parallel
k	Size of pixel neighborhood used in determining data quality
E	Young's modulus
ν	Poisson's ratio
C_{ij}	Elastic constant

NIR	near-infrared
EFG	edge-defined film-fed growth
CZ	Czochralski
FCC	face-centered cubic
XRD	X-ray diffraction
PV	Photovoltaic
mc-Si	multicrystalline silicon
EOS	Electro-Optical System
JPEG	Joint Photographic Experts Group
ISO	International Standards Organization
PET	polyethylene terephthalate
RMS	root mean square

SUMMARY

The purpose of this research was to further develop the understanding of birefringence as it relates to stress in thin crystalline materials. Crystalline silicon was chosen as a model material for the study. Improvements in data acquisition coupled with the silicon characterization provide a better understanding of stress phenomena.

Prior research has established the efficacy of the near-infrared polariscope as a non-destructive evaluation tool for measurements of stress in silicon. In this thesis, data acquisition and processing methods were improved to reduce noise and provide a more accurate evaluation of photoelastic parameters. Crystallographic anisotropy was included and stress optic coefficients were measured in multicrystalline silicon wafers. Grain orientation identification based on transmission intensity was used to assign appropriate stress-optic coefficients to grains of three crystallographic orientations. The correlation of transmitted intensity perpendicular to the planar atomic density was shown to be {111} orientations were found to have a lower light transmission than orientations such as {311}, which were found to have a higher light transmission intensity. A 10-step phase stepping technique was used to reduce isoclinic oscillation between $\pi/4$ and $-\pi/4$ by 60%. The shear-difference stress separation method was adapted to quality-guided integration, and zero-stress points were identified as acceptable boundary conditions for integration starting points.

Validation of the experimental methods and analytical techniques was done by imposing pre-determined stresses in the silicon surface by indentation. Vickers indentations in single-crystal Czochralski (CZ) wafers were found to create stressed

zones roughly 1.2 mm in diameter after a 2 N applied load. Measured stress levels in the indentation zones averaged between 20 and 25 MPa, in line with analytical calculations and a significant increase from residual stresses of 2-3 MPa typical of a CZ wafer. Indentations grouped in 2-D arrays also formed a larger secondary stress field around the array. The percentage of highly stressed wafer area outside of the array was found to behave according to the relationship $A = -39x + 117$, where A is the affected wafer area and x is the spacing between indentations. The increased levels of residual stress in these high-stress areas were defined through the relationship $\Delta\tau_{max} = -2.9x + 9.4$, where $\Delta\tau_{max}$ is the stress increase in MPa from unstressed levels.

Interactions between indentations and grain boundaries were also investigated by placing Vickers indentations in specific grains and measuring the resulting stress fields. Stress fields caused by the indentations extended to and were arrested by the grain boundaries, and ranged from 5-25 MPa in magnitude. Shear stress levels at grain boundaries were consistently raised or lowered by 15-20 MPa, implying that grain boundaries contain tensile and/or compressive stresses. This behavior was consistent regardless of proximity to the nearest indentation and the number of indentations placed in the grain.

Low-angle grain boundary theory predicts grain boundary stresses very close to the levels measured by the NIR polariscope. Comparison to several different types of contact theory explained the magnitude of the stresses in the Vickers indentations, but none predicted stress fields larger than 300 μm in diameter. Analytical and empirical evidence indicates a complex relationship governing residual stresses in silicon.

CHAPTER 1
INTRODUCTION

This thesis develops and expands the use of birefringence as a nondestructive residual stress evaluation tool for thin, flat, non-metallic materials by the analysis of transmitted light through the thickness. Stresses in the material result from frozen-in stresses during solidification and damage resulting from thermo-mechanical processing. Tensile stresses coupled with cracks can be a source of catastrophic failure of these materials. Of particular interest are stresses in anisotropic crystalline solids, where cracks can propagate long distances beyond the initiation sites at very low stresses. A study of crack propagation due to stresses is of special interest in multicrystalline silicon used in photovoltaic (PV) devices. PV cells are fabricated from multicrystalline wafers subject to thermal gradients during solidification and thermo-mechanical stresses during the manufacturing process.

This thesis begins by describing prior work at Georgia Tech and other labs, from which a near-infrared (NIR) polariscope capable of studying the relationship of birefringence and stresses in silicon has been developed. Figure 1-1 presents a flow chart of the thesis components and direction. Chapter 2 of this dissertation describes the background including the phenomena of birefringence and photoelasticity, which are expanded on in detail in Chapter 3. Research objectives are laid out in Chapter 4. Identification of crystallographic orientation by transmission intensity is introduced in Chapter 5. The stress-optic material coefficient of silicon varies with crystallographic orientation, and quick identification using transmission intensity allows for accurate stress evaluation. Chapter 6 describes a new phase shifting method for data acquisition

which was adapted to reduce noise and improve data quality. Separation of τ_{max} into the normal stress components σ_x and σ_y is discussed in Chapter 7. Stress separation was accomplished using a novel quality-guided integration scheme. Furthermore, new boundary conditions were developed to provide integration starting points which do not require a free boundary.

Chapter 8 addresses residual stresses in silicon wafers. Correlations were found between residual stresses and manufacturing parameters such as method of wafering and growth rate. These findings were corroborated by fracture strength tests. Highly localized stresses were found at grain boundaries and around Vickers indentations. These stresses of single indentations and the interaction between multiple indentations were studied. It was found that indentations placed in close proximity create a larger stress field which surrounds all indentations. Indentations near grain boundaries imposed stress fields which did not extend beyond the grain boundary but increased the stress level in the grain boundary itself. Chapter 9 compares the experimental results with grain boundary theory and linear elastic mechanics. Finally, Chapter 10 summarizes the thesis.

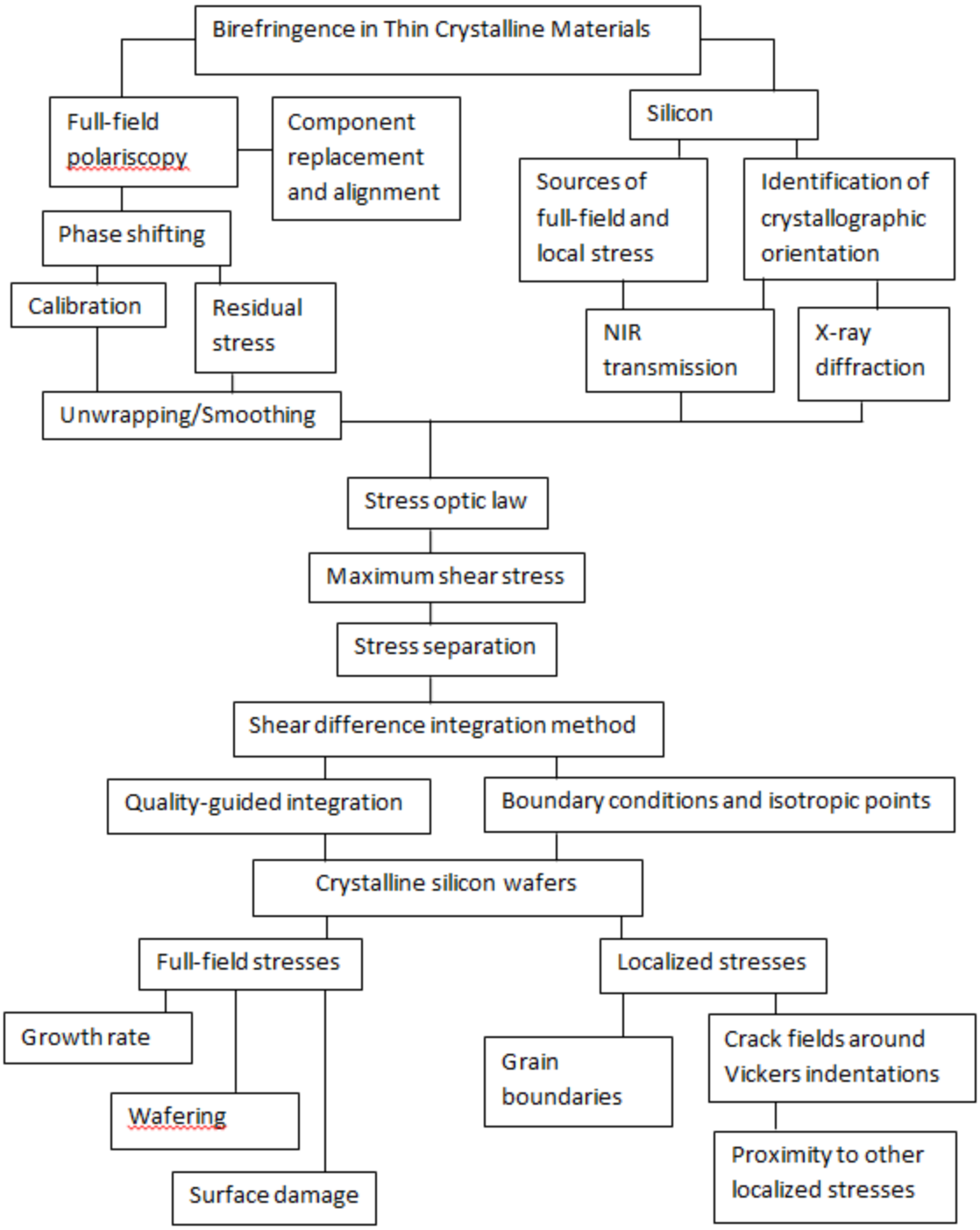

Figure 1-1: Research flowchart.

CHAPTER 2
BACKGROUND

2.1 Birefringence and photoelasticity

The phenomenon of birefringence in glass and transparent crystals under stress was first recorded in 1815 by Brewster [1], who found that a glass plate which was not birefringent would still exhibit doubly refracting behavior upon the application of body forces. Brewster also noted that changing the direction of the applied force altered the birefringence in relation to the optic axes of the doubly refracting glass. Neumann [2] and Maxwell [3] subsequently established in 1841 and 1853 the linear relationship between light propagating in solids as transverse waves and the transmission of linearly polarized light showing a phase retardation through a stressed medium. Coker and Filion successfully applied phase retardation principles to engineering-related problems in 1902 by using photoelastic principles to study structural engineering [4]. Birefringence at wavelengths beyond visible light was successfully tested by Bergman, Fues, Hidemann, and Hoesch in the late 1930s [5].

This prior work was eventually used to construct an optical system where linearly polarized light is transmitted through translucent solids under known stress. This tool through which the stress-induced birefringence of a sample may be measured is known as a polariscope. Linearly or circularly polarized light illuminates a sample, and the transmitted or reflected light is analyzed with subsequent optical components. Figure 2-1 is an illustration from Dally's textbook showing a sample in a plane polariscope.

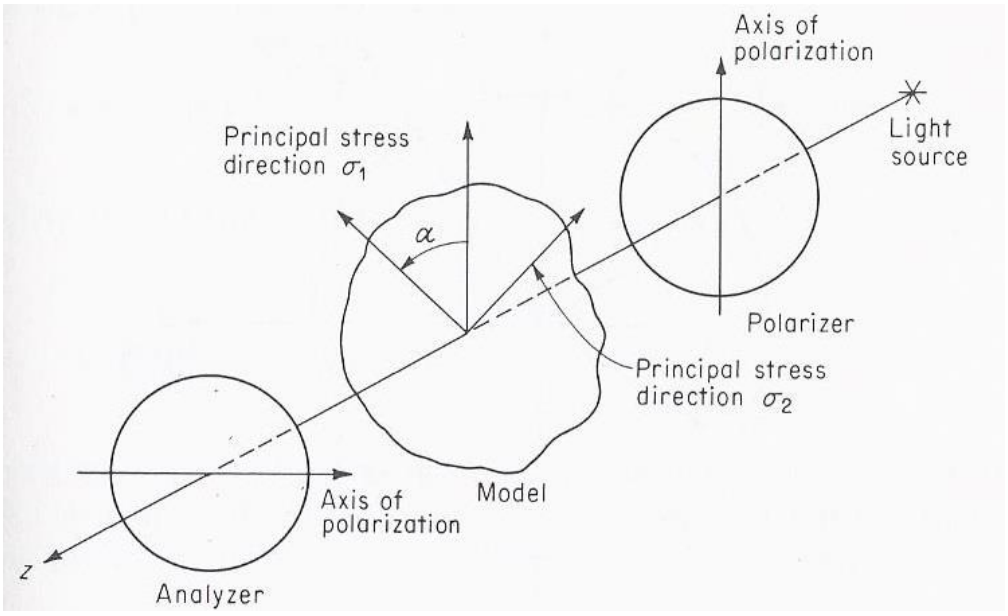

Figure 2-1: Sample in a plane polariscope. [6]

Referring to Figure 2-1, detection of the transmitted or reflected light may then be used to evaluate the stress state of the sample. An analysis of the transmitted light as a function of the angle between the polarizer and analyzer may be used to determine the phase retardation (δ) and isoclinic angle (θ), or isochromatics and isoclinics. These parameters represent the magnitude and direction of the maximum shear stress, respectively, and are illustrated below in Figure 2-2. Once the phase retardation and isoclinic angle are known, the stress optic law may be used to find the maximum shear stress.

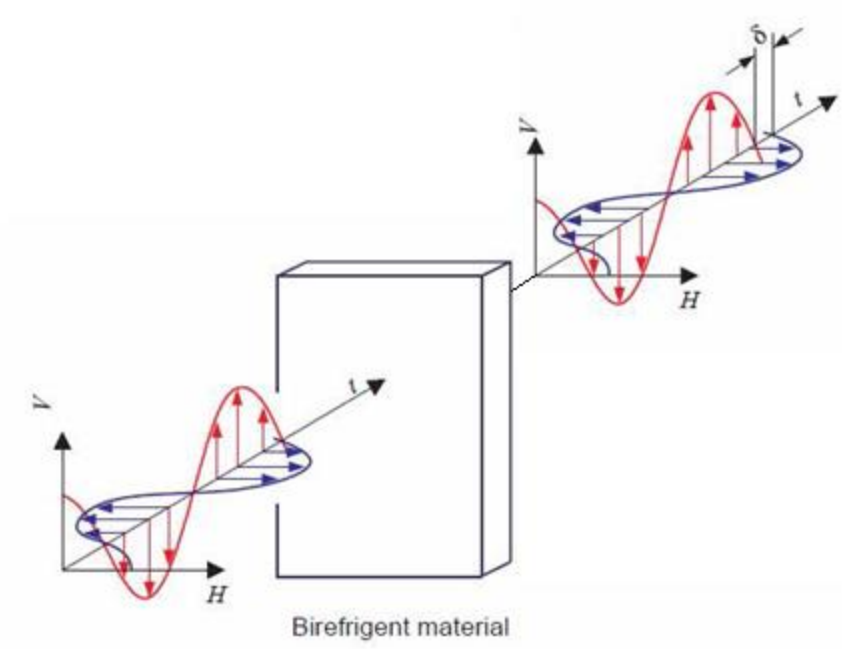

(a)

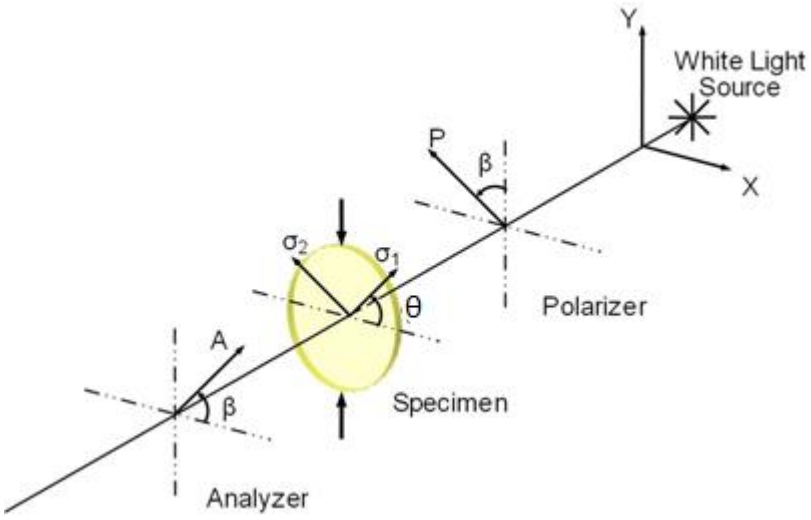

(b)

Figure 2-2: (a) Phase retardation δ, (b) Isoclinic angle θ.

Prior to the advent of digital image storage and processing, photoelastic parameters were extracted directly from the polariscope using fringe counting methods. This process required the identification of fringe centers and fringe edges, neither of

which are guaranteed to be well-defined. Improvements in photo-detector and video technology in the 1950s allowed for the capture and storage of photoelastic images. These images could then be analyzed through numerical post-processing for greater accuracy. Two types of polariscopes were developed: point polariscopes and full-field polariscopes. Point polariscopes use a point light source (such as a laser) and a light detector to scan a sample and produce a stitched image from multiple measurements. The light source in a full-field polariscope illuminates the entire sample. A CCD or CMOS camera is used to capture an image of the illuminated sample.

2.2 Photoelasticity in semiconductor materials

Researchers have been using photoelasticity to evaluate semiconductors since the 1950s. Silicon, while opaque to visible light, becomes transparent at wavelengths of roughly 1100 nm or greater. Near-infrared or broadband light sources may therefore be used to successfully analyze silicon through the use of a polariscope. Bond and Andrus were the first to use birefringence to characterize residual stresses in silicon in 1955 [7]. Lederhandler then discovered a correlation between etch pit density and residual strain [8]. The use of photoelasticity was further expanded to include other semiconductor materials such as GaP and GaAs by Dixon in 1967 [9].

Until 1980, residual stresses were defined only in terms of qualitative fringe measurements, which were useful for comparison between samples but unable to provide any sort of precise quantitative stress evaluation. Kotake et al. first obtained quantitative residual stress numbers in 1980 when investigating GaP ingots [10]. However, these results were dependent on the assumption of perfectly vertical or perfectly horizontal

principal stress directions, a stress state rarely seen outside of a tightly controlled environment.

Later, Date used a linear polariscope in 1992 to find residual stresses in GaAs wafers [11]. Liang et al. simultaneously studied the anisotropy of piezo-optic properties of silicon while examining the residual stresses caused by different processing techniques [12]. This relationship was explored further by Niitsu, who demonstrated the independence of retardation in silicon with respect to orientation [13]. Niitsu's work was followed by Danyluk's group, which constructed a full-field polariscope capable of fractional fringe analysis.

This work began with Zheng, who compared NIR transmission photoelasticity with shadow moiré analysis [14]. FEA optimization was used to extract residual stresses from thin silicon plates using phase stepping shadow moiré with a sensitivity of ~1 MPa. After finding that shadow moiré was sensitive to variations in the location of tensile and compressive stresses, a near-infrared transmission polariscope was developed as an alternative means to study local residual stresses in anisotropic thin plates. Phase stepping photoelasticity was used with a fringe multiplier to achieve a stress sensitivity of 0.8 MPa. Zheng concluded that NIR transmission photoelasticity was more promising for non-destructive stress evaluation based on ease of use and potential for improvement in spatial resolution.

Zheng's work was continued by He [15], who calibrated the fringe multiplier to minimize losses in light intensity and spatial resolution. He also began work on anisotropic stress coefficients, and derived the coefficients for {100}, {110}, and {111} crystalline silicon using in-plane 4-point bending. A new program for extracting stresses

from phase stepping images was written and residual stresses in EFG, string ribbon, cast, and CZ wafers were examined.

Li expanded on the capabilities of polariscopy as a residual stress characterization tool by further evaluating the stress-optic coefficients of different crystallographic orientations of silicon [16]. The maximum variation between coefficients was found to be ~1.7. The polariscope was rearranged to allow for examination of larger samples, and the fringe multiplier was removed after advances in system alignment and systemic error removal. A thermal model was used to estimate the stresses induced by the light source, which were negligible. Finally, stress separation via shear-difference integration was examined, and a solution for elimination of ambiguity at boundary conditions was proposed.

While stress separation by shear-difference integration was proven viable by Li, excessive noise accumulation remained problematic. Noise levels in the τ_{max} evaluation were high, and stress separation beyond a distance of a few millimeters was difficult. The shear-difference integration scheme also required a free boundary to satisfy initial boundary conditions, limiting the areas of a wafer which could be successfully analyzed. Additionally, the spatial resolution of the polariscope was only 200 μm, limiting studies of stresses around local features, and no solution was proposed for the assignment of appropriate stress optic coefficients to multicrystalline wafers.

2.3 Residual stress characterization methods

Residual stresses are generally characterized through two categories of evaluation: destructive and non-destructive. Destructive methods measure changes in

strain after releasing embedded residual stresses. The measured strains may be converted into residual stresses through Hooke's Law and linear elastic theory. While quite accurate, releasing the residual stress in a sample involves damaging the specimen in some way, typically rendering it unusable for any originally intended purpose. Methods for stress release include hole drilling, micro-indentation, and sub-critical annealing. None of these methods are particularly suitable for silicon, which is extremely brittle when subjected to drilling or indentation and oxidizes at temperatures required for annealing.

Non-destructive evaluation methods may be used for in-situ monitoring of manufacturing processes. The non-destructive nature of these methods does not affect the ability of the inspected sample to function in its originally designed capacity. The most prevalent non-destructive evaluation methods in the photovoltaic industry are currently X-ray diffraction, Raman spectroscopy, and near-infrared polariscopy. Each method has benefits and drawbacks which must be carefully weighed before selection of a particular process.

X-ray diffraction is described by Bragg's law of diffraction. Stress-induced changes in the crystal lattice structure of silicon cause atomic displacements which are measured by diffraction of an X-ray beam. Back Laue diffraction may then be used to characterize the strains present in the lattice. These strains are then converted into stresses using linear elasticity.

There are two primary disadvantages to X-ray diffraction as a residual stress detection tool. First, X-ray diffraction is a localized point technique. Full-field evaluation of a 156x156 mm PV silicon wafer may require hundreds of measurements,

each with an uncertainty of nearly 100 MPa. The computational cost of stitching the image together and the time necessary to complete such a large number of measurements are significant. Full-field evaluation of a single wafer can take longer than one hour to complete, which is unacceptable for *in-situ* evaluation and in-line inspection. The second disadvantage of X-ray diffraction is its inability to penetrate the wafer surface beyond roughly 30 μm, after which X-rays are almost entirely absorbed. PV silicon wafers are on the order of 200 μm thick, and residual stresses in the wafer interior cannot be detected using X-ray diffraction.

Raman spectroscopy is based on the inelastic scattering of monochromatic light after impinging upon a surface. Interaction with of the surface phonons creates a shift in the energy of the reflected light. This effect is named after Raman, who first discovered it in 1928 [17]. Practical applications of the theory were expanded by Placzek in the early 1930s [18]. Raman spectroscopy provides excellent spatial and stress resolution assuming phonon frequencies and displacements, but is essentially a point procedure, making full-field measurements time-intensive. It is also intended to be a surface detection technique, and results must be interpreted accordingly.

Near-infrared polariscopy is based on the principles of birefringence, where stressed crystalline structures split a single ray of incident light into two distinct rays. A series of images is acquired while systematically altering the wavelength of the incident light, the applied load on the sample, or the polarization state of the incident light. From these images, a system of equations based on the transmission intensity through the sample is used to solve for the isoclinic and isochromatic photoelastic parameters. Once these parameters have been determined, the maximum shear stress and its orientation

may be determined using the stress-optic law. This technique has been proven to be a good combination of low computational expense, low required time, and full-field capability.

2.4 Residual stresses in photovoltaic silicon wafers

Crystalline silicon is the primary source material for photovoltaic (PV) cells. PV modules are composed of 156x156 mm silicon wafers tiled together. Silicon is brittle, and PV silicon wafers are susceptible to breakage during the manufacturing process. Residual stresses present in these wafers can have a detrimental effect on their mechanical and electrical properties. These residual stresses often arise from thermal gradients which occur during wafer creation. While post-process treatment such as annealing can reduce these residual stresses, they cannot be completely removed [20]. Furthermore, the process of wafering, in which a cast or grown ingot is cut into wafers, has been found to induce residual stress on the surface of the silicon wafers [21].

Most silicon wafers are created through one of three processes. Single-crystal ingots are created via Czochralski (CZ) growth from a seed crystal, illustrated below in Figure 2-3.

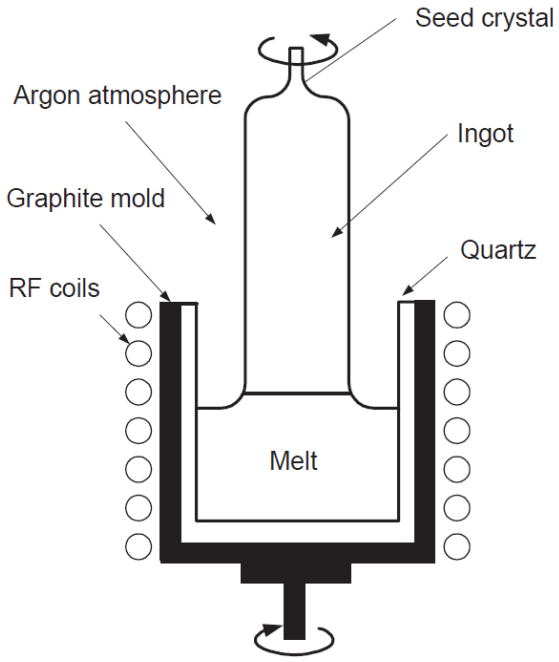

Figure 2-3: Diagram of Czochralski silicon growth process.

Multicrystalline silicon is cast as ingots or grown from the melt as wafers through the edge-defined film-fed (EFG) growth process. Multicrystalline cast ingots are created by pouring molten silicon into a crucible and allowing it to solidify. Figure 2-4 is an illustration of the casting process.

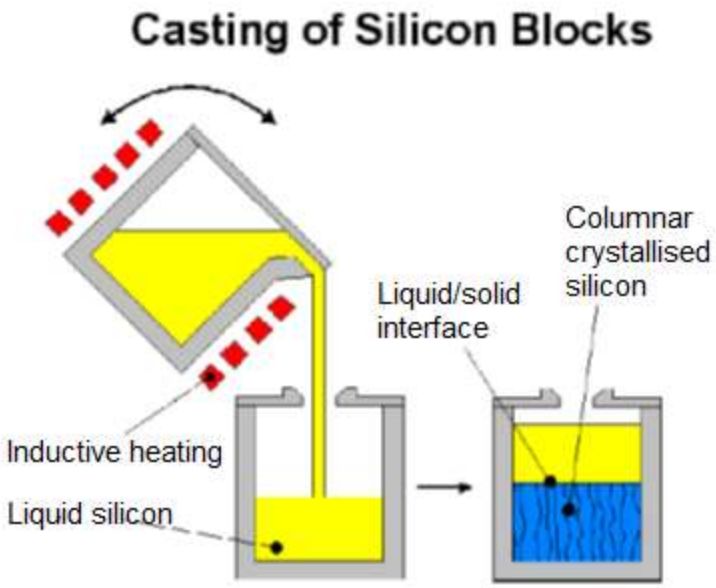

Figure 2-4: Casting of silicon ingots. [19]

Multicrystalline EFG wafers are grown as a thin ribbon from a melt. The EFG process is illustrated below in Figure 2-5.

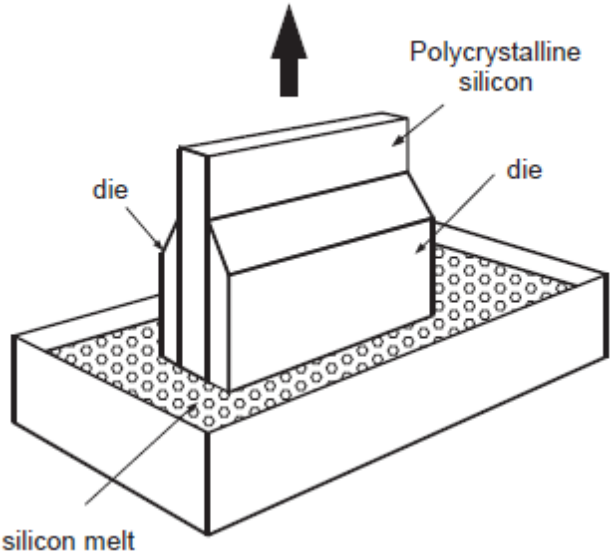

Figure 2-5: Diagram of EFG silicon growth process.

Kalejs et al. found that thermal gradients inherent in these manufacturing processes may result in residual stresses [22]. Furthermore, cast and CZ ingots must be sliced into wafers through what is commonly a wire sawing process such as the one shown in Figure 2-6. Yang et al. demonstrated that surface damage created during wafering can result in residual stresses which affect the mechanical strength of the wafer [21].

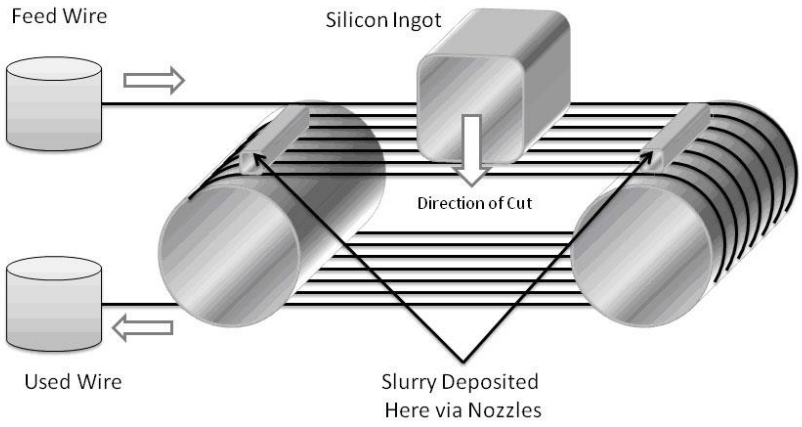

Figure 2-6: Silicon ingot cut into wafers through wire sawing. [23]

While Figure 2-6 shows slurry being deposited onto the wire, industry standard has recently been trending toward fixed-abrasive diamond wire sawing.

Furthermore, Garcia and Danyluk have shown a correlation between etch pit density, residual stress, and electrical efficiency of the completed solar cell. The relationship between dislocation density and residual stress in EFG wafers was found by Garcia to be a negative square root relationship, and stress relaxation is indicated by critical dislocation densities between $1x10^5$ and $3x10^5$ [24]. Finally, Skenes, Li, and Danyluk have found high concentrations of residual stress near grain boundaries and hard

inclusions present in the wafer [25]. Residual stress fields accompanying the crack networks created by Vickers indentations have also been detected [26].

CHAPTER 3
UNDERLYING PHYSICAL PRINCIPLES

3.1 Behavior of light

Maxwell's equations lay the foundation for the interaction of electromagnetic radiation with solids [27]. Study of the propagation of light through a medium led to Maxwell's conclusion that light is an electromagnetic disturbance which is propagated through a field according to certain electromagnetic laws. Furthermore, an electromagnetic radiation passing through a non-conducting field was found to only propagate those disturbances transverse to the direction of propagation. The propagation of light through a medium can therefore be characterized as a collection of electromagnetic disturbances which are transverse to the direction of propagation.

The velocity of light in a medium is described as follows,

$$V = \frac{1}{n} V_0 \tag{1}$$

Where V_0 is the speed of light in a vacuum and n is the index of refraction of the medium. The index of refraction of an optically anisotropic material varies with propagation direction or polarization state. Light passing through an optically anisotropic material will therefore pass through at different speeds based on the direction of propagation or the polarization state of the light.

The phenomenon of birefringence is based on this behavior of light propagating through an optically anisotropic material. If the optical anisotropy is based on the direction of propagation, two rays with a lateral offset are created. Calcite, an optically anisotropic material, displays two instances of each black line in Figure 3-1.

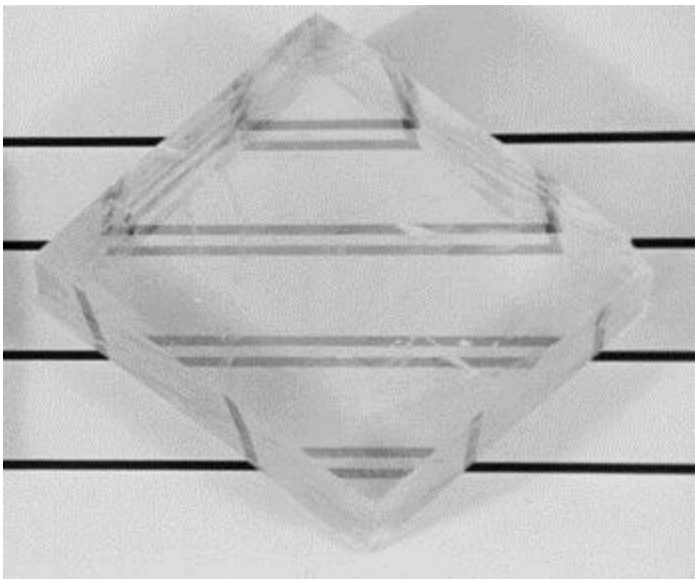

Figure 3-1: Optically anisotropic behavior of calcite.

The two rays created due to the anisotropy are known as the ordinary and the extraordinary ray. The ordinary ray remains constant along the original path of the incident light, while the location of the extraordinary ray is dependent on the crystal's physical orientation. The behavior of laterally shifted extraordinary rays is shown in Figure 3-2.

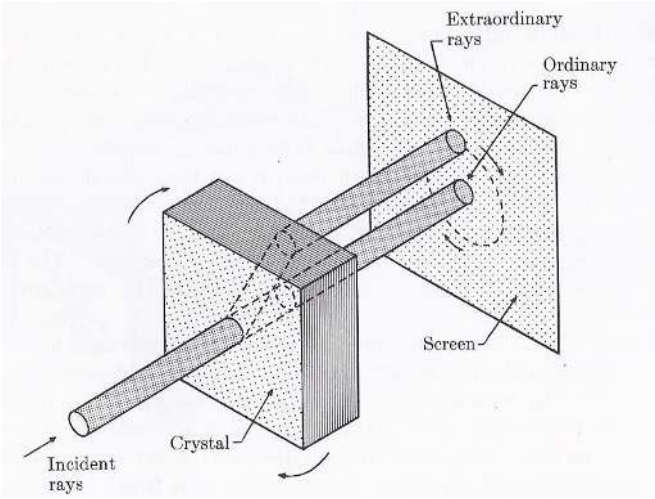

Figure 3-2: Behavior of laterally shifted ordinary and extraordinary rays. [28]

Incident light which is parallel with or orthogonal to the optic axis of the material will not create a laterally shifted extraordinary ray. Rather, the ordinary and extraordinary rays will travel along the same path at a different phase velocity, creating a retardation between the two rays when they exit the material. Figure 3-3 demonstrates the retardation between electricity and magnetic field waves as they travel through space, enter a dielectric material, and exit.

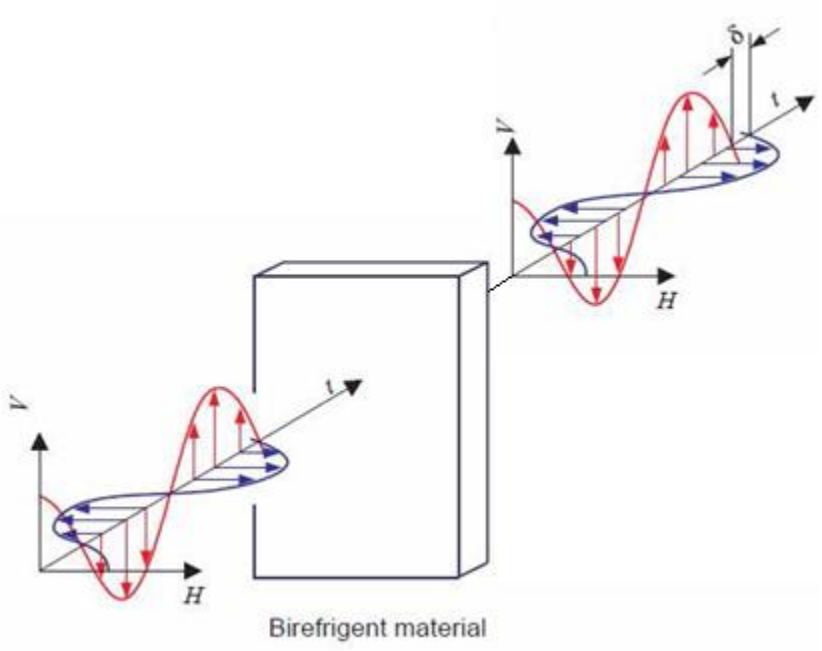

Figure 3-3: Behavior of phase retardation caused by optical anisotropy.

The same behavior is occurs when a ray of light passes through a birefringent medium parallel or orthogonal to its optic axis. No lateral shift occurs between the ordinary and extraordinary rays. Each ray passes through at a different velocity, resulting in a phase retardation δ after propagation through the material.

3.2 Behavior of polarized light

Common broadband light emitted from a source such as an incandescent light bulb contains transverse vibrations of electrical charges in many random directions relative to the propagation direction as shown in Figure 3-4.

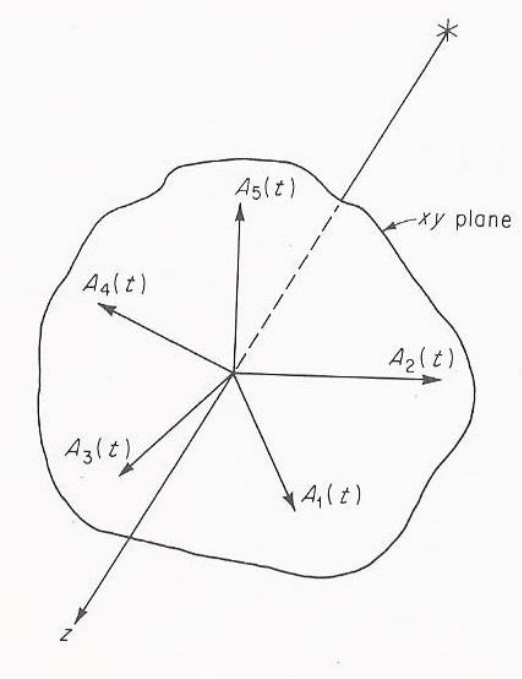

Figure 3-4: Sample transverse vibrations in light propagation. [6]

Polarized light is light in which the electrical field is resolved in one specific direction. The transverse electric field vector oscillates along a single line at all points of any plane such as the one illustrated in Figure 3-4, and is said to be linearly polarized. A polarizer is an optic element which absorbs the transverse components of a light vector that are not in line with its optic axis. If the beam of light in Figure 3-4 is directed through a polarizer whose optic axis is aligned with the A_5 direction, vector components in all other directions will be absorbed while vibrations in the A_5 direction pass through. The principle is illustrated in Figure 3-5.

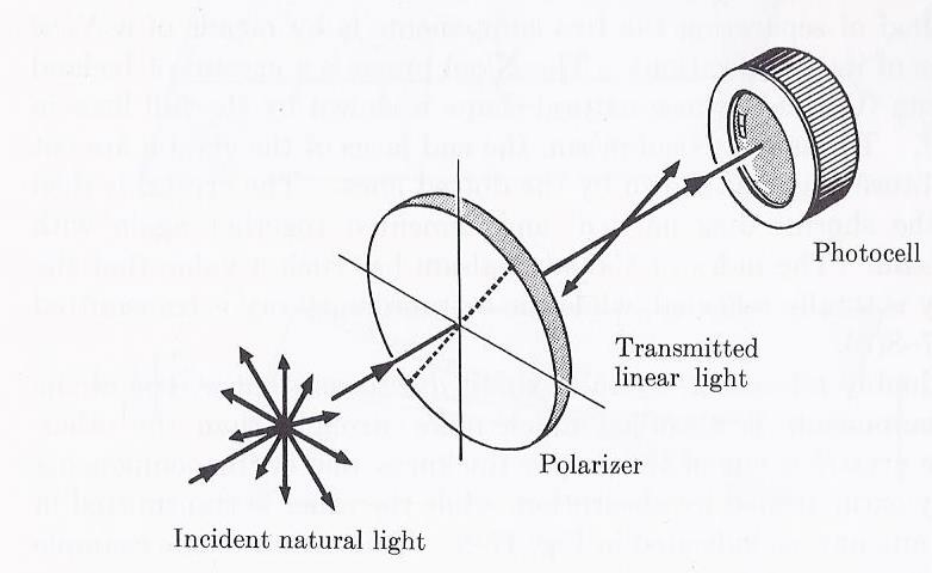

Figure 3-5: Passage of broadband light through a polarizer. [28]

Analysis of light transmission through a polarizer as shown in Figure 3-5 requires knowledge of the angular position of the optic axis. The polarization orientation of the polarizer in Figure 3-5 is represented as a dotted line. Light which passes through the polarizer will be resolved in the direction of the dotted line in Figure 3-5. The fraction of any one transverse vibration which will be transmitted or absorbed can be determined using analysis represented in Figure 3-6.

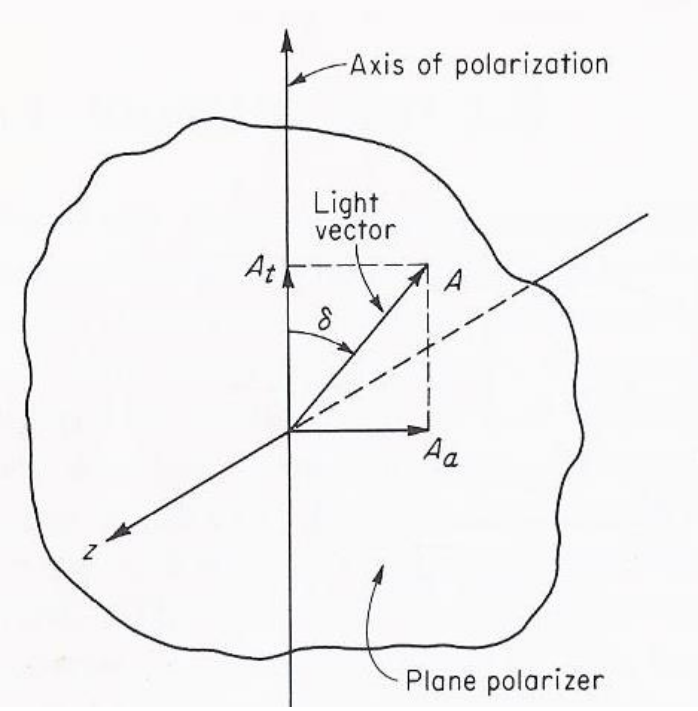

Figure 3-6: Behavior of light passing through a plane polarizer. [6]

Here, A_a is the portion of the vector A which is absorbed, and A_t is the portion which is resolved along the optic axis and transmitted. Each vector may be calculated using the following relationship:

$$A_a = A \sin \delta \tag{2}$$

$$A_t = A \cos \delta \tag{3}$$

The variable δ represents the angle between the optic axis of the polarizer and the transverse vibration concerned. The passage of light through multiple polarizers in series can be similarly predicted. Two polarizers whose optical axes are perpendicular ($\delta = \pi/2$) will allow no light to pass through, as indicated by Equation (3).

Circularly polarized light rotates about the propagation path as shown in Figure 3-7. The single vibration found in linearly polarized light now rotates in a circular helix as it propagates.

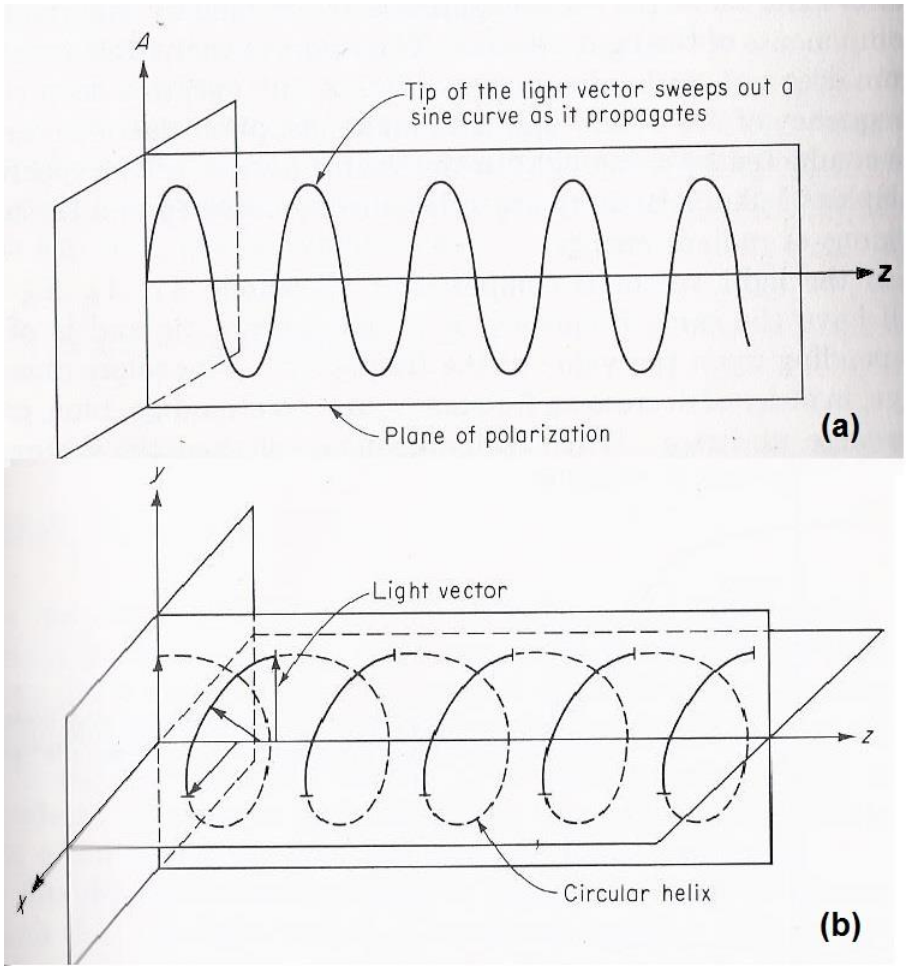

Figure 3-7: Propagation of (a) linearly polarized and (b) circularly polarized light. [6]

Creating circularly polarized light requires a polarizer and a doubly refracting plate. A doubly refracting plate contains two optic axes known as the fast axis and the slow axis. Light propagates along the fast axis at a speed c_1 which is greater than c_2, the

speed at which light travels along the slow axis. Figure 3-8 is a diagram of light passing through a doubly refracting plate.

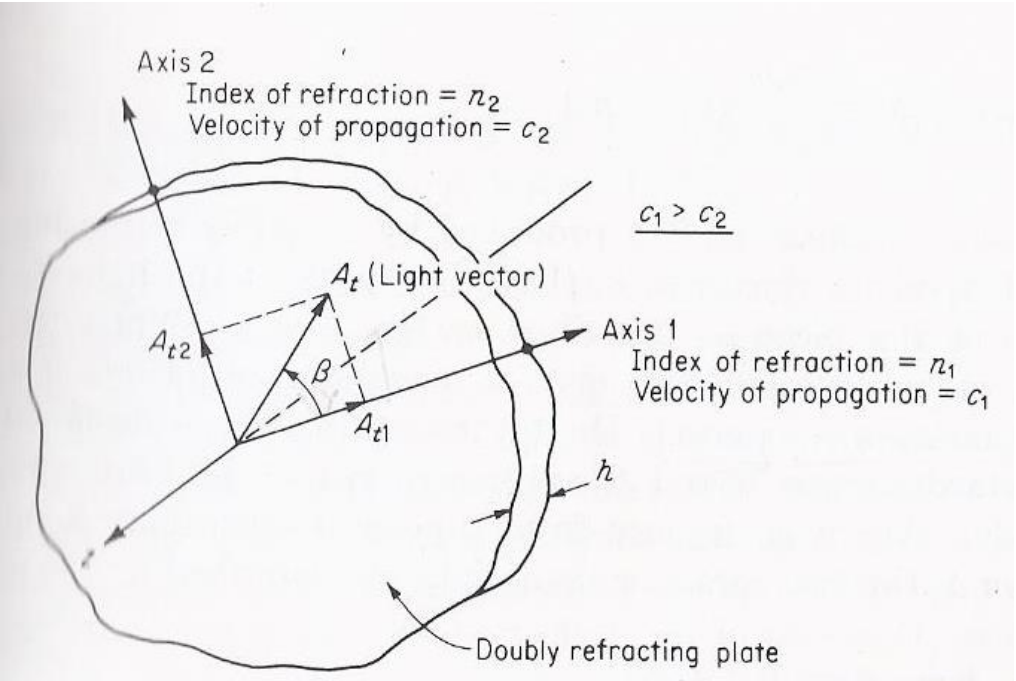

Figure 3-8: Light passing through a doubly refracting plate. [6]

Light entering the doubly refracting plate must be linearly polarized for circularly polarized light to exit. The individual components of the beam after passing through may be evaluated by the following, where δ is the angle represented in Figure 3-6.

$$A_{t1} = A \cos\delta \cos\beta \tag{4}$$

$$A_{t2} = A \cos\delta \sin\beta \tag{5}$$

Moreover, due to the difference in speed between c_1 and c_2, a phase shift is introduced between the vectors A_{t1} and A_{t2}. This relative phase shift or retardation δ or Δ is shown below in Figure 3-9.

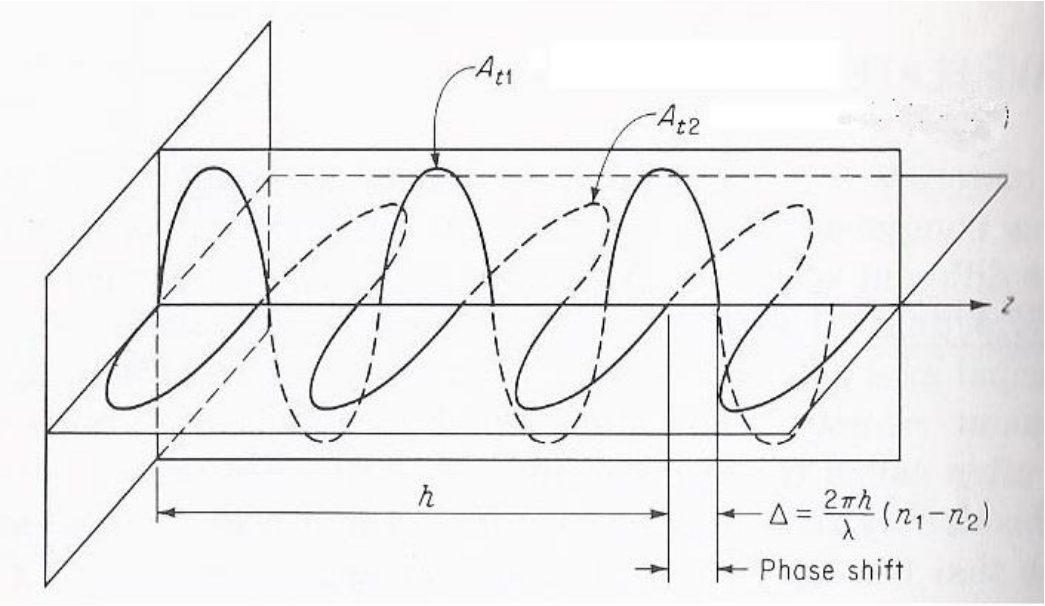

Figure 3-9: Phase shift or retardation introduced by doubly refracting optics. [6]

Doubly refracting plates are identified by the magnitude of the created phase shift. A plate designed to give an angular retardation of π/2 is known as a quarter waveplate, while plates designed to create angular retardation of π and 2π are respectively known as half waveplates and full waveplates.

To create circularly polarized light with a polarizer and a quarter waveplate, the angle β between the polarization axis of the polarizer and the fast axis of the quarter waveplate is π/4. This arrangement creates a light vector with constant amplitude whose angle of emergence increases with time *t*. Thus, as light propagates along the z-axis, the tip of the light vector sweeps in a circular helix along the propagation path.

3.3 Stress-optic law

Maxwell was also the first to relate the stress state of a material to its index of refraction [3]. A material in its unstressed state exhibits an index of refraction n_0 which

is uniform at all points. The introduction of a two-dimensional stress state changes the optical properties of the medium, which becomes doubly refracting or birefringent and behaves in a manner similar to the wave plates discussed in the previous section.

Furthermore, the principal axes of stress at any point in the material become the fast and slow axes of the now doubly refracting medium. Maxwell deduced that the changes in the indices of refraction were linearly proportional to the stresses induced and followed the relationships

$$n_1 - n_0 = c_1\sigma_1 + c_2\sigma_2 \tag{6}$$

$$n_2 - n_0 = c_1\sigma_2 + c_2\sigma_1 \tag{7}$$

Where n_1 and n_2 are the indices of refraction along the two principal axes of σ_1 and σ_2. The material constants c_1 and c_2 are known as the stress optic coefficients, and the quantities $c_1\sigma_1$ and $c_2\sigma_2$ represent strains. Changes in atomic displacement modify the electron positions and vibrations and allow for the quantification of these strains, which are then converted to stresses using the stress optic coefficients. The third principal stress σ_3 is assumed to be negligible. Subtracting the two equations to eliminate n_0 results in the following:

$$n_1 - n_2 = (c_1 - c_2)(\sigma_1 - \sigma_2) \tag{8}$$

Recalling the material now behaves like a waveplate, the difference between the refractive indices $n_1 - n_2$ can also be characterized as

$$n_1 - n_2 = \frac{\lambda}{2\pi t}\delta \tag{9}$$

Where λ is the wavelength of the incident light, t is the sample thickness, and δ is the phase retardation illustrated in Figure 3-9. Combining Equations (8) and (9) and

substituting the relative stress optic coefficient C for the quantity $c_1 - c_2$ results in the stress optic law as it is commonly implemented:

$$|\sigma_1 - \sigma_2| = \frac{\lambda}{2\pi t C}\delta \tag{10}$$

The difference $|\sigma_1 - \sigma_2|$ is the absolute value of the difference between the largest and smallest principal stresses, and can be represented as the single term $2\tau_{max}$. The relationship between these parameters is readily obtained by drawing Mohr's Circle for a two-dimensional stress state.

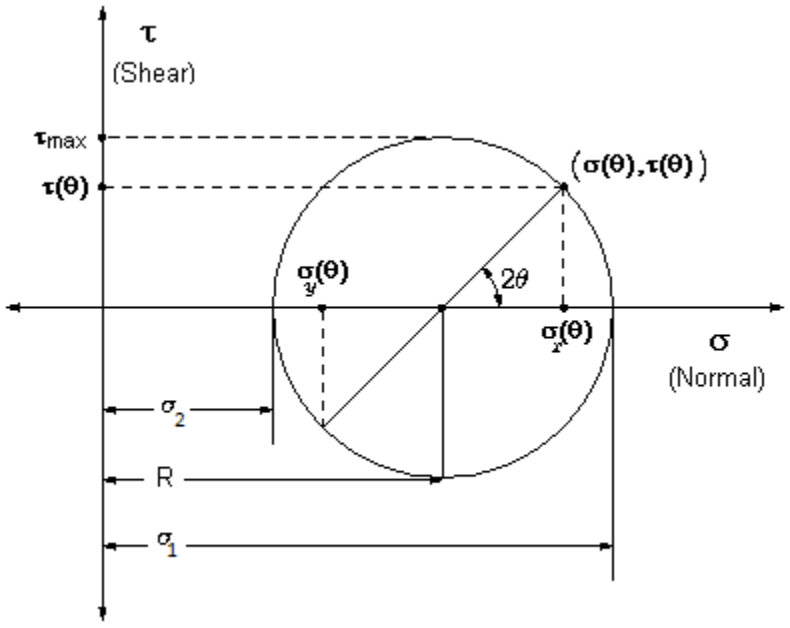

Figure 3-10: Mohr's Circle stress analysis.

Note the relationship between σ_1, σ_2, and τ_{max}. The stress-optic law provides the value of τ_{max}, or the radius of the circle. The angle θ is the isoclinic angle and is evaluated directly through the polariscope. Information about the values of σ_1, σ_2, σ_x, and σ_y is more difficult to obtain. Numerical integration schemes are helpful in the separation of τ_{max} into the normal stress components σ_x and σ_y and will be discussed later.

3.4 Evaluation of photoelastic parameters

To accurately obtain the isochromatic and isoclinic photoelastic parameters, more than one image of the sample must be acquired. Recent research has focused on four methods: spectral analysis, Fourier transform analysis, load stepping, and phase stepping. Spectral content analysis was first introduced by Redner in 1984 [29], who used the color of light transmitted through the specimen to find stress-related phase retardation. However, spectral analysis requires a precisely calibrated light source and optical arrangement, and is limited to a point procedure. Quan and Morimoto independently proposed FFT analysis processes in 1993 [30] and 1994 [31]. Quan's method is only capable of providing isochromatic data, while 90 images are required for use of Morimoto's technique. Fourier transform techniques are also more computationally expensive than others available for photoelastic analysis. Load stepping involves applying a known series of stresses to the sample, and was developed by Ng in 1997 [32]. While accurate, this procedure is by nature not conducive for applications involving non-contact *in-situ* residual stress measurement.

Hecker and Morche introduced the phase shifting concept in 1986 [33]. Five years later, Patterson and Wang developed an algorithm based on a circular polariscope which allowed for the complete evaluation of isoclinic and isochromatic values for every point (pixel) in the spatial domain of the sample [34]. Ramji and Ramesh next developed a ten-step algorithm based on a mixed polariscope in 2008 [35]. Prasath and Skenes recently analyzed the difference between the most recent two methods and found the Ramji and Ramesh technique to be superior to Patterson and Wang in terms of quality of

data [36]. Phase shifting is the method of choice for the purposes of this research, as it is not excessively computationally expensive, takes a reasonable amount of time, and is easily full-field capable.

3.5 Near-infrared transmission through silicon

As light passes through a crystalline semiconductor, photons with a wavelength shorter than the material's band gap are absorbed and converted to charge carriers while other wavelengths are transmitted. The band gap is the energy difference between the top of the valence electron band and the bottom of the conduction band, and is illustrated below in Figure 3-11. This difference is the amount of energy required to move a valence electron into the conduction band.

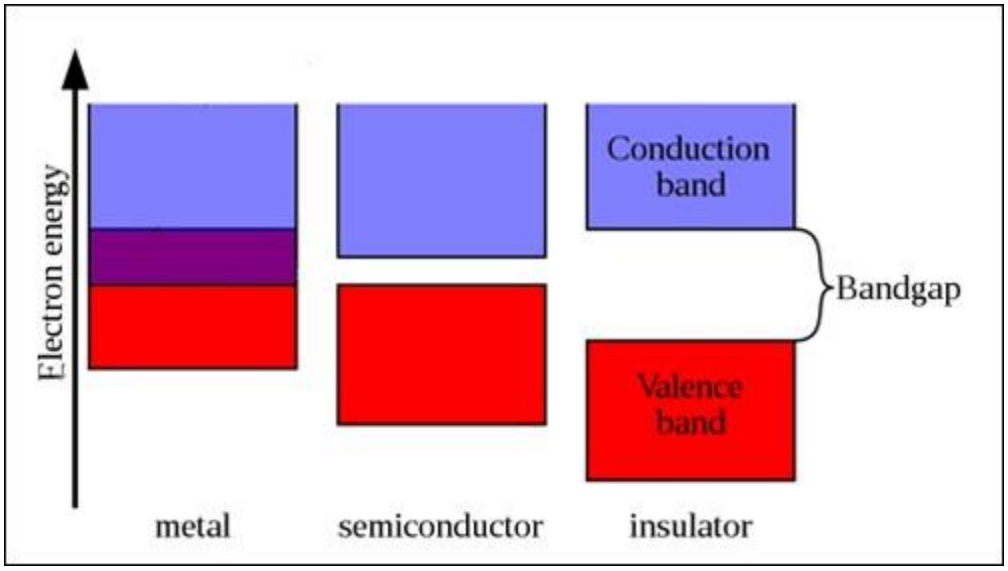

Figure 3-11: Band gap comparison between materials.

Crystalline silicon has a band gap of approximately 1.1 eV at room temperature. The relationship between the energy of a photon and its wavelength is characterized by

$$E = \frac{hc}{\lambda} \tag{11}$$

Where h is Planck's constant and c is the speed of light.

Photons with an energy level equivalent to the band gap of crystalline silicon are characterized by a wavelength of roughly 1.1 μm. Thus, silicon is opaque to ultraviolet and visible light but has a transmission ratio of about 50% starting at a wavelength of around 1100 nm. The transmission spectrum of silicon is shown below in Figure 3-12.

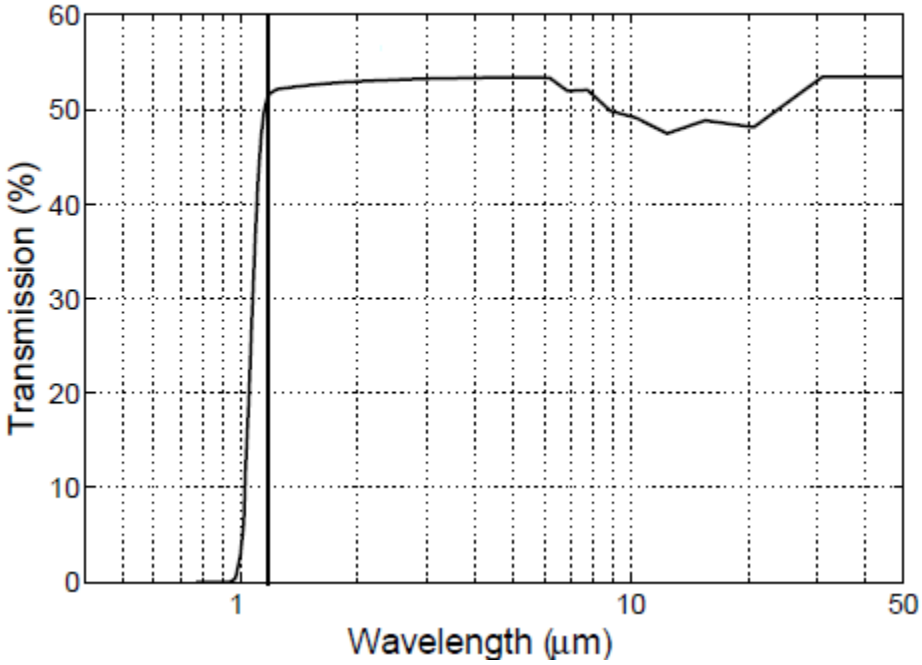

Figure 3-12: Transmission spectrum of silicon.

An operational wavelength of 1150 nm was chosen for the experiments performed in this research. This was achieved with a broadband light source and band pass filters.

3.6 Experimental setup

A schematic of the experimental setup used for the research in this dissertation is presented below in Figure 3-13.

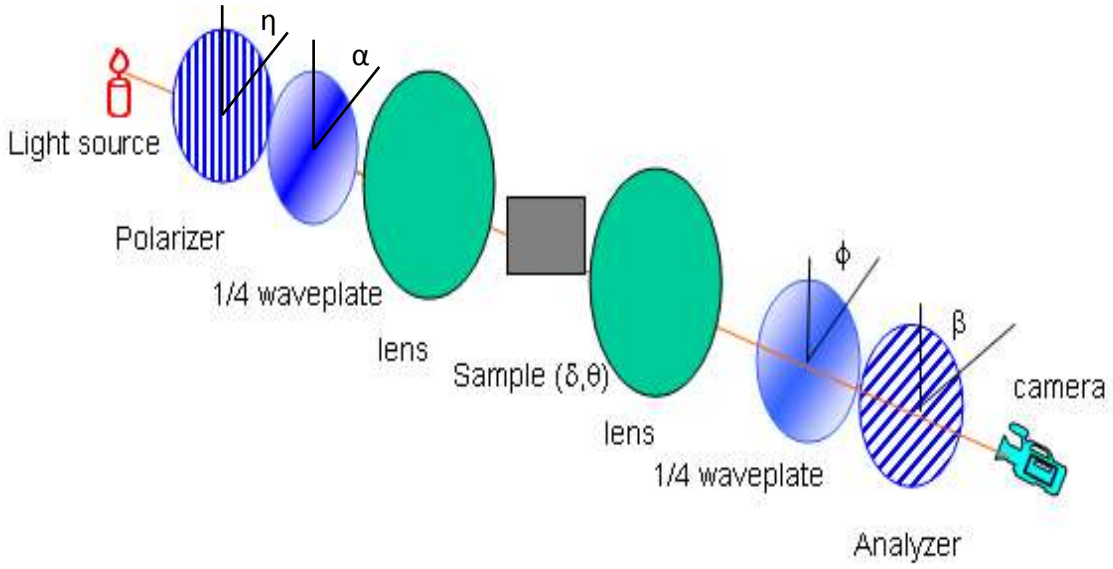

Figure 3-13: Experimental setup of NIR polariscope.

The light source used is an Oriel broadband tungsten-halogen lamp operable over a range of 40-250 W. At 150 W, there is sufficient intensity for analysis after a 10 nm narrow band filter, as shown in Figure 3-14:

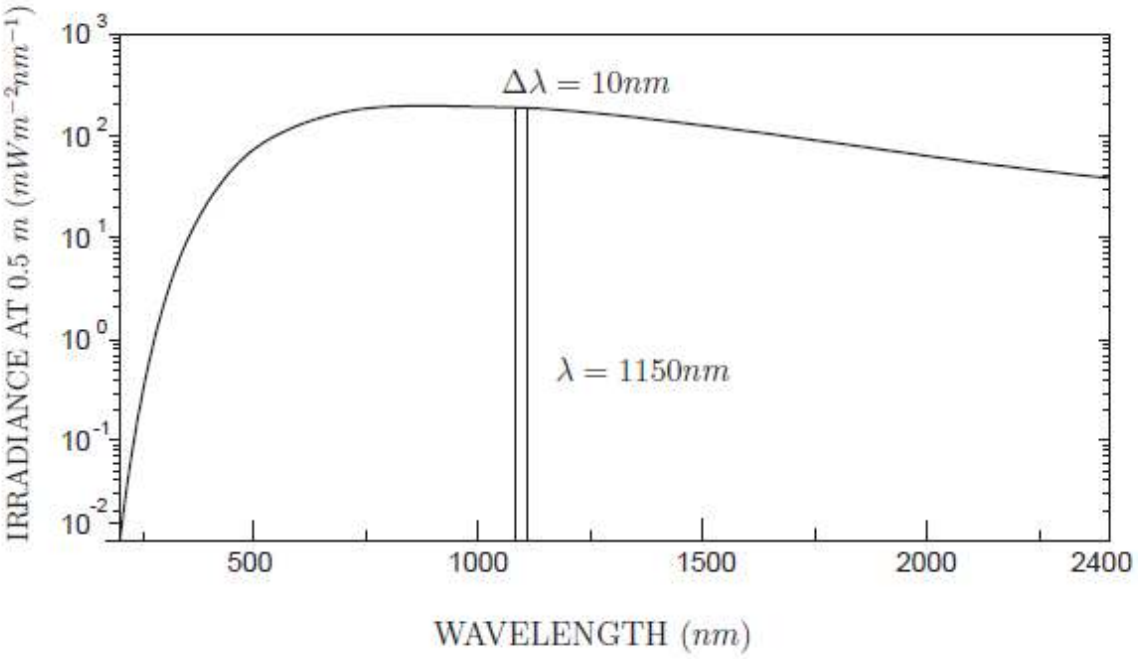

Figure 3-14: Spectrum of tungsten-halogen light source. [37]

Two polarizers 100 mm in diameter also serve as band pass filters in the range of 800 to 1200 nm. 100 mm diameter input and output quarter waveplates calibrated for 1150 nm are placed just inside the polarizers, and a 230-mm diameter lens pair collimates the light before it passes through the sample. An infrared camera is used for image acquisition. The entire arrangement from light source to camera is 1.5 m long. Images from the camera are sent directly to a computer, where they are used for data evaluation. The light source, optics, and camera are all placed on an isolation table.

An aperture may be placed between the light source and input polarizer. The aperture protects the polarizer from heat damage and limits interference from stray light pollution. The infrared camera is a Canon 50D modified for operation in the NIR range. The modifications include a 700 nm low pass filter and an altered anti-reflective coating on the photosensor. Monochromatic images of 4752 x 3168 pixels are captured using

Canon EOS Utility software. A standard USB cable connects the camera to the computer, where settings such as shutter speed, aperture, and ISO sensitivity may be controlled. Figure 3-15 shows a typical Canon EOS Utility interface through which camera control and image capture is performed.

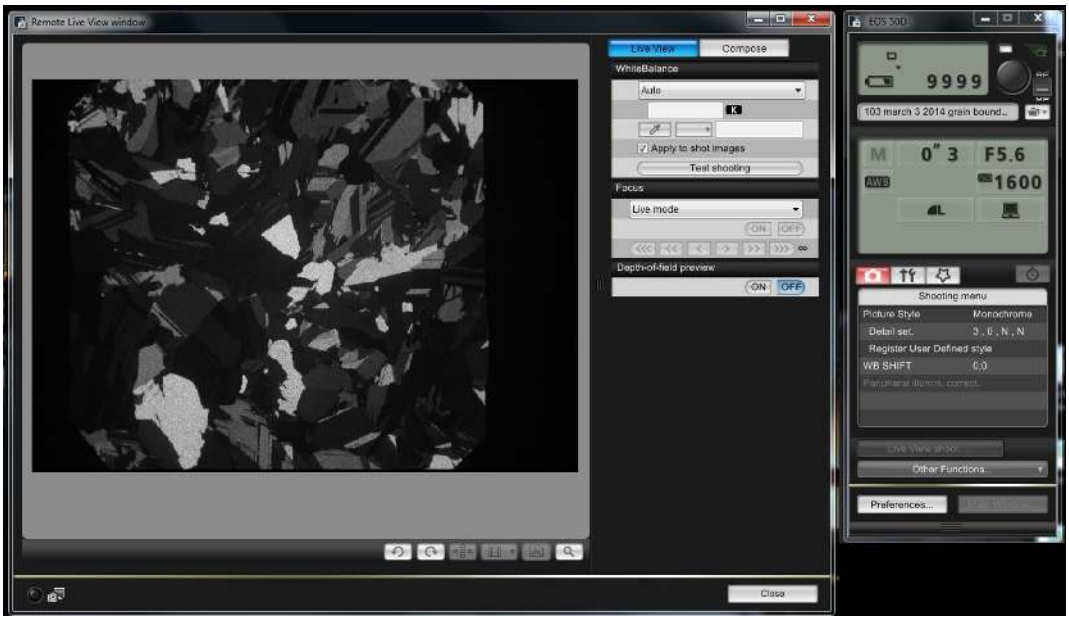

Figure 3-15: Canon EOS Utility image acquisition software.

Acquired images are stored as JPEG or RAW files. A live video feed from the camera to the computer is used for image focus and proper adjustment of camera parameters. An ideal series of images contains no saturated or completely dark pixels. Once proper photography conditions are obtained, the camera settings remain constant for the duration of the experiment. After all images have been stored, a MATLAB program is used to extract data. Figure 3-16 shows the program interface for analysis of stresses in a silicon wafer.

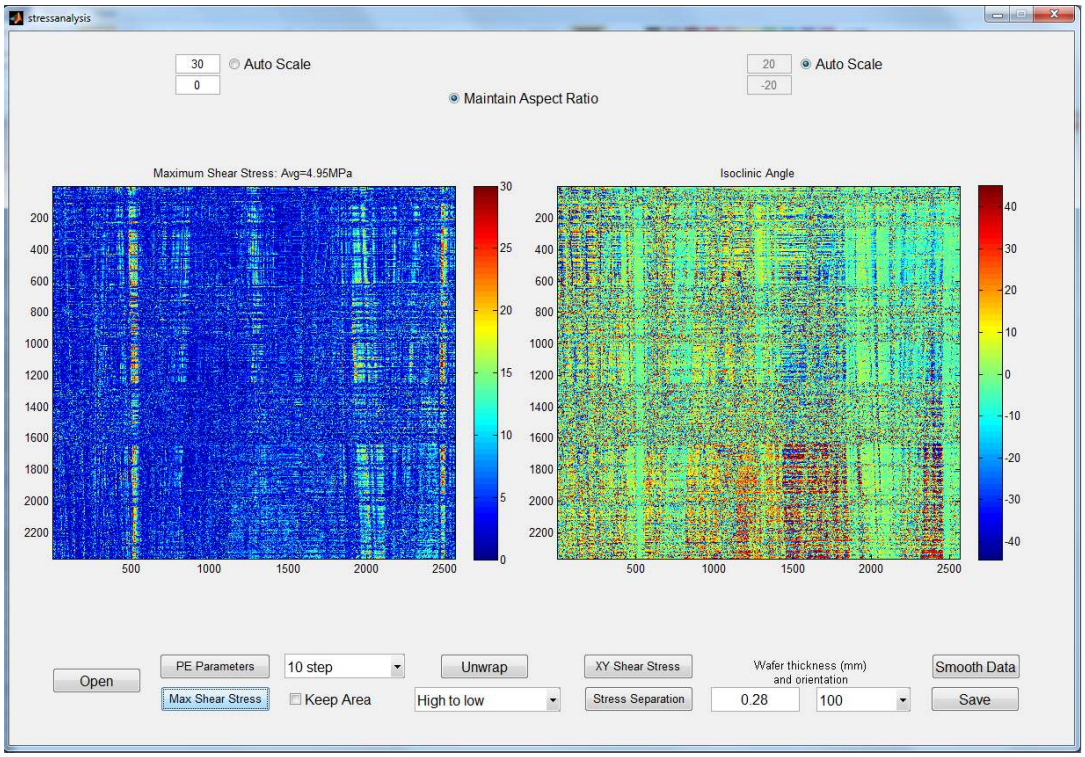

Figure 3-16: MATLAB stress analysis program interface.

CHAPTER 4
RESEARCH PLAN

The objective of this research is to expand the capabilities of birefringence with regards to residual stress measurement using crystalline silicon as a model material. Hardware improvements and advances in numerical methods allow for a greater understanding of the data provided by the polariscope. This data can then be used to investigate stresses in silicon wafers, including wafer-scale stresses and localized stress concentrations.

The full-field NIR polariscope was modified with improvements to the optics and camera. These components were validated with analysis of a single-crystal CZ beam in 4-point bending. Residual stresses in silicon are often on the order of less than one-tenth of a photoelastic fringe, and any improvement in data acquisition is desired. Patterson and Wang's six-step phase shifting technique was discarded in favor of Ramji and Ramesh's recently developed 10-step algorithm, and the resulting improvements were investigated and documented. Finally, noise reducing smoothing techniques and quality-guided unwrapping and integration processes were implemented to further improve the quality of the residual stress data.

Wafer-scale stresses in single-crystal CZ wafers were examined and investigated as a function of wafering processes, growth rate, and surface damage. For multicrystalline wafers, a system of grain sorting by way of transmitted brightness level was calibrated on single-crystal samples, performed on multicrystalline samples, and verified with X-ray diffraction. A new quality-guided shear difference integration

technique was paired with the identification of zero-stress points as adequate boundary conditions for complete stress resolution in each grain.

Finally, localized stress concentrations were examined in single crystal and multicrystalline wafers. Residual stresses surrounding Vickers indentations were investigated in CZ wafers. The interaction between multiple indentations in close proximity was also studied, and a model was created relating the proximity of indentations in an array and the stress field surrounding the entire array. Multicrystalline wafers were found to have considerably higher stresses at grain boundaries. The effect of an external stress source on the stresses at a grain boundary was explored by placing Vickers indentations in close proximity to grain boundaries. Grain boundary theory and contact mechanics were consulted to explain the interaction between grain boundary stresses and stresses surrounding indentations.

CHAPTER 5
CRYSTALLOGRAPHIC ORIENTATION IDENTIFICATION

5.1 Stress-optic coefficient dependence on crystallographic orientation

The stress-optic coefficient C in Equation (10) is a material constant used to calibrate the photoelastic parameters θ and δ to physical stresses. Light propagation in crystalline materials depends on the crystallographic orientation of the material due to the optic axis varying with orientation. Figure 5-1 is a schematic diagram that shows the relationship of the light rays relative to the (100) and (110) planes.

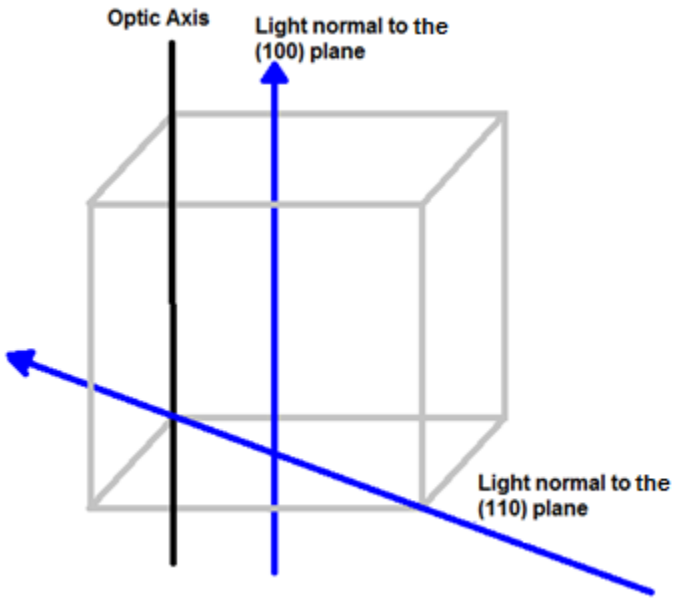

Figure 5-1: Schematic diagram showing propagation of light through a crystalline material relative to the optic axis.

The two rays of light illustrated in Figure 5-1 will propagate at different velocities through a birefringent material due to the different propagation direction relative to the optic axis. Birefringence of doubly refracting materials also varies with crystallographic

orientation. This effect is magnified when the material is subject to stresses. He and Li were able to demonstrate that *C* also varies with crystallographic orientation in silicon [38, 16]. A sample of their results is presented in Table 5-1, and a transmission image of a multicrystalline wafer is shown in Figure 5-2. Multicrystalline wafers such as the one in Figure 5-2 contain a variety of crystallographic orientations. Differentiating between these orientations is an important part of the stress analysis.

Table 5-1: Stress-optic coefficient variation by crystallographic orientation.

Orientation (φ)	100	111	111	111	210	211	321	322	421
Rotation (θ)	20	53	-5	65	-8	31	-100	106	73
C ($10^{-11}\times Pa^{-1}$)	2.40	2.54	2.53	2.55	2.08	2.75	1.87	2.35	1.75

Figure 5-2: NIR transmission image of multicrystalline silicon wafer.

Evaluation of residual stresses in multicrystalline material is dependent on knowledge of the crystallographic orientation, since stress-optic coefficients are needed as a function of orientation. Crystallographic orientation is relatively straightforward to obtain by X-ray diffraction. A similar evaluation methodology using a Laue backscatter system has been developed by Reimann et al. [39] for the purpose of identifying grain orientations. This system can measure the orientation of grains 5 mm^2 or larger, but takes 1-2 hours to measure an entire 156 x 156 mm wafer.

5.2 Grain sorting using relative transmission brightness

Part of this thesis sought to develop a grain orientation identification and correlation to calibrate silicon wafers of specific orientations. Figure 5-1 shows a transmission image of a cast multicrystalline wafer taken by the NIR polariscope; monochrome images simplify comparison between grains. A sorting algorithm was used to separate grains into four bins based on ranges of grayscale brightness from 0 – 255. The isolated brightness levels are shown from darkest to brightest in Figure 5-3. Regions that are black do not fall within the highlighted brightness level.

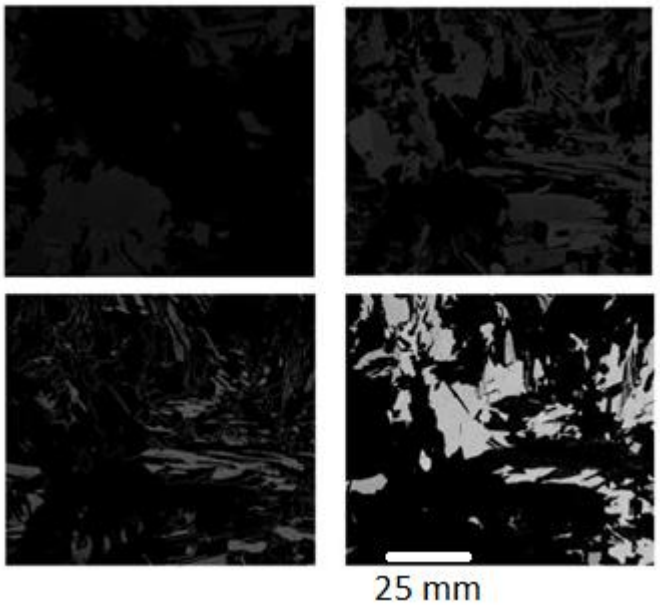

Figure 5-3: Example of NIR transmission images showing grains separated by brightness levels.

The brightness of each group of grains is thus easily determined by any NIR transmission image such as the one in Figure 5-2. An average brightness value for each group is calculated from all of the pixels binned. Table 5-2 summarizes the average brightness of each group.

Table 5-2: Grain transmission intensities.

Grain Category	**Mean Transmitted Brightness, 0 – 255**
Bright	172.9
Medium Bright	71.2
Medium Dark	35.3
Dark	19.4

Semiconductor-grade single-side polished CZ wafers of known orientation were then obtained and examined through the polariscope to create a calibration scale for the

brightness categories. Residual stresses in the bulk material of these wafers were assumed to be negligible. Single-side polished P-type wafers, 200 mm in diameter, 525 μm thick, and of four orientations: (111), (110), (100), and (211) were used for this calibration. The transmission results of these four orientations are shown in Figure 5-4.

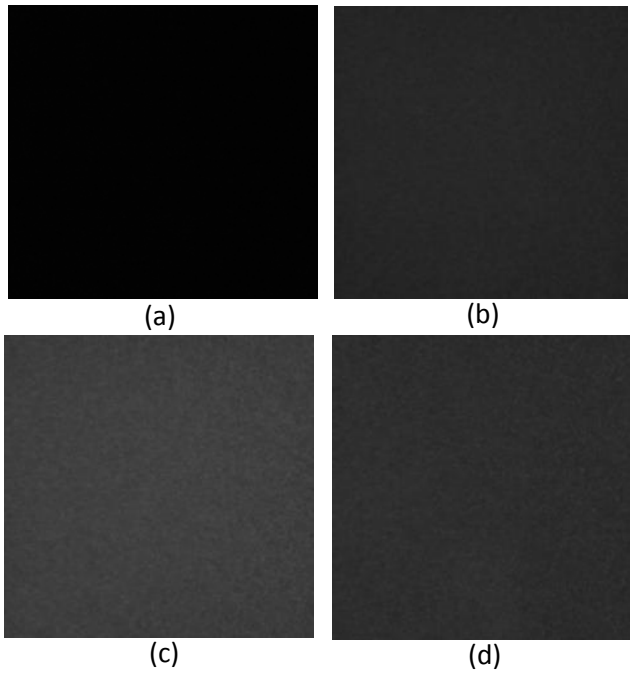

Figure 5-4: NIR transmission images of (a) [111], (b) [110], (c) [100], (d) [211] semiconductor-grade 200 μm thick P-type CZ wafers.

Obtaining the average grayscale intensity value is then straightforward. Monochromatic transmission images of each wafer were obtained with the NIR camera. The images were then imported into MATLAB for analysis. The average transmission intensity over the wafer surface is given with crystallographic orientation in Table 5-3.

Table 5-3: NIR transmission image brightness comparison of CZ single-crystal wafers.

Crystallographic Orientation	Mean Transmitted Brightness, 0-255
[111]	2.4
[110]	39.4
[100]	65.5
[211]	42.7

A correlation may be drawn between the contents of Tables 5-2 and 5-3. Each average from Table 5-2 matches up with a crystallographic orientation in Table 5-3. However, a transmitted intensity of 172.9 was recorded for the brightest grain type in the multicrystalline wafer (Table 5-2), but no comparable transmission intensity was measured from the single-crystal wafers. A multicrystalline silicon wafer was sectioned into bars and the orientation of several grains was determined by X-ray diffraction. An NIR transmission image was taken of one of these bars to find grains with a transmitted intensity in the range of 170. This bar is shown in Figure 5-5.

Figure 5-5: NIR transmission image of a multicrystalline beam, bright grain highlighted.

The grain within the red box is one of the brightest grains in the image, and was identified as of the (344) orientation. The average brightness level of the grain was found to be 185.3, which is comparable to the transmitted intensities of the brightest grains in Figure 5-3. Grains identified as (111) were the darkest, while other orientations varied in transmission intensity from 40-100. Figure 5-6 graphically illustrates the correlation.

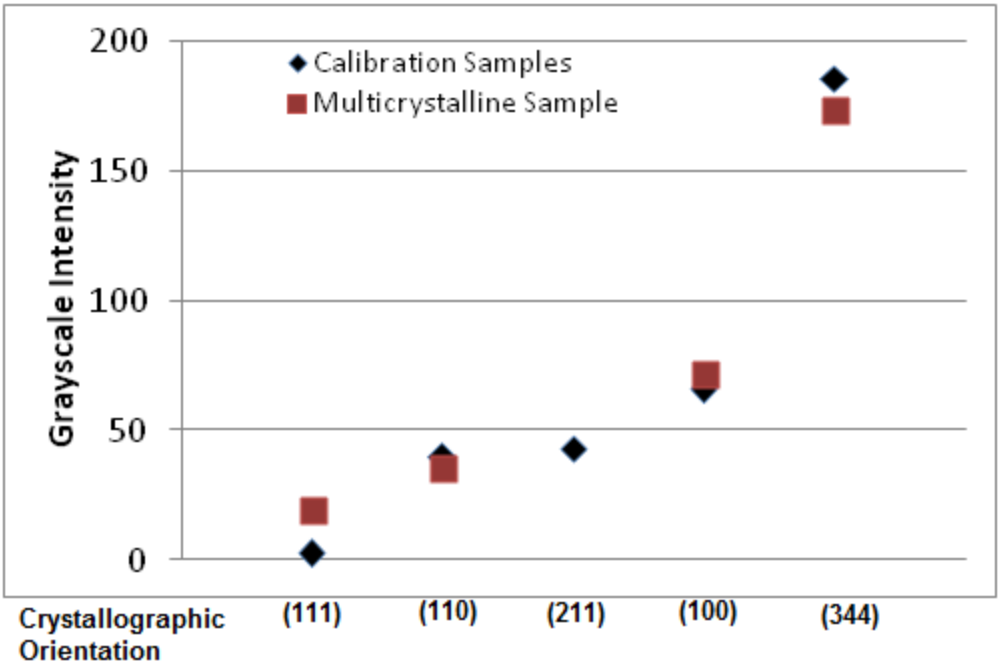

Figure 5-6: Grayscale intensity showing the correlation between CZ and multicrystalline grain transmission (0-255).

To further validate the results, X-ray diffraction (XRD) was performed on numerous grains in the two samples shown below in Figure 5-7. A schematic of the XRD procedure is shown in Figure 5-8.

Figure 5-7: NIR transmission images of two multicrystalline wafers used as the XRD verification samples.

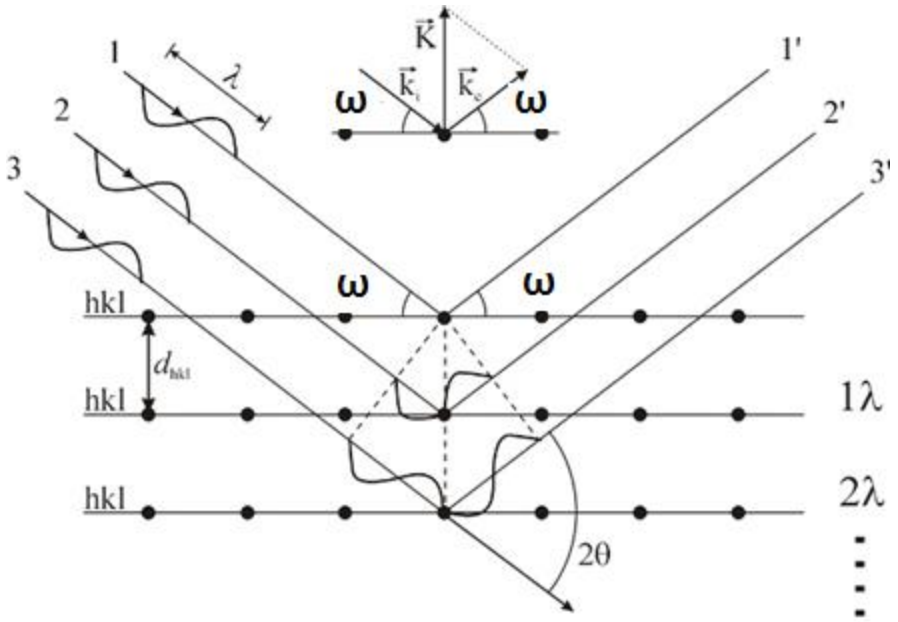

Figure 5-8: Schematic diagram of the diffraction of X-rays by a crystalline material.

The diffracted intensity provides the orientation of the crystal as described by Bragg's Law as shown in Figure 5-8.

Grains of varying transmission intensity were investigated to strengthen the correlation between crystallographic orientation and transmission intensity. Figures 5-9 through 5-12 show four grains and their respective XRD results.

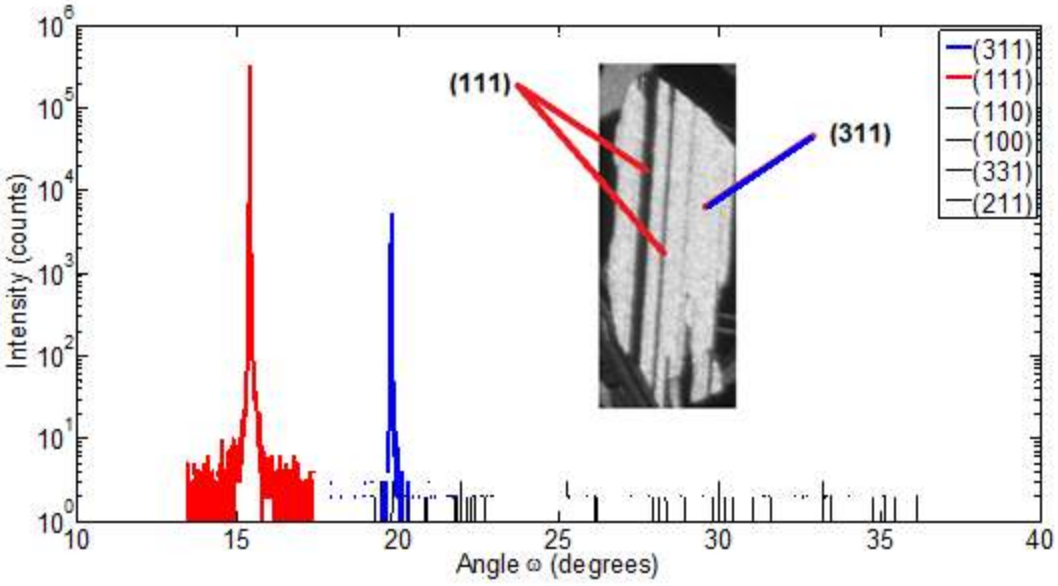

Figure 5-9: NIR transmission image (inset) and intensity (counts) vs. diffraction angle (degrees) from XRD results for the "bright" grain.

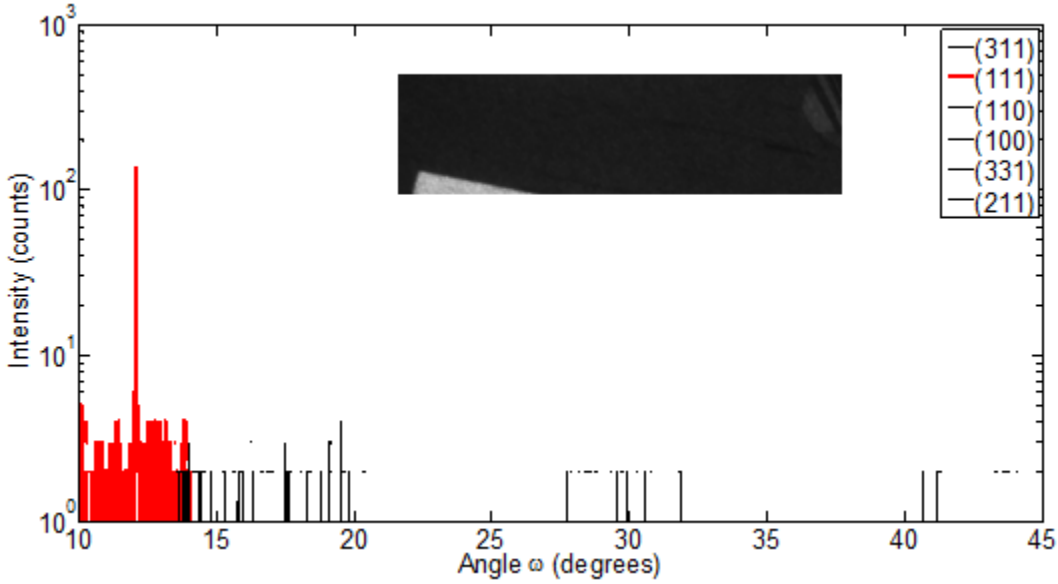

Figure 5-10: NIR transmission image (inset) and intensity (counts) vs. diffraction angle (degrees) from XRD results for the "dark" grain.

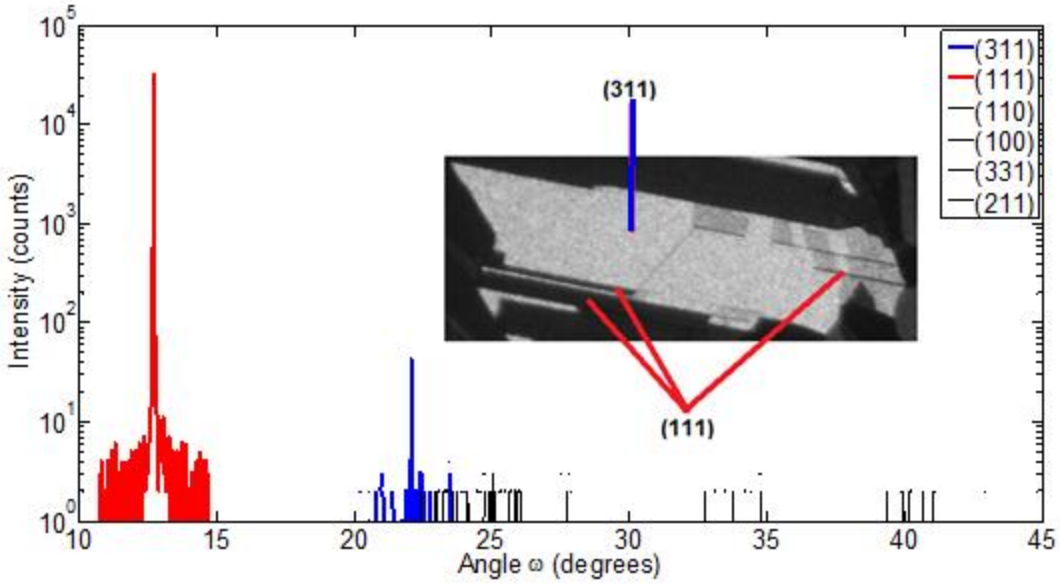

Figure 5-11: NIR transmission image (inset) and intensity (counts) vs. diffraction angle (degrees) from XRD results for the "bright" grain.

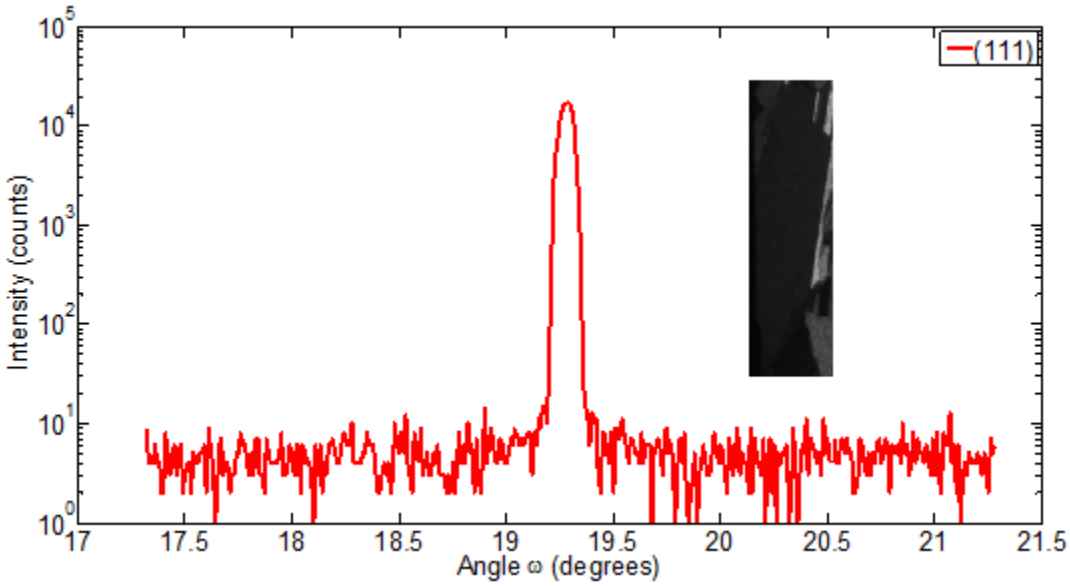

Figure 5-12: NIR transmission image (inset) and intensity (counts) vs. diffraction angle (degrees) from XRD results for the "dark" grain.

Figure 5-6 indicates the correspondence between crystallographic orientation and NIR transmission intensity, with each orientation matching closely with a unique NIR

transmission brightness level. The XRD data does not support such a tight correlation. However, the XRD data shows that {111} grains are consistently darker than other orientations. A comparison of the bar in Figure 5-5 and the grains in Figures 5-9 and 5-11 indicate that bright grains were determined to be of orientation {311}, {344}, or some similar higher-order {*hkl*} structure. The grains in the middle of the brightness scale displayed no clear relationship between transmission intensity and crystallographic orientation.

The transmission intensity through different crystallographic orientations can be related to planar atomic density. Silicon is a diamond-centered cubic structure with a two atom basis. The planar density for silicon can be determined by calculating the density of an FCC lattice and multiplying by two. Figure 5-13 shows the (100), (110), and (111) planes in a single lattice unit cell.

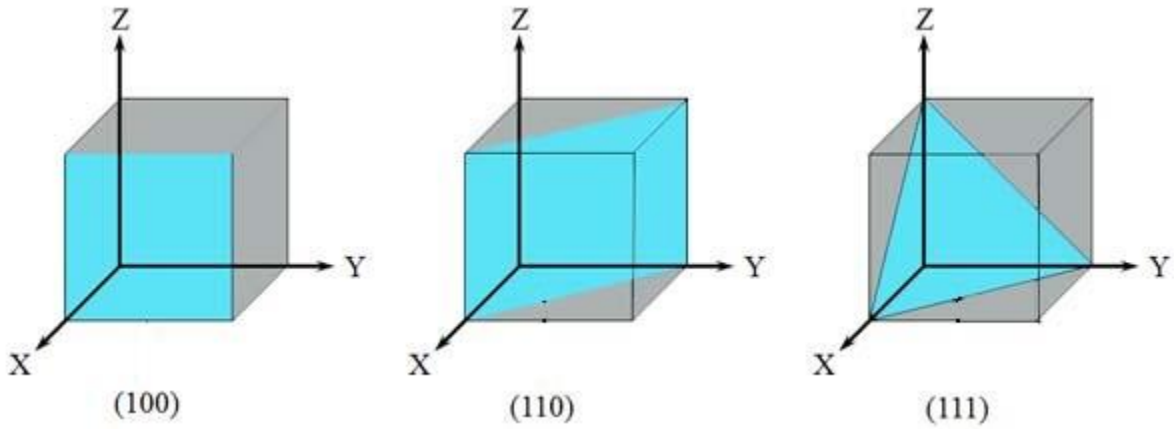

Figure 5-13: Schematic diagram of crystallographic planes in a unit cell.

Figure 5-14 illustrates the atoms at their crystallographic locations on the lattice in the planes outlined by Figure 5-13. The dimension of the lattice is represented by lattice length a_0.

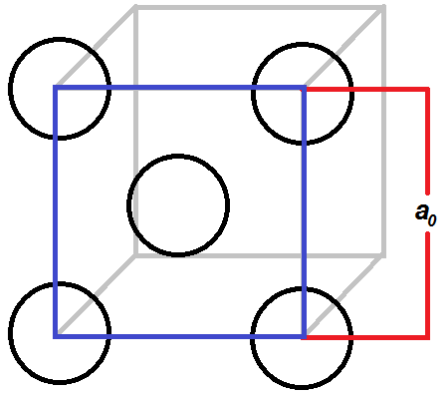

(a)

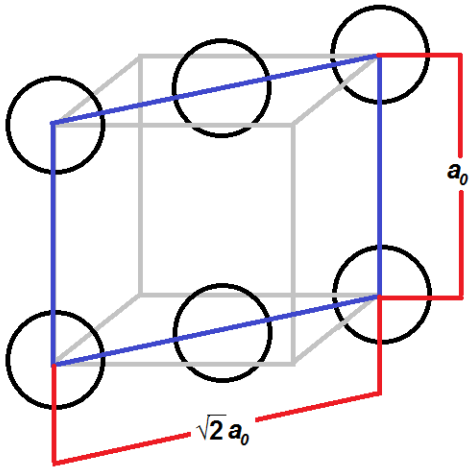

(b)

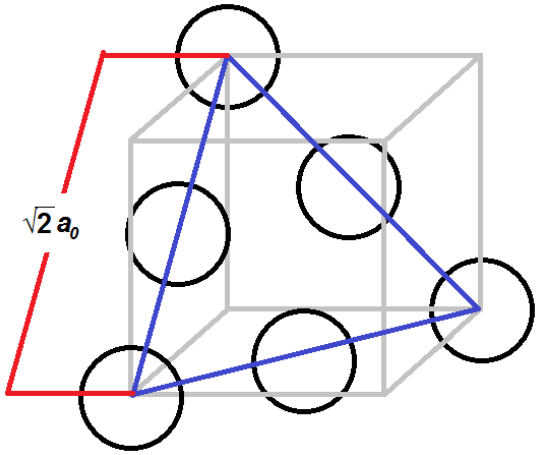

(c)

Figure 5-14: Schematic diagram of atoms in (a) (100), (b) (110), (c) (111) planes.

Atoms in orientations such as {111} will interact with the electromagnetic wave to a greater degree than less dense orientations, resulting in a lower transmission intensity. Figure 5-15 shows transmission intensity as a function of atomic planar density.

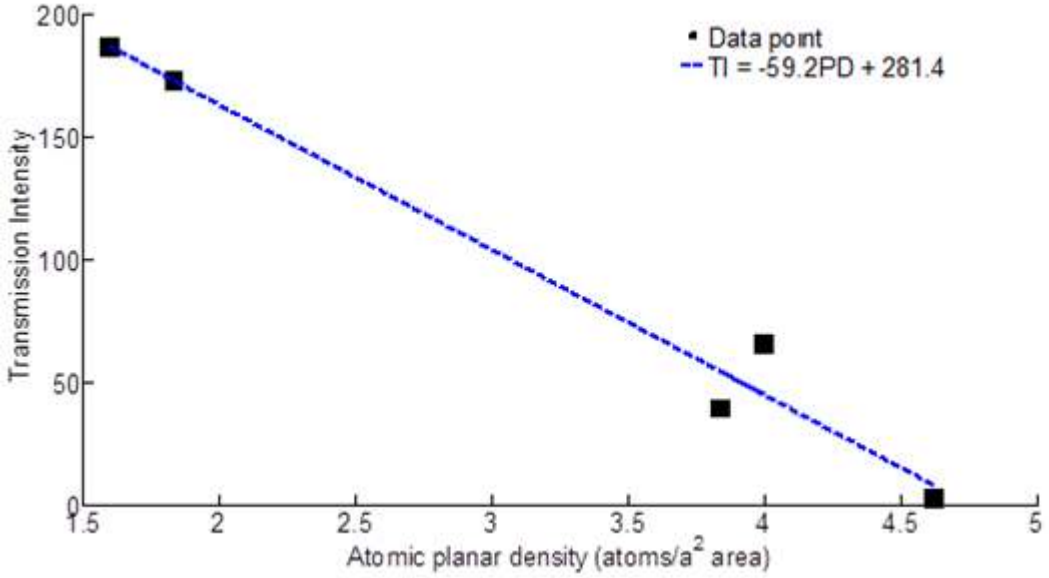

Figure 5-15: Transmission intensity (pixel values ranging from 0-255) vs. atomic planar density (atoms/area).

From left to right, the data points for atomic planar density are from the {331}, {311}, {110}, {100}, and {111} crystallographic orientations. The R^2 value for the line in Figure 5-15 is 0.96, representing a good data fit. Atomic planar density is measured in atoms per lattice length a_0 squared. If the incident light is assumed to be normal to the {111} plane, it is reasonable to conclude that the densely packed {111} grains should be quite dark, while the far less dense higher-order orientations will be consistently brighter. It is important to keep in mind that planar density will not only be determined by

crystallographic orientation, but also by any misalignment from a specific orientation. Thus, it is also reasonable to expect that a severely misaligned grain may allow a lower level of NIR transmission than a perfectly aligned grain.

The data collected through three separate validation methods indicates that a rough estimate of crystallographic orientation may be drawn through NIR transmission intensity. {111} grains appear to be consistently darker than average, while orientations of {311} or higher are consistently the brightest. With this knowledge and a grain-sorting algorithm based on transmission intensity, correct stress-optic coefficients may be applied to a significant portion of the wafer area, increasing the accuracy of residual stress evaluation through photoelasticity. The {111} stress optic coefficient may be applied to the darkest grains in the sample, while a smaller coefficient common among higher-order orientations (see Table 5-1) may be used for brighter grains. Finally, the middle grains can be evaluated using the {100} stress optic coefficient. This procedure is an improvement over using one coefficient to evaluate the entirety of a multicrystalline wafer. Figure 5-16 displays a multicrystalline wafer with grains sorted into {111}, {100}, and {311} bins.

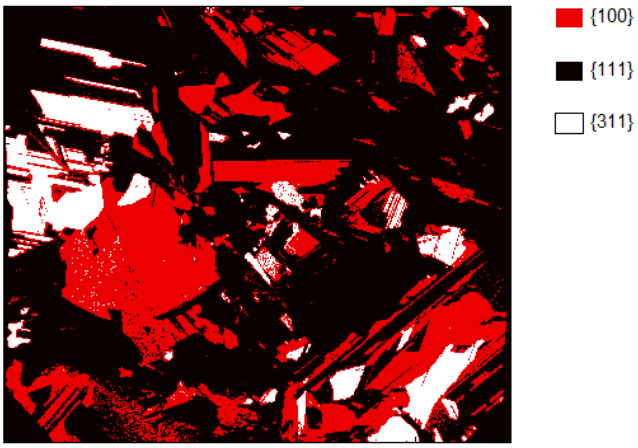

Figure 5-16: Grains in a multicrystalline wafer identified by NIR transmission.

Finally, while the CZ wafers were remarkably consistent in their transmission levels (standard deviation of ~1 brightness level), variables such as surface finish would be expected to shift the entire line. It is not reasonable to expect an as-cut sample to provide the same level of transmission as a double-side polished wafer. As such, the absence of brightness levels greater than 150 does not necessarily mean that all grains present are of {111}, {110}, or {100} orientations. Rather, the relationship between grains of a specific sample should be normalized, with the brightest grains of each wafer identified as the higher-order crystallographic orientations. Figure 5-17 shows the same data as Figure 5-15 with percentage of brightest grain used as the y-axis metric.

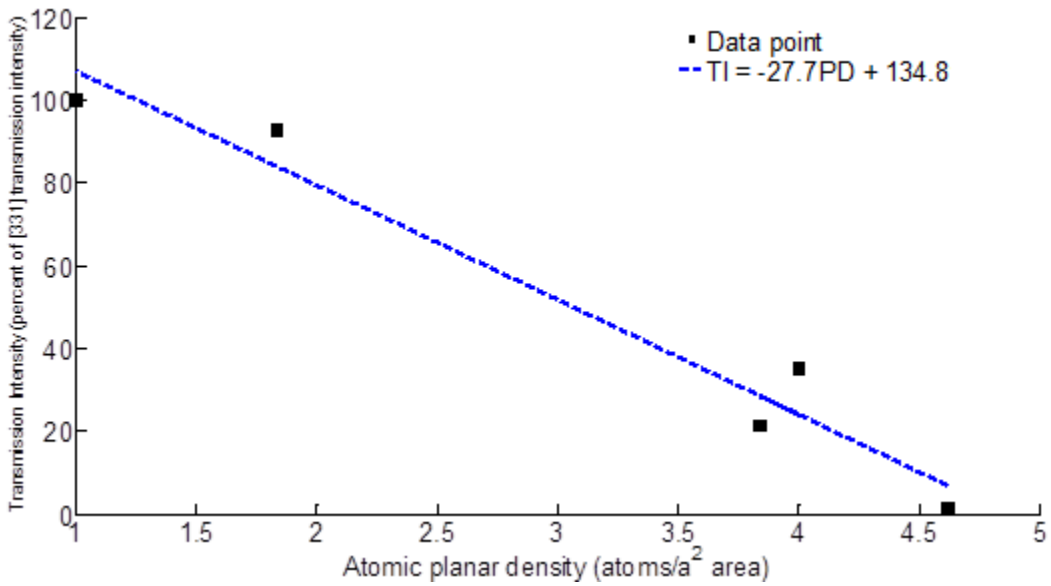

Figure 5-17: Transmission intensity (% of brightest measured grain) vs. atomic planar density (atoms/area).

5.3 Conclusions

Crystallographic orientations can be assigned to grains in multicrystalline silicon wafers based on their NIR transmission intensity. Transmission intensity through silicon is related to planar atomic density. These results were confirmed with data collected from NIR transmission through multicrystalline wafers, NIR transmission through single crystal CZ wafers of known orientation, and X-ray diffraction of grains in multicrystalline wafers.

CHAPTER 6
DATA ACQUISITION AND NOISE REDUCTION

6.1 Challenges in residual stress photoelasticity

Research conducted with photoelasticity often involves polymeric samples placed under an applied load. These loads perform three functions: overwhelm any residual stresses present in the sample, provide a loading stress state that is expected, and ensure that the stresses in the sample will be high enough to create multiple photoelastic fringes for analysis. Photoelastic fringes are identified as alternating light and dark bands present in a captured image. As an example, Figure 6-1 shows an NIR transmission image of a polymeric disc under compressive load with a fringe order (number of fringes) of approximately 10.

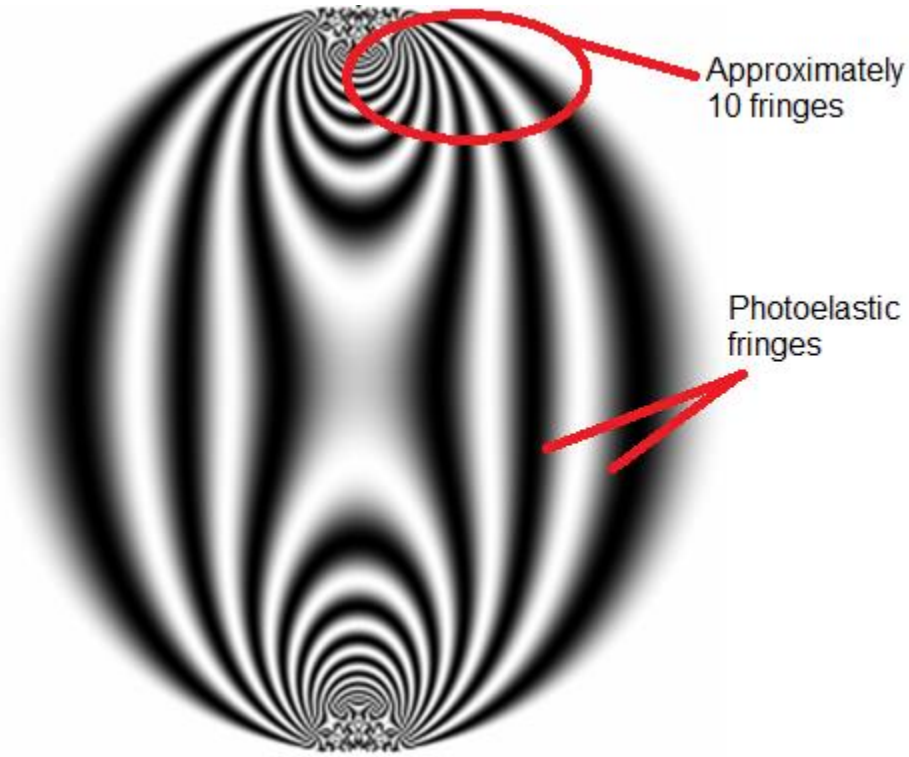

Figure 6-1: NIR transmission image of a polymer disc under compression.

Each fringe consists of a bright and dark band. The fringe order of the disc is determined by counting the bands present. Stresses in silicon are small and do not result in multiple fringes. The thin profile and brittle nature of silicon wafers cause difficulties in keeping the applied stresses within the viewing plane and in not fracturing the sample. However, calibration using applied loads is necessary. Figure 6-2 shows a double-side polished 200 μm thick p-type single-crystal CZ silicon beam loaded in in-plane four-point bending. Note that while visible light and dark areas are visible, a complete fringe is not present. In absence of a complete fringe, the measured phase retardation δ is divided by 2π to obtain a fringe number map of the sample. The highest evaluated fringe number is the fringe order of the sample. The fringe order of the beam in Figure 6-2 is ~0.3.

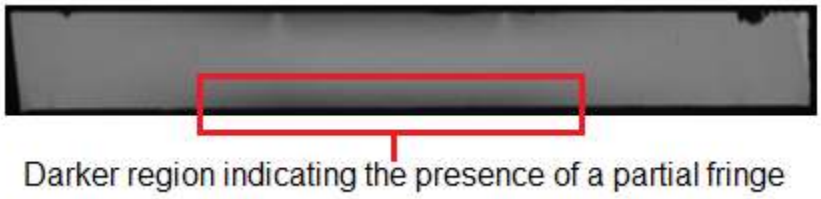

Figure 6-2: NIR transmission image of a single crystal silicon beam in 4-point bending.

The majority of residual stresses in photovoltaic silicon wafers are lower than the stresses in the beam in Figure 6-2. Single crystal CZ samples in particular such as the one in Figure 6-3 may have a fringe order of only ~0.05. The nature of the algorithm for photoelastic parameter evaluation can potentially cause higher noise levels at lower stress levels.

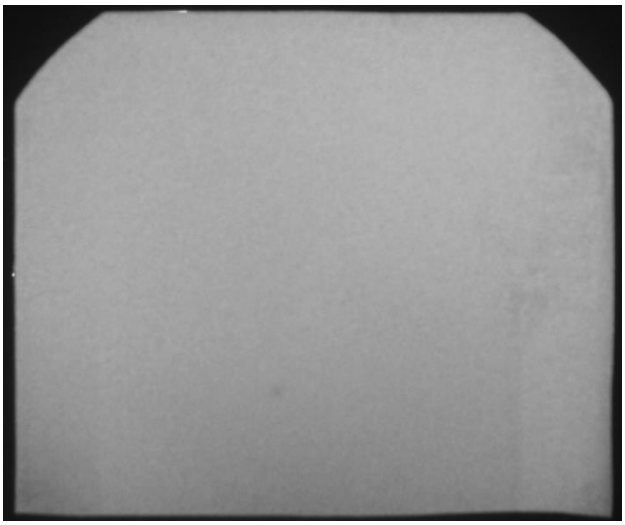

Figure 6-3: NIR transmission image of a CZ wafer with no applied load showing a fringe order of 0.05.

6.2 Phase shifting: 10-step vs. 6-step algorithm

Hecker and Morche first introduced the phase shifting concept to photoelasticity in 1986 [33]. Light transmitted through a plane polariscope arranged like the one in Figure 2-1 takes on the general form

$$I = I_b + I_a\left[\cos^2\frac{\delta}{2}\cos^2(\beta-\alpha) + \sin^2\frac{\delta}{2}\cos^2(\beta+\alpha-2\theta)\right] \tag{12}$$

Where I is the final image captured by the camera, α is the angle of the polarizer, and β is the angle of the analyzer. The addition of waveplates adds several extra terms and the angles η and ϕ to Equation (12). There are four unknowns in the above equation: the stray light parameter I_b, the intensity I_a when all optic axes are parallel, and the photoelastic parameters θ (isoclinic angle) and δ (phase retardation). A physical representation of the photoelastic parameters can be found in Figure 2-2. These four unknowns can be solved using a system of equations. The necessary system can be

created by rotating the optic elements, changing the angles α, β, η, and ϕ seen in Figure 3-13. This procedure is known as phase shifting or phase stepping.

Several phase shifting algorithms have been published, of which Patterson and Wang's 6-step process [34] remains the most popular. The Patterson and Wang method uses two polarizers and two quarter waveplates in a circular polariscope to evaluate the isoclinic and isochromatic photoelastic parameters. Table 6-1 shows the angles of the six optical arrangements for the Patterson and Wang method.

Table 6-1: Polarizer and waveplate orientations for Patterson and Wang 6-step algorithm.

P	QWP1	QWP2	A	Intensity Equations
$\pi/2$	$3\pi/4$	0	$\pi/4$	$I_1 = I_b + \frac{I_a}{2}(1+\cos\delta)$
$\pi/2$	$3\pi/4$	0	$3\pi/4$	$I_2 = I_b + \frac{I_a}{2}(1-\cos\delta)$
$\pi/2$	$3\pi/4$	0	0	$I_3 = I_b + \frac{I_a}{2}(1-\sin 2\theta\sin\delta)$
$\pi/2$	$3\pi/4$	$\pi/4$	$\pi/4$	$I_4 = I_b + \frac{I_a}{2}(1+\cos 2\theta\sin\delta)$
$\pi/2$	$3\pi/4$	$3\pi/4$	0	$I_5 = I_b + \frac{I_a}{2}(1+\sin 2\theta\sin\delta)$
$\pi/2$	$3\pi/4$	$\pi/4$	0	$I_6 = I_b + \frac{I_a}{2}(1-\cos 2\theta\sin\delta)$

Solving for the isoclinic angle θ_c can thus be accomplished through the last four steps in Table 6-1. Combining the intensity equations from steps 3-6 and isolating the θ term results in the following expression:

$$\theta_c = \frac{1}{2}\tan^{-1}\left(\frac{I_5 - I_3}{I_4 - I_6}\right) \tag{13}$$

Where I_n is the transmission intensity of a single pixel in the n^{th} image. The isoclinic parameter can then be evaluated for every pixel of the wafer.

The fractional retardation δ_c is found in the same manner. Combining the six equations and isolating δ yields the following equation for evaluation:

$$\delta_c = \tan^{-1}\left(\frac{(I_5 - I_3)\sin 2\theta + (I_4 - I_6)\cos 2\theta}{(I_1 - I_2)}\right) \tag{14}$$

Here, θ is the isoclinic angle calculated through Equation (13) and I_n is again the transmission intensity of the n^{th} image.

An important choice presents itself here when evaluating photoelastic parameters using phase stepping. The *atan2* function is a common feature of most programming languages and uses two inputs to determine the appropriate quadrant of the computed angle [40]. Values returned by the *atan2* function over a range of arguments are shown below in Figure 6-4.

$$\operatorname{atan2}(y,x) = \begin{cases} \arctan\left(\frac{y}{x}\right) & x > 0 \\ \arctan\left(\frac{y}{x}\right) + \pi & y \geq 0, x < 0 \\ \arctan\left(\frac{y}{x}\right) - \pi & y < 0, x < 0 \\ +\frac{\pi}{2} & y > 0, x = 0 \\ -\frac{\pi}{2} & y < 0, x = 0 \\ \text{undefined} & y = 0, x = 0 \end{cases}$$

Figure 6-4: Behavior of *atan2* function.

While using the *atan2* function to find the isoclinic angle does provide results in the desired range of [-π/2, π/2], sign changes at locations which should be consistent indicate that the traditional arctan function is the correct choice. However, the results given from the arctan function must be unwrapped in post-processing. Unwrapping is the

process by which the evaluated isoclinic parameter is expanded from the range [-π/4, π/4] to the appropriate range [-π/2, π/2]. This is accomplished by finding discontinuities in the isoclinic map where θ_c jumps from π/4 to -π/4 and adding π/2 to the negative values.

Ramji and Ramesh most recently proposed a 10-step phase shifting algorithm in 2008 [35]. The first four steps use a plane polariscope and are adopted from the technique of Brown and Sullivan [41], while the last six arrangements use a circular polariscope and are from a technique developed by Ajovalasit [42]. Table 6-2 shows the ten optical arrangements listed in order.

Table 6-2: Polarizer and waveplate orientations for 10-step algorithm.

P	QWP1	QWP2	A	Intensity Equations
$\pi/2$	-	-	0	$I_1 = I_b + I_a \sin^2\frac{\delta}{2}\sin^2 2\theta$
$5\pi/8$	-	-	$\pi/8$	$I_2 = I_b + \frac{I_a}{2}\sin^2\frac{\delta}{2}(1-\sin 4\theta)$
$3\pi/4$	-	-	$\pi/4$	$I_3 = I_b + I_a \sin^2\frac{\delta}{2}\cos^2 2\theta$
$7\pi/8$	-	-	$3\pi/8$	$I_4 = I_b + \frac{I_a}{2}\sin^2\frac{\delta}{2}(1+\sin 4\theta)$
$\pi/2$	$3\pi/4$	$\pi/4$	$\pi/2$	$I_5 = I_b + \frac{I_a}{2}(1+\cos\delta)$
$\pi/2$	$3\pi/4$	$\pi/4$	0	$I_6 = I_b + \frac{I_a}{2}(1-\cos\delta)$
$\pi/2$	$3\pi/4$	0	0	$I_7 = I_b + \frac{I_a}{2}(1-\sin 2\theta\sin\delta)$
$\pi/2$	$3\pi/4$	$\pi/4$	$\pi/4$	$I_8 = I_b + \frac{I_a}{2}(1+\cos 2\theta\sin\delta)$
$\pi/2$	$\pi/4$	0	0	$I_9 = I_b + \frac{I_a}{2}(1+\sin 2\theta\sin\delta)$
$\pi/2$	$\pi/4$	$3\pi/4$	$\pi/4$	$I_{10} = I_b + \frac{I_a}{2}(1-\cos 2\theta\sin\delta)$

The isoclinic and isochromatic data are obtained in a fashion similar to the Patterson and Wang technique. The equations necessary are given below.

$$\theta_c = \frac{1}{4}\tan^{-1}\left(\frac{I_4 - I_2}{I_3 - I_1}\right) \tag{15}$$

$$\delta_c = \tan^{-1}\left(\frac{(I_9 - I_7)\sin 2\theta + (I_8 - I_{10})\cos 2\theta}{(I_5 - I_6)}\right) \tag{16}$$

Ramesh recommends that the parameter θ_c in this case be evaluated with the *atan2* function [35]. However, θ_c will still need to be unwrapped to the desired range of [-π/2, π/2] before use for isochromatic evaluation.

Prasath and Skenes later compared the two phase shifting techniques in an attempt to quantify the advantages of one over the other [36]. Three silicon samples were studied: in-plane three-point bending applied to a bar diced from a single crystal CZ wafer, an unloaded edge-defined film-fed growth (EFG) wafer, and an unloaded cast multicrystalline wafer. The stresses in the samples were not measured, but the photoelastic parameters of each were evaluated. A schematic of the bar in three-point bending is presented below in Figure 6-5.

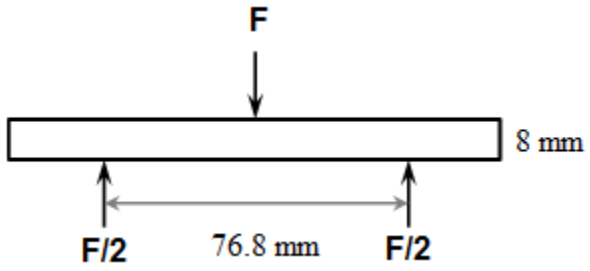

Figure 6-5: In-plane three-point bending schematic.

The predictable isoclinic and isochromatic states induced by three-point bending makes it ideal for calibration and comparison of polariscopy methods. A load was applied such that the maximum shear stresses at the edge of the bar were 30 MPa. The dimensions of the bar are also shown in Figure 6-5, and the sample thickness was 450 μm. Phase retardation and isoclinic angle plots for the bar as evaluated by the 6-step and 10-step techniques are presented below in Figure 6-6.

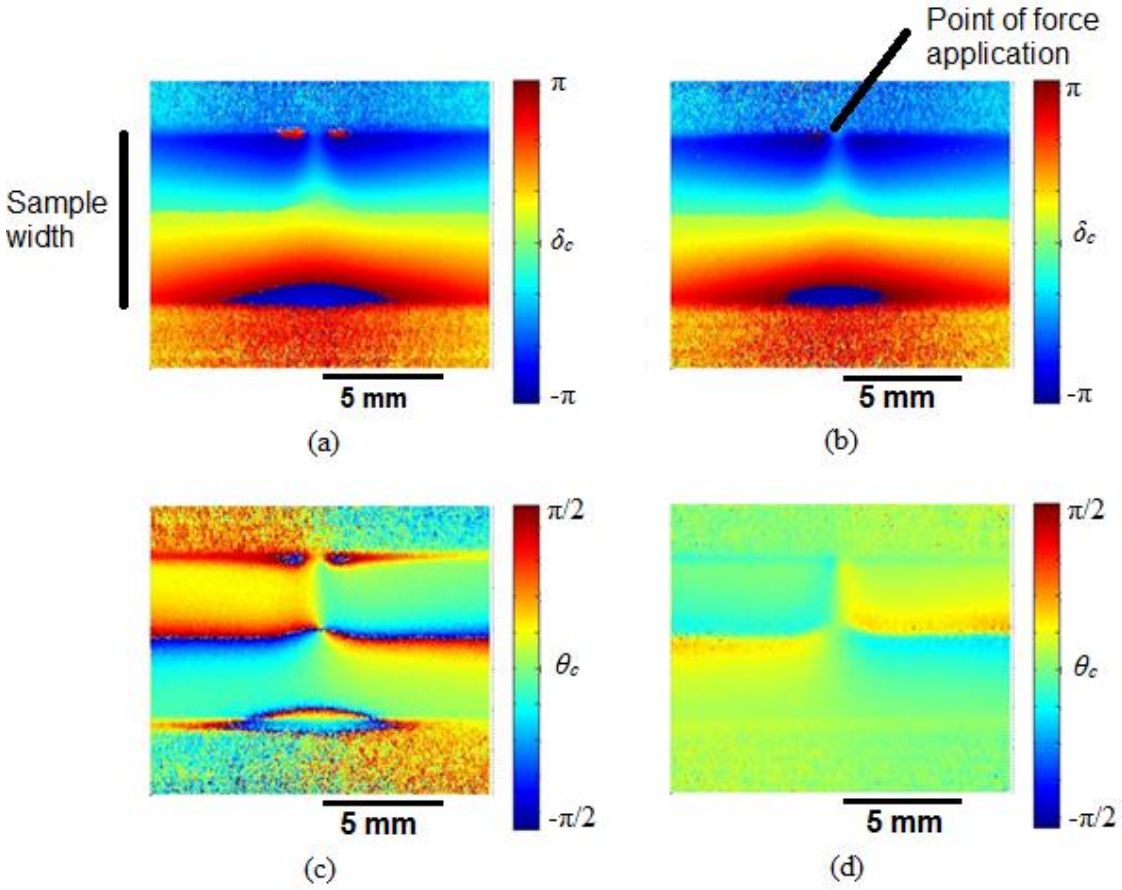

Figure 6-6: Isochromatics of three-point bending sample from (a) Patterson and Wang 6-step and (b) 10 step algorithm; wrapped isoclinics from (c) 6-step and (d) 10-step algorithm.

Note that a shift in retardation from negative to positive is clearly visible at the top of Figure 6-6(c). This shift causes a significant increase in noise and does not appear in

Figure 6-6(d). Similarly, the isoclinic plot generated by the 6-step method contains more discontinuities of greater severity as well as increased noise levels. Figure 6-7 illustrates the comparison by plotting the isochromatics and isoclinics along a single vertical line drawn through the beam.

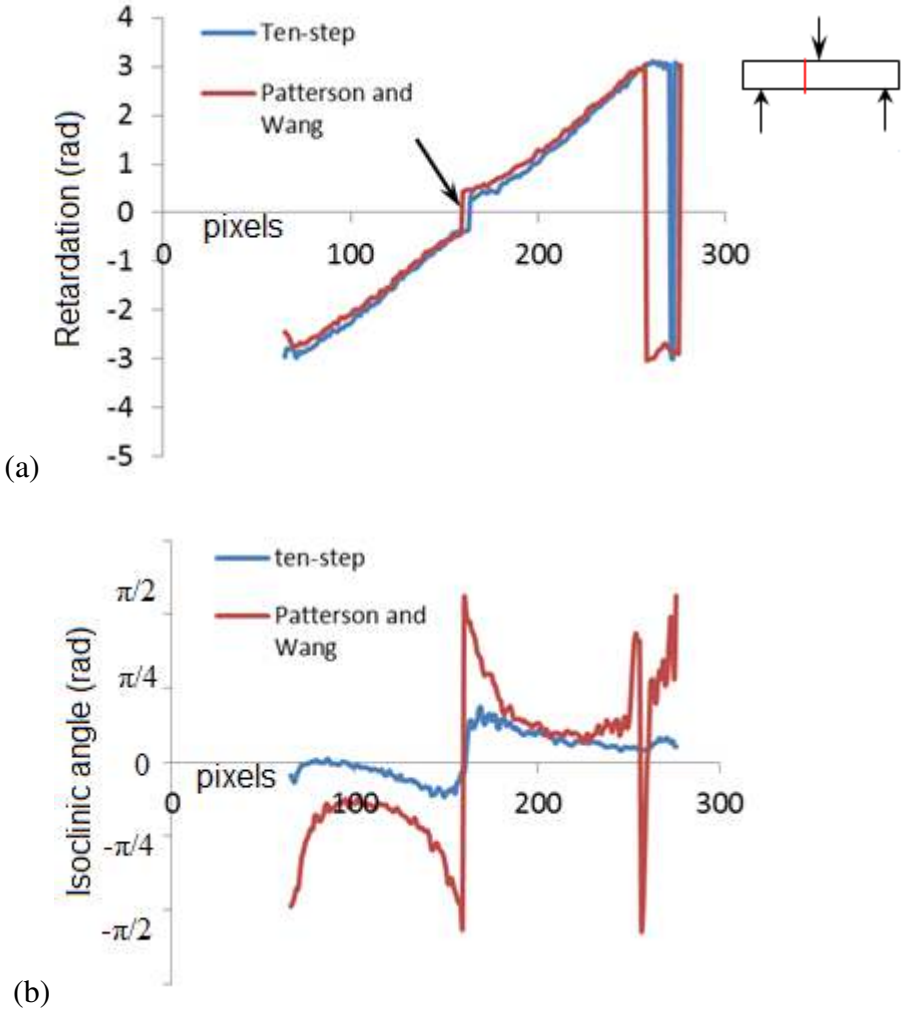

Figure 6-7: (a) Phase retardation (rad) vs. location (pixels) and (b) Isoclinic angle (rad) vs. location (pixels) of a vertical line trace across a beam in three-point bending.

The plots of isoclinic values along the vertical line clearly indicate a transition from negative to positive at the center of the bar. However, the transition is much more pronounced in the results generated by the Patterson and Wang 6-step method. A second

sign transition in the isoclinic plot in the Patterson and Wang results is clearly absent from the 10-step results.

These abrupt changes in isoclinic value have two causes. The first is the appearance of zero in the denominator of Equation (15), and the second is interaction between isochromatics and isoclinics in specific regions. Discontinuities such as these cannot physically exist and must be removed with phase unwrapping or other methods. The 10-step method generates few discontinuities and is less affected by the interaction between isochromatics and isoclinics, leading to improved computational cost overall.

The second two samples used for comparison were examined in a residual stress state with no applied external load. The EFG wafer is displayed in Figure 6-8, while the cast wafer is shown in Figure 6-9.

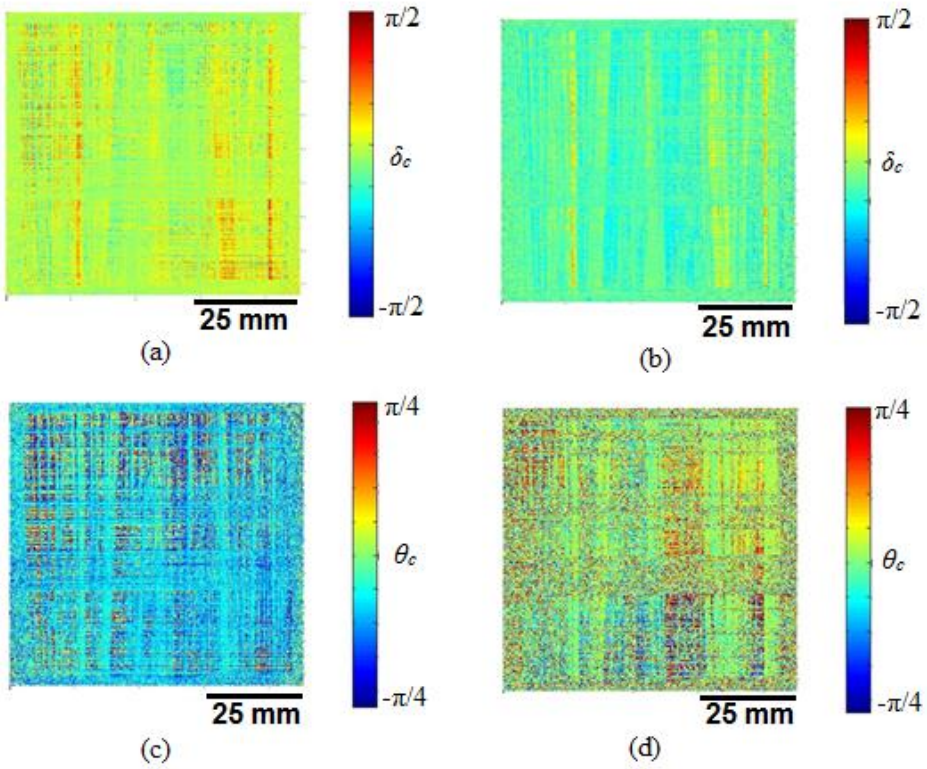

Figure 6-8: Phase retardation of EFG sample from (a) 6-step and (b) 10 step algorithm; isoclinic angle from (c) 6-step and (d) 10-step algorithm.

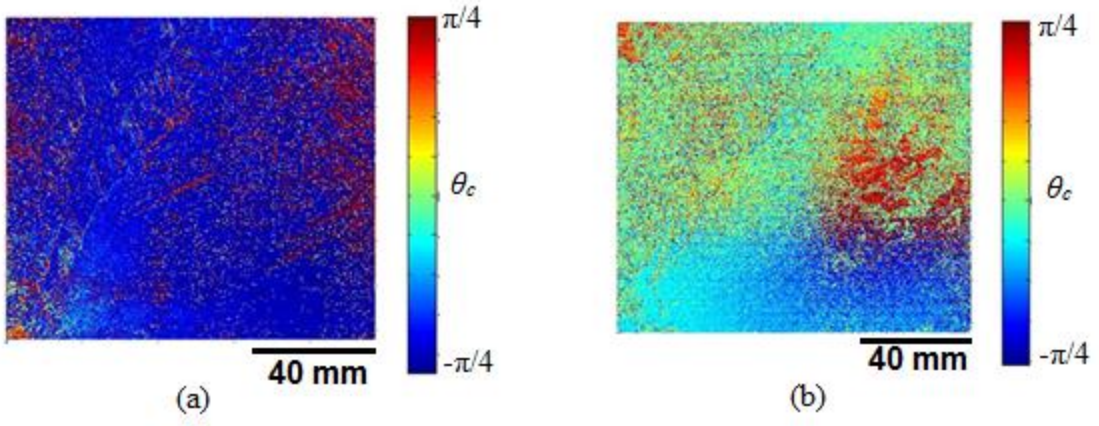

Figure 6-9: Isoclinic angle of cast sample from (a) 6-step and (b) 10-step algorithm.

The isoclinic angle of both the EFG and cast wafers varies considerably between the two techniques. For the cast wafer, the Patterson and Wang 6-step method returned a value of $-\pi/4$ or $\pi/4$ for fully 26% of the wafer surface, a direct result of low retardation levels causing zero to appear in the denominator of Equation (15). Examination of Figure 6-9 reveals that an even greater percentage of the wafer area is within a few degrees of either extreme. In contrast, the 10-step method resolves 46% of the wafer area to an isoclinic angle of zero, while only 8% is evaluated as $-\pi/4$ or $\pi/4$. The results from the 10-step method not only greatly reduce noise accumulation during integration-based stress separation techniques, but also make more sense from a physical standpoint. A stress of zero magnitude should not have a non-zero direction.

6.3 Quality-guided phase unwrapping

The methodology used for obtaining the isoclinic parameter gives results from the range of $[-\pi/4, \pi/4]$. However, the isoclinic parameter itself has a range of $[-\pi/2, \pi/2]$. With this in mind, the evaluated isoclinics must be unwrapped to the correct values.

Recognition of this problem is relatively recent, and the first unwrapping attempts relied on a simple raster scanning method [43-46]. These algorithms are extremely susceptible to noise effects which may cause them to fail. Phase tracking was developed by Quiroga and Gonzalez-Cano [47], which is successful but computationally expensive and requires a precisely weighted costing function. Quality guided unwrapping was first developed for other optical techniques [48], but has been seen more often in photoelasticity in recent years. Ramji and Ramesh [49-50] have created an adaptive quality-guided phase unwrapping technique which unwraps the entire isoclinic map in a single step, which will be discussed further.

This adaptive quality guided unwrapping begins with a determination of the quality of the entire isoclinic map. The quality map generated is essentially a measure of the statistical variance of the phase derivatives, and is defined below.

$$\frac{\sqrt{\sum\left(\Delta_{i,j}^{x}-\bar{\Delta}_{m,n}^{x}\right)^{2}}+\sqrt{\sum\left(\Delta_{i,j}^{y}-\bar{\Delta}_{m,n}^{y}\right)^{2}}}{k^{2}} \tag{17}$$

Each center pixel with coordinates *m, n* is defined by a *k* x *k* neighborhood of surrounding pixels. Each pixel in the *k* x *k* neighborhood is covered by the indices *i, j*. $\Delta_{i,j}^{x}$ and $\Delta_{i,j}^{y}$ are defined as follows.

$$\Delta_{i,j}^{x}= W_{i+1,j} - W_{i,j} \tag{18}$$

$$\Delta_{i,j}^{y}= W_{i,j+1} - W_{i,j} \tag{19}$$

W are the wrapped phase values. $\bar{\Delta}_{m,n}^{x}$ and $\bar{\Delta}_{m,n}^{y}$ are the averages of the partial derivative values in the *k* x *k* window centered upon the pixel *m, n.* This quality map is unique in that it determines the "badness" of the data, which must then be negated to

represent “goodness.” Figure 6-10 illustrates the difference between “bad” and “good” data.

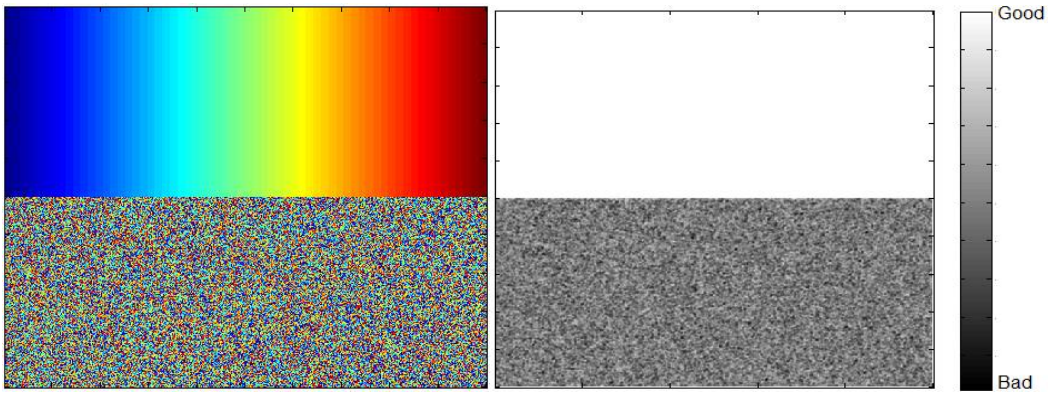

(a) (b)

Figure 6-10: (a) Data map and (b) accompanying quality map.

The top half of Figure 6-10(a) is not noisy and contains a consistent trend. As such, it is rated at maximum quality in Figure 6-10(b). The bottom half of the data, however, is quite noisy and is rated poorly in the quality map.

Once the quality of the entire sample has been determined, the highest quality pixel is chosen as the starting point for the unwrapping process. Figure 6-11(a) shows the wrapped isoclinics from a ring under diametral compression, and Figure 6-11(b) displays the accompanying quality map. From there, the immediately surrounding pixels are examined, and the highest quality neighbor is chosen for the next unwrapping step. As pixels are unwrapped, they are removed from consideration for the rest of the process. The entire spatial domain is thus unwrapped, beginning with the highest quality data and ending with the lowest. This reduces the likelihood that noisy areas of data will corrupt the unwrapping process. Figure 6-11(c) and Figure 6-11(d) compare the unwrapped

isoclinics with the theoretical solution. Figure 6-11 is reproduced from Ramji and Ramesh's work [50].

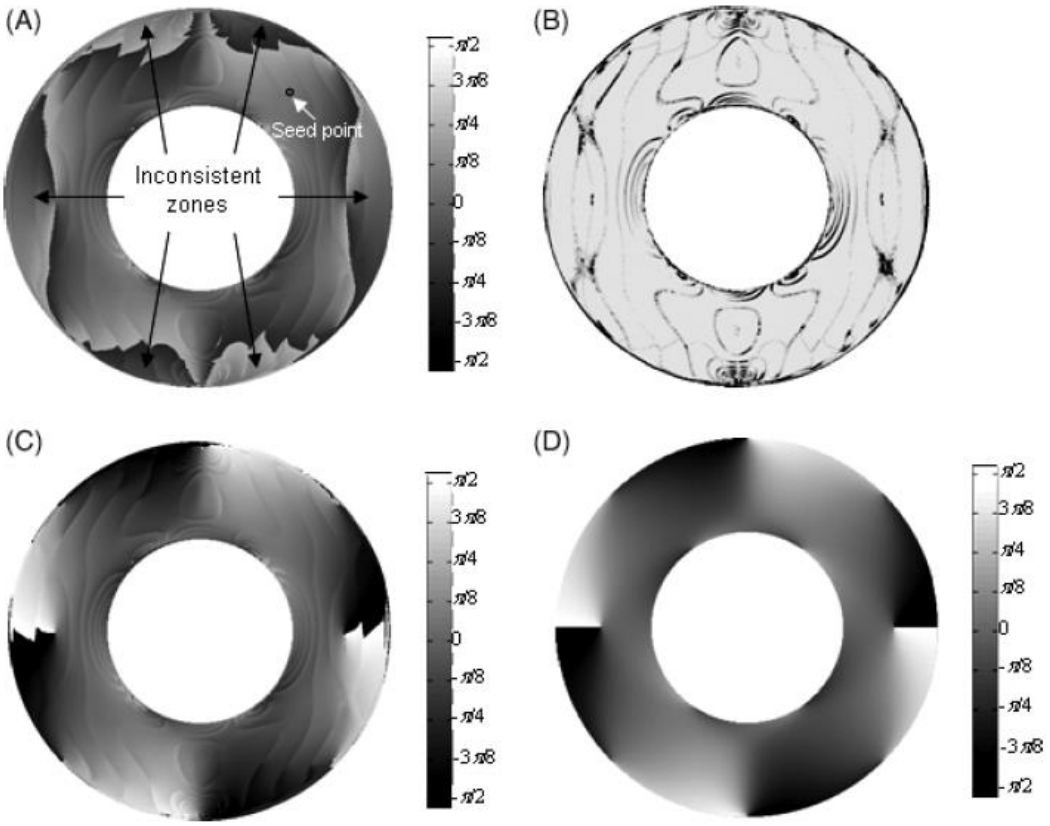

Figure 6-11: (a) Wrapped isoclinics, (b) quality map of wrapped isoclinics, (c) unwrapped isoclinics, (d) analytical solution.

6.4 Conclusions

The 10-step phase shifting algorithm is an improvement over the Patterson and Wang method, reducing isoclinic oscillation by 60% and decreasing noise levels in the evaluated isoclinic map. Quality guided phase unwrapping can successfully unwrap complex isoclinic schemes while maintaining low levels of noise accumulation in the isoclinic parameter. It is this method that was chosen in this thesis.

CHAPTER 7
STRESS SEPARATION

7.1 Shear difference method

While photoelasticity directly provides maximum shear stress data through the stress-optic law, this data is of limited use. Maximum shear stress τ_{max} is the absolute value of the difference between the two principal stresses σ_1 and σ_2, or the largest and smallest stresses. To fully understand the stress state of the sample, the τ_{max} data must be first converted into the yx-plane shear stress τ_{yx} via the following:

$$(\tau_{yx}) = \frac{(\sigma_1 - \sigma_2)\sin 2\theta}{2} \tag{20}$$

The data is then finally separated into the principal normal stresses σ_x and σ_y. Stress separation must be carefully performed to produce accurate results and avoid noise accumulation.

The most common method of stress separation is the shear difference method. This unwrapping technique is based on the equations of equilibrium for a free body. These equations for the x- and y-directions are seen below.

$$\frac{\partial \sigma_y}{\partial y} + \frac{\partial \tau_{xy}}{\partial x} = 0 \tag{21}$$

$$\frac{\partial \sigma_x}{\partial x} + \frac{\partial \tau_{yx}}{\partial y} = 0 \tag{22}$$

Integration of the equilibrium equations results in the following rearrangement:

$$(\sigma_y)_j = (\sigma_y)_i - \int_i^j \frac{\partial \tau_{xy}}{\partial x} \partial y \tag{23}$$

$$(\sigma_x)_j = (\sigma_x)_i - \int_i^j \frac{\partial \tau_{yx}}{\partial y} \partial x \tag{24}$$

The integrals shown above can be easily discretized for numerical assessment.

$$(\sigma_y)_j = (\sigma_y)_i - \sum_i^j \frac{\Delta \tau_{xy}}{\Delta x} \Delta y \tag{25}$$

$$(\sigma_x)_j = (\sigma_x)_i - \sum_i^j \frac{\Delta \tau_{yx}}{\Delta y} \Delta x \tag{26}$$

As is the case in any type of equilibrium equation, boundary conditions must be supplied for the beginning of the integration. The most widely accepted form of the shear difference method is to begin from an edge, or free boundary, and integrate across the surface of the sample. The procedure is illustrated below in Figure 7-1.

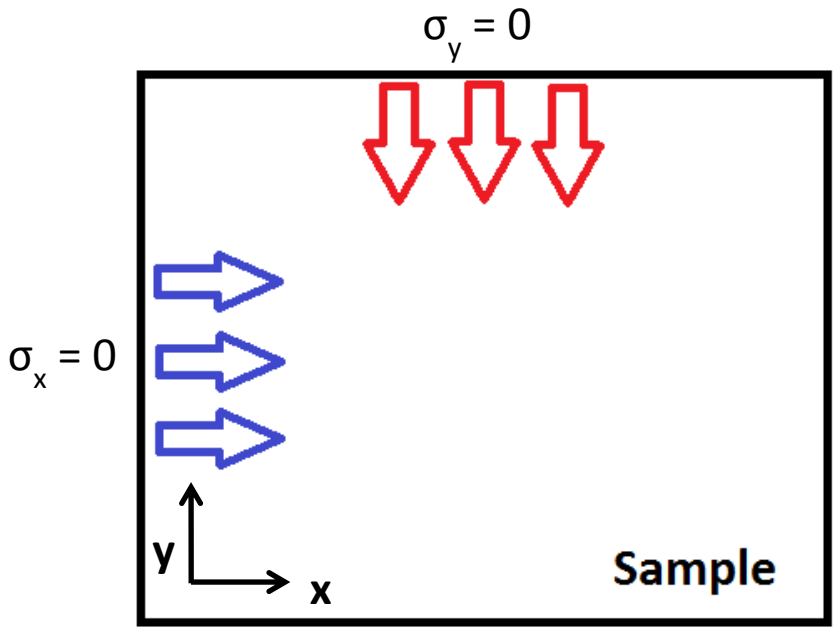

Figure 7-1: Schematic diagram of the shear difference integration method from a free boundary.

By definition, σ_x and σ_y must respectively be 0 at the x and y free boundaries. This provides a starting point for the shear difference integration process, which then separates the maximum shear stress τ_{max} into the normal stress components σ_x and σ_y moving away from the edge.

Use of a free boundary creates simple boundary conditions but also imposes limitations on the shear difference process. Obviously, the edges of the sample must be included in the analysis domain for the free boundary conditions to be valid. The accuracy of the method across multicrystalline materials is also questionable, since different grains may be defined by different stress optic coefficients. Finally, noise in the isoclinic parameter causes rapid error accumulation in the integration process, rendering shear difference results nearly impossible after a short distance from the edge.

7.2 Effect of isoclinic parameter on noise accumulation in stress separation

The noise accumulation mentioned above is primarily dependent on the isoclinic parameter. Noise in the isoclinic parameter results in the presence of "streaks" across the sample after stress separation using the shear difference method. Each streak is caused by a large difference in noise accumulation between adjacent integration paths. An example of this streak formation is displayed below in Figure 7-2.

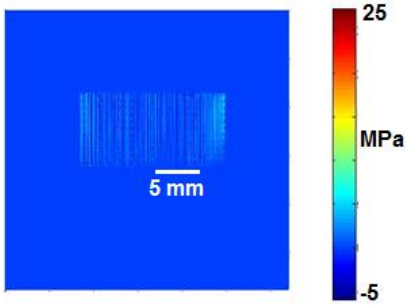

Figure 7-2: Streak formation in σ_y obtained with shear difference integration.

The results shown in Figure 7-2 are from a single crystal CZ beam loaded in in-plane 4-point bending. As such, σ_y should be uniformly zero between the top load points. However, Figure 7-2 shows a significant amount of non-zero stress evaluation in the form of streaks. This behavior is caused by noise in the isoclinic angle, and results in noise of more than 25 MPa present in the normal stress results. Skenes and Prasath found that smoothing the isoclinic parameter before stress separation substantially reduces noise levels in normal stress evaluation [51]. Figure 7-3 shows the same sample as Figure 702 after isoclinic smoothing.

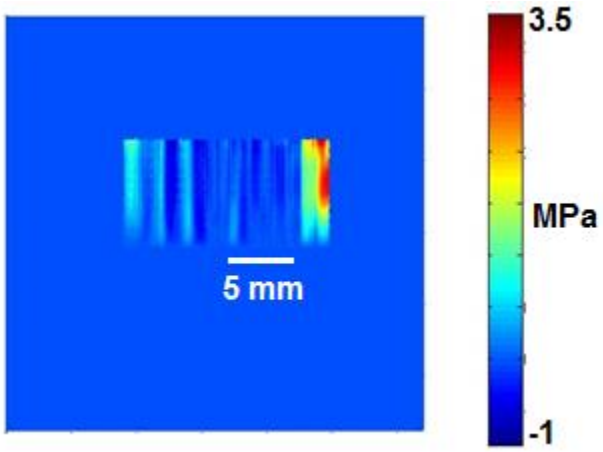

Figure 7-3: σ_y after isoclinic smoothing.

Note that while minor streak behavior is still observable, the magnitude of the noise present has decreased from 25 MPa to 3 MPa, an 88% reduction. The implications of this noise reduction are illustrated to a greater degree in multicrystalline samples. Figure 7-4 shows a comparison between σ_x and σ_y evaluated with unsmoothed and smoothed isoclinics for a multicrystalline silicon bar.

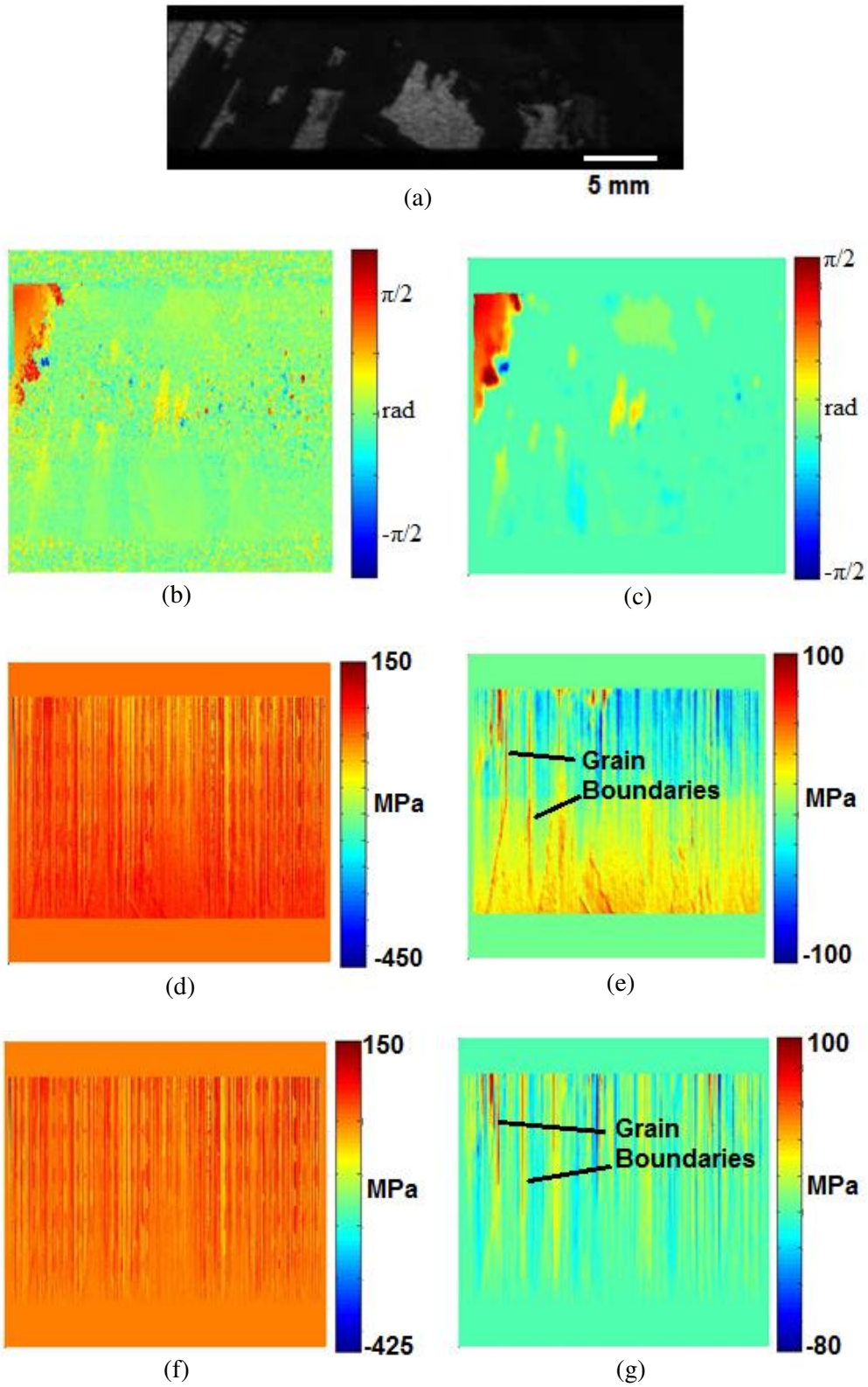

Figure 7-4: (a) NIR transmission image of multicrystalline bar; (b) unsmoothed and (c) smoothed isoclinic angle; (d) σ_x evaluated before and (e) after isoclinic smoothing; (f) σ_y evaluated before and (g) after isoclinic smoothing.

The difference in isoclinic noise between (a) and (b) is quite clear. Furthermore, features such as grain boundaries are visible in the σ_x and σ_y directions after smoothing. These features are hidden by extreme noise levels before smoothing. Comparison of noise levels before and after smoothing reveals a nearly 70% reduction in magnitude. It is important to keep in mind that the procedure for stress separation remains identical in each case, and the smoothing operation is performed on the isoclinic data. While spatial averaging requires the lowest time and computational cost, RMS smoothing remains the most accurate option.

7.3 Use of zero-stress point as boundary condition

The single-crystal CZ wafer shown in Figure 6-3 is assumed to contain very low amounts of residual stress, which is expected for a single-crystal wafer with no applied load. Figure 7-5 shows the maximum shear stress map for the wafer in question.

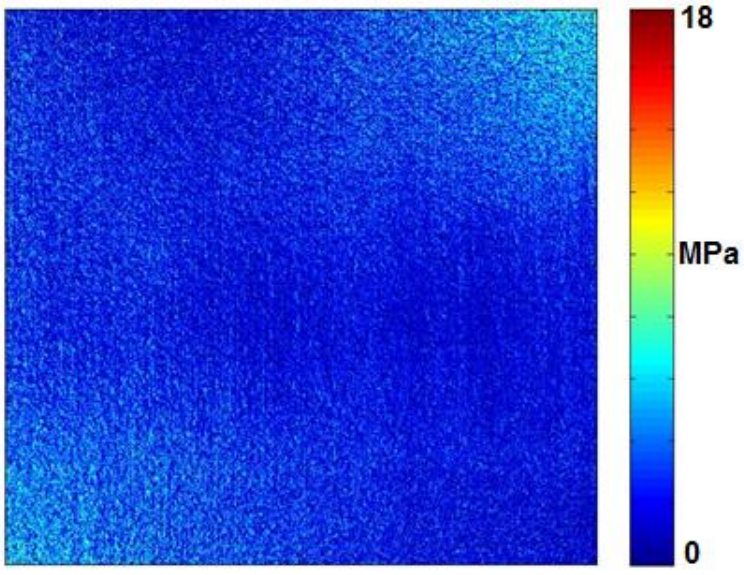

Figure 7-5: τ_{max} map for single-crystal CZ wafer.

Examination of Figure 7-5 shows that a large percentage of the wafer area is evaluated to have a maximum shear stress value of zero. Similar results were shown for the cast multicrystalline wafers in Figure 6-9.

The nature of maximum shear stress (the absolute value of a difference) means that there is an inherent uncertainty in a maximum shear stress of zero. Two cases are possible: Both principal stresses are zero, or both principal stresses are equal and non-zero. This ambiguity has previously only been able to be resolved after the performance of some stress-separation technique such as the shear difference method.

For the case where both principal stresses are equal and non-zero, the point in question is referred to as an isotropic point. This phenomenon was first discussed in detail by Frocht [52]. As an example, Figure 7-6 displays the photoelastic fringes of a polymeric disc in 3-point loading.

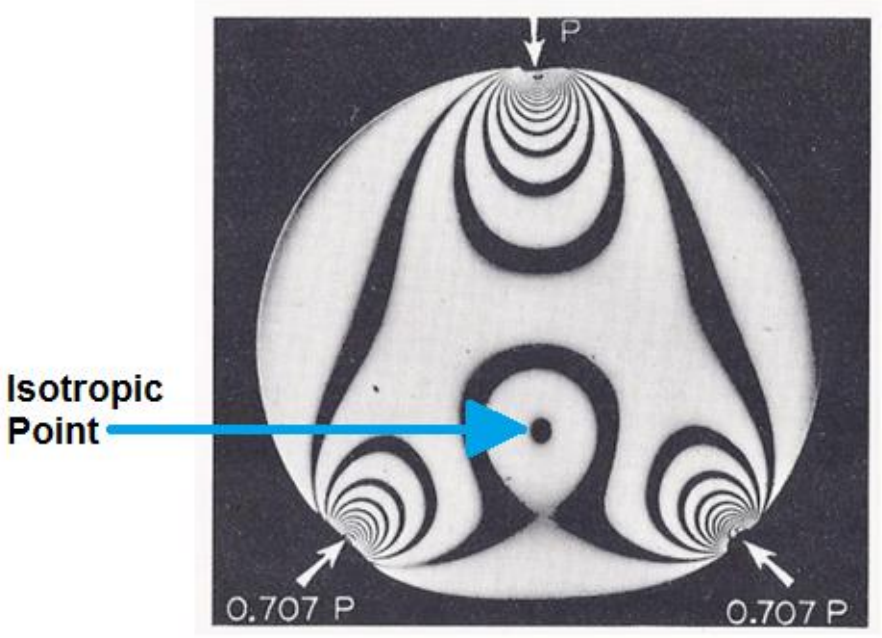

Figure 7-6: Isotropic point in photoelastic fringes of disc in 3-point loading. [52]

Isotropic points such as these are accompanied by a particular isoclinic behavior. The isoclinics rotate around the isotropic point in a manner described by Sears and Zemansky [28] and shown in Figure 7-7.

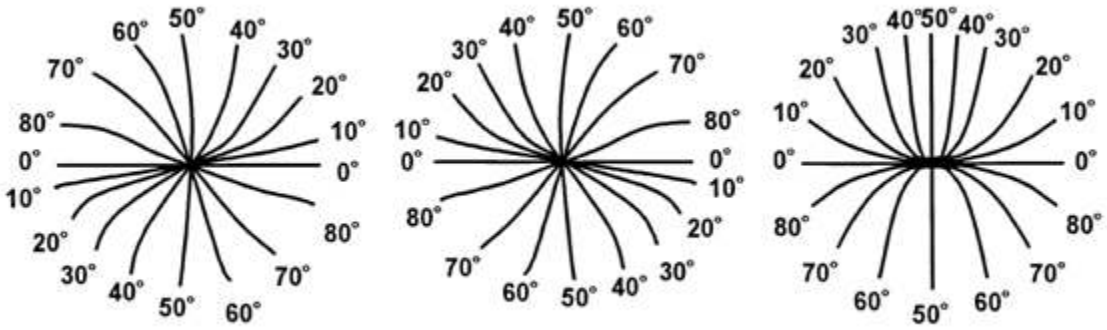

Figure 7-7: Isoclinic rotation behaviors around isotropic point.

While isotropic points are most commonly introduced by applying loads, they can be found in residual stress states. Figure 7-8 presents one such example. A PET sample with large amounts of frozen stresses was found to have one isotropic point on the left side.

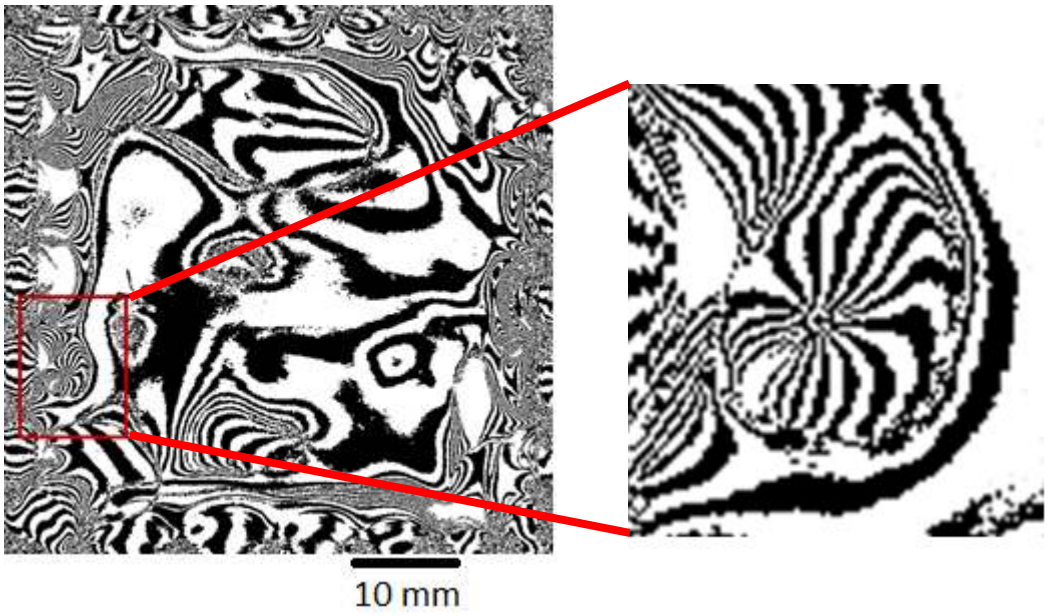

Figure 7-8: Binary isoclinic plot of isotropic point in PET sample.

This rotational isoclinic behavior is key to the analysis of points found to have a maximum shear stress. The PET sample presented in Figure 7-8 is an example of an isotropic point occurring in a residual stress state, and is accompanied by the rotational isoclinic behavior which identifies it as an isotropic point. Examination of isoclinic maps resolves the ambiguity over whether a zero-stress point contains zero normal stresses or equal and non-zero normal stresses. The isoclinic data for a CZ silicon wafer and a cast silicon wafer is presented below in Figures 7-9 and 7-10.

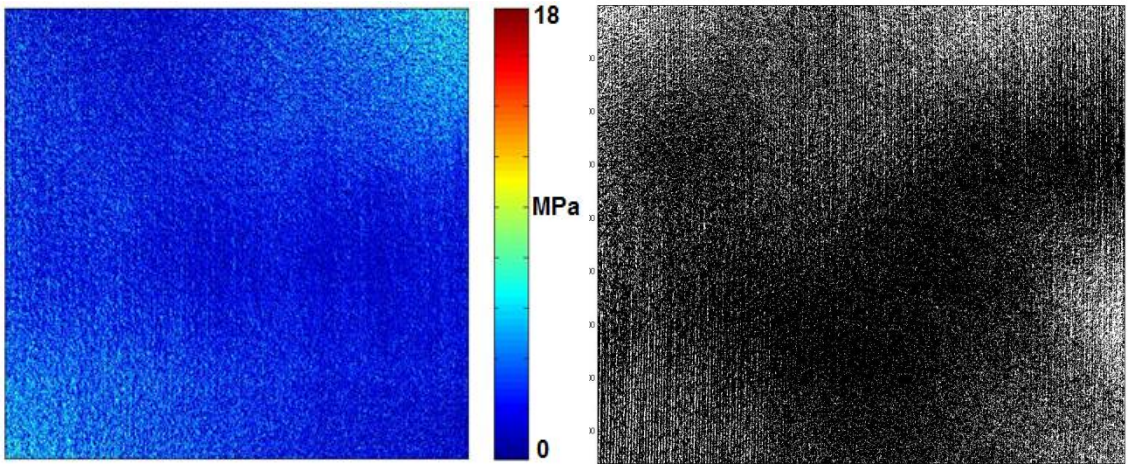

(a) (b)

Figure 7-9: (a) Maximum shear stress, (b) binary isoclinic plot of CZ wafer.

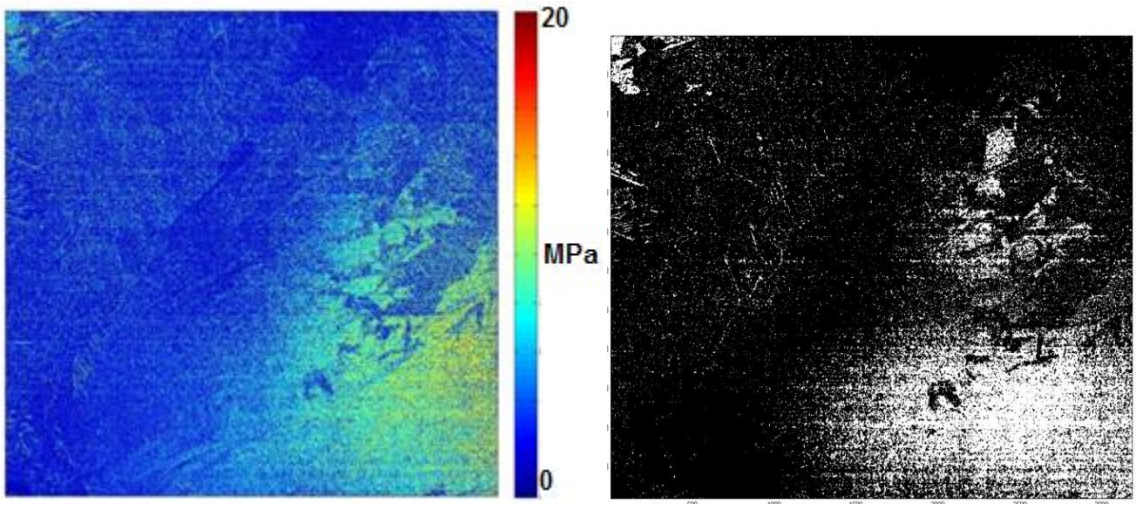

(a) (b)

Figure 7-10: (a) Maximum shear stress, (b) binary isoclinic plot of cast wafer.

The absence of rotational isoclinic behavior is evidence that the zero-stress points in the silicon wafer can be identified as having principal stresses of zero as well as a maximum shear stress of zero. This conclusion has particular significance to the shear difference integration method of stress separation. If the normal stresses at a point are all zero, the point can serve as a satisfactory boundary condition for the start of shear

difference integration. Starting points such as these would allow for successful integration of an area which may not include free boundaries, and would also create the possibility of separate stress separation processes for every grain in a multicrystalline wafer. However, to take full advantage of these new boundary conditions, a change in integration algorithm is needed.

7.4 Quality-guided integration

Current shear difference integration schemes commonly progress along a straight line until a free boundary is reached. While this method is acceptable if integration is being performed from free boundary to free boundary, starting the integration process in the middle of a sample poses challenges. If zero shear stress points are used as starting points for integration, moving in straight lines will result in normal stresses evaluated over a minimal area as shown in Figure 7-11.

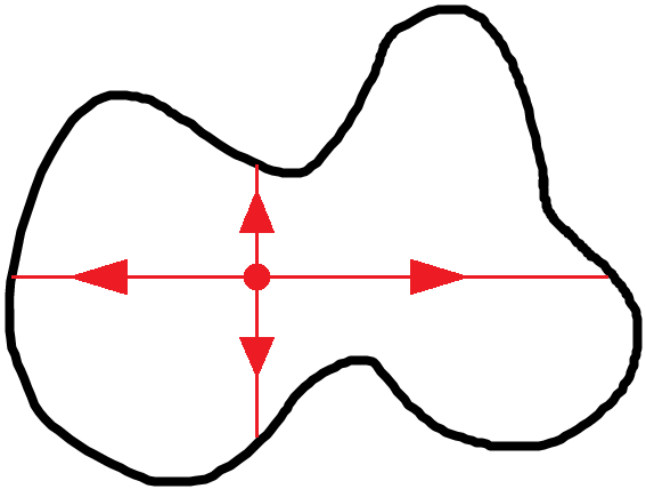

Figure 7-11: Straight-line integration from a starting point in the center of a sample.

The presence of enough zero shear stress points to cover the entire spatial domain of the sample using the scheme illustrated in Figure 7-11 is at best unlikely. A different integration scheme is clearly needed.

Quality-guided phase unwrapping has been discussed in Chapter 6. The main benefits of quality-guided unwrapping are its ability to minimize the effects of noise and determine the best algorithm path for minimizing noise. These two benefits are also applicable to a numerical integration process. This thesis proposes a quality-guided shear difference integration scheme.

The quality of the sample is determined using the procedure outlined in Equation (17). Next, the zero shear stress point is selected as the starting point for stress separation. The highest quality point adjacent to the starting point is identified and used for the next integration step using Equation (25) or (26) as appropriate. Integration proceeds by continuing to identify the highest quality point adjacent to the area which has already been evaluated. The process continues until the entire surface area of the sample has been separated.

There are two main benefits to using a quality-guided integration process. First, the algorithm is able to choose its own path such that the noise levels in the data are minimized. Previously mentioned streak formation is caused by the presence of noisy pixels at the beginning of the integration process. Quality-guided integration saves these noisy pixels for last, ensuring that good data will not be corrupted by adjacent noise. Second, the algorithm allows for the evaluation of an entire irregularly shaped sample from one starting point.

Figure 7-12(a) shows the quality-guided integration results from a single-crystal CZ beam in four-point bending, while Figure 7-12(b) shows the same beam integrated using the standard boundary conditions at the sample's edge.

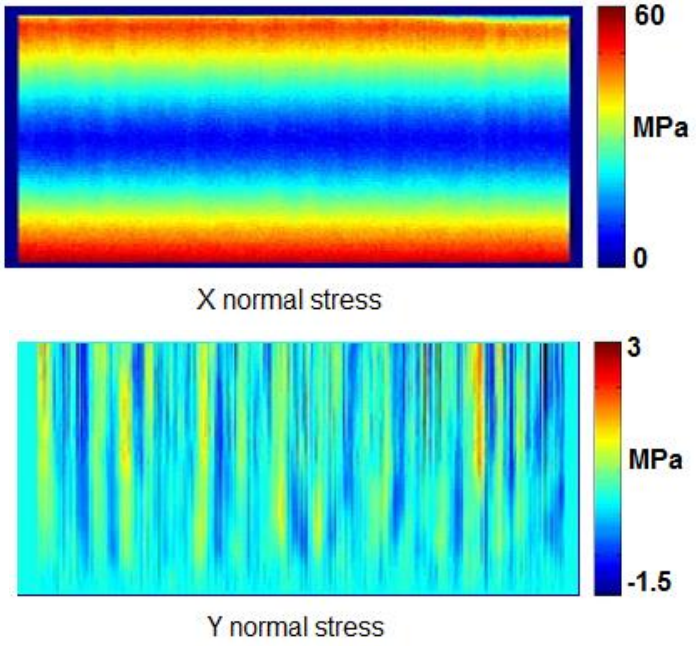

(a)

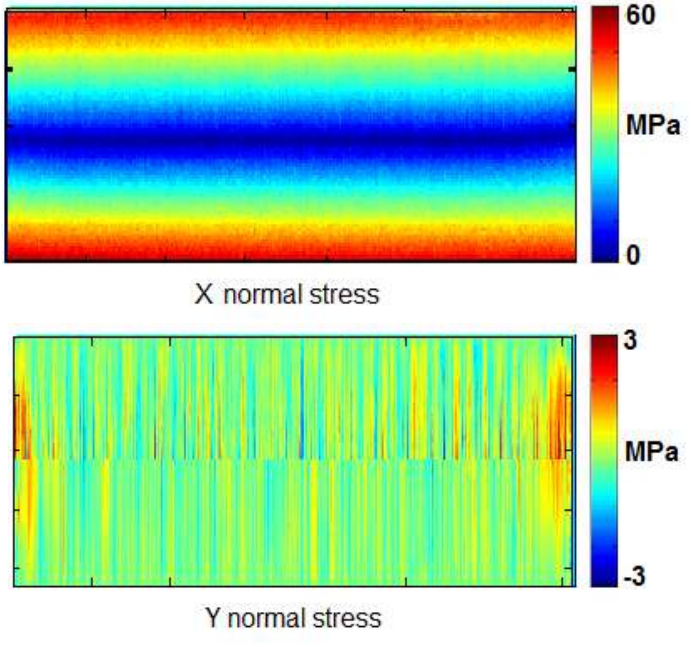

(b)

Figure 7-12: Comparison of (a) quality-guided and (b) straight-line integration.

While four-point bending does not create isotropic points, the normal stresses at the horizontal centerline of the beam are zero, providing a starting point to test the quality-guided integration process. A comparison between the two results demonstrates the accuracy of the quality-guided process. Quality-guided integration can therefore be applied to grains in a multicrystalline wafer with confidence. Figure 7-13 shows stress separation results from one such grain which would be nearly impossible to evaluate without the newly defined boundary conditions and the quality-guided integration algorithm.

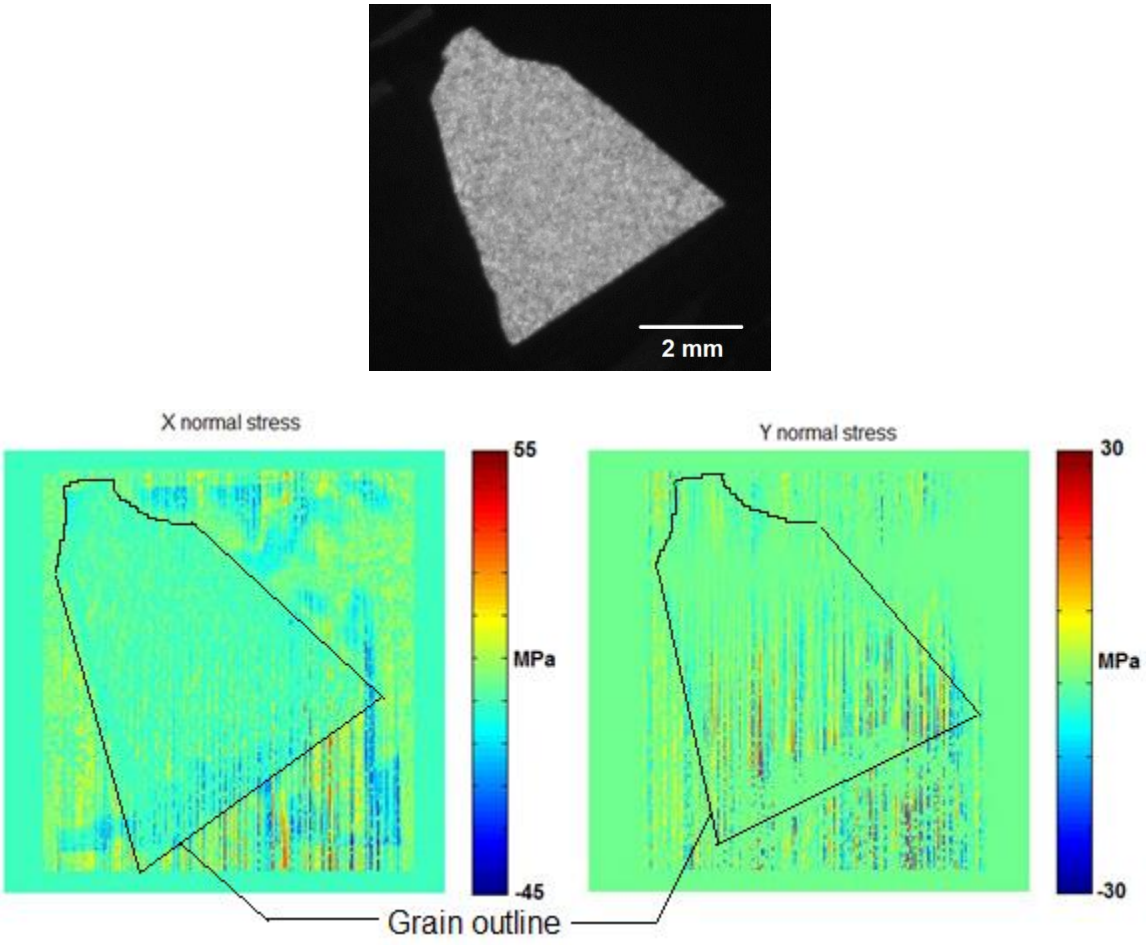

Figure 7-13: Quality-guided stress separation of silicon grain.

Stress separation of the grain in Figure 7-13 would be impossible with the previous integration scheme. The grain is located in the interior of a 156x156 mm wafer. Integration from a free boundary would result in excessive accumulation of noise before reaching the grain in question. The quality-guided integration scheme is not only able to separate the stresses in the grain from a single starting point, but does so in a manner that successfully limits noise accumulation.

7.5 Conclusions

Noise in the isoclinic parameter is a primary contributor to noise accumulation in the stress separation process. Smoothing the isoclinic parameter resulted in a 70% noise reduction in separated normal stresses for multicrystalline silicon bars. Points at which τ_{max} is evaluated to be zero can be determined to be stress-free points by their isoclinic behavior. Stress-free points can be used as boundary conditions for the shear difference stress separation process. Shear difference integration was adapted to a quality-guided process, and was found to be capable of separating an entire spatial domain from one starting point.

CHAPTER 8
APPLICATION TO DEFECTS AND FEATURES IN CRYSTALLINE SILICON

8.1: Four-point bending validation

Prior work by Li [16] and He [38] used in-plane 4-point bending to load single-crystal and multicrystalline silicon beams in order to determine the stress-optic coefficient. The applied stresses in the beam were then used to determine the stress-optic coefficient C and calibrate the NIR polariscope. Replacement of the NIR camera and polarizers in the polariscope warranted another validation experiment.

In-plane 4-point bending imposes stresses on the edges of the sample. Figure 8-1 illustrates the in-plane 4-point bending setup. The load points are roller pins arranged to apply the load as illustrated in Figure 8-1.

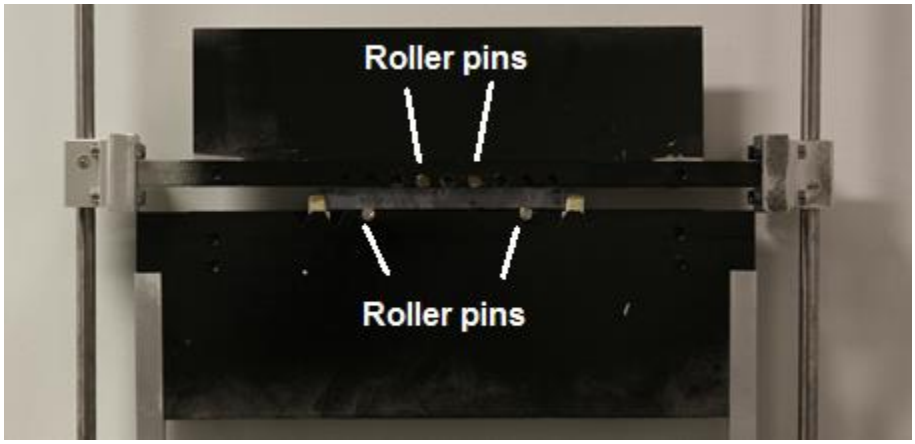

Figure 8-1: In-plane 4-point bending apparatus.

Figure 8-2 shows the free body diagram, shear stress, and moment diagrams of the setup. Normal stresses are created along the x-direction only.

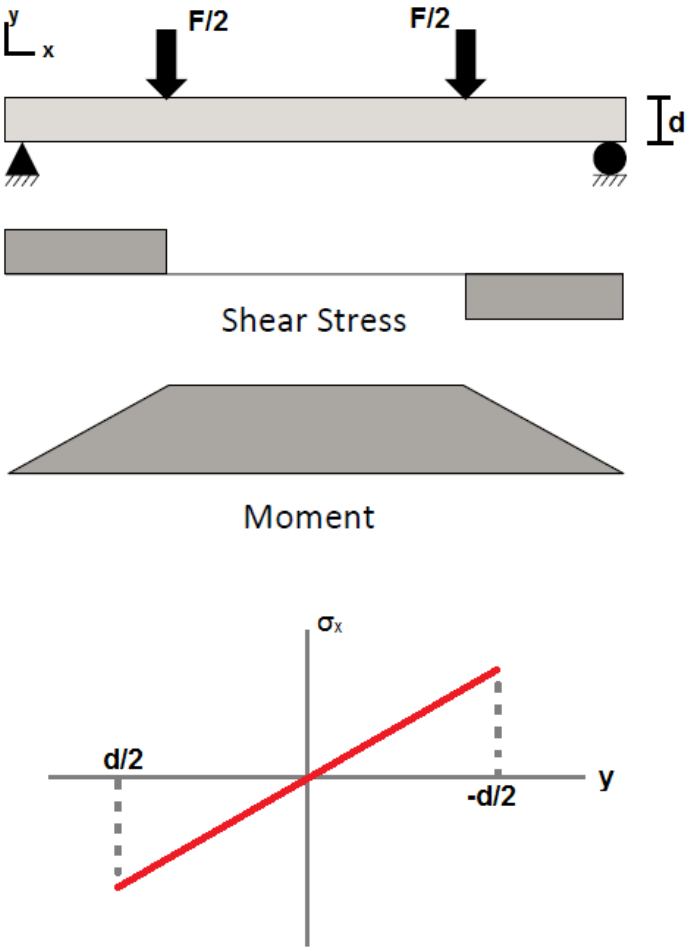

Figure 8-2: Free body diagram, shear stress, moment diagram, and σ_x of a beam in 4-point bending.

Between the inner load points, σ_y is zero while σ_x behaves as illustrated. The maximum value of σ_x occurs at the bottom of the beam and is determined using Euler-Bernoulli beam theory:

$$\sigma_x = \frac{3F(L - L_i)}{2bd^2} \tag{27}$$

Where b is the beam thickness and L and L_i are the distances between the outer and inner load points, respectively.

Figure 6-2 shows the bright-field transmission image of a single-crystal P-type, 8 mm wide, 200 μm thick CZ beam loaded in this manner. The beam was loaded to a normal stress σ_x of 43 MPa, or a maximum shear stress τ_{max} of 21.5 MPa. Figure 8-3 shows the maximum shear stress, x-normal stress, and y-normal stress evaluation results from the loaded beam.

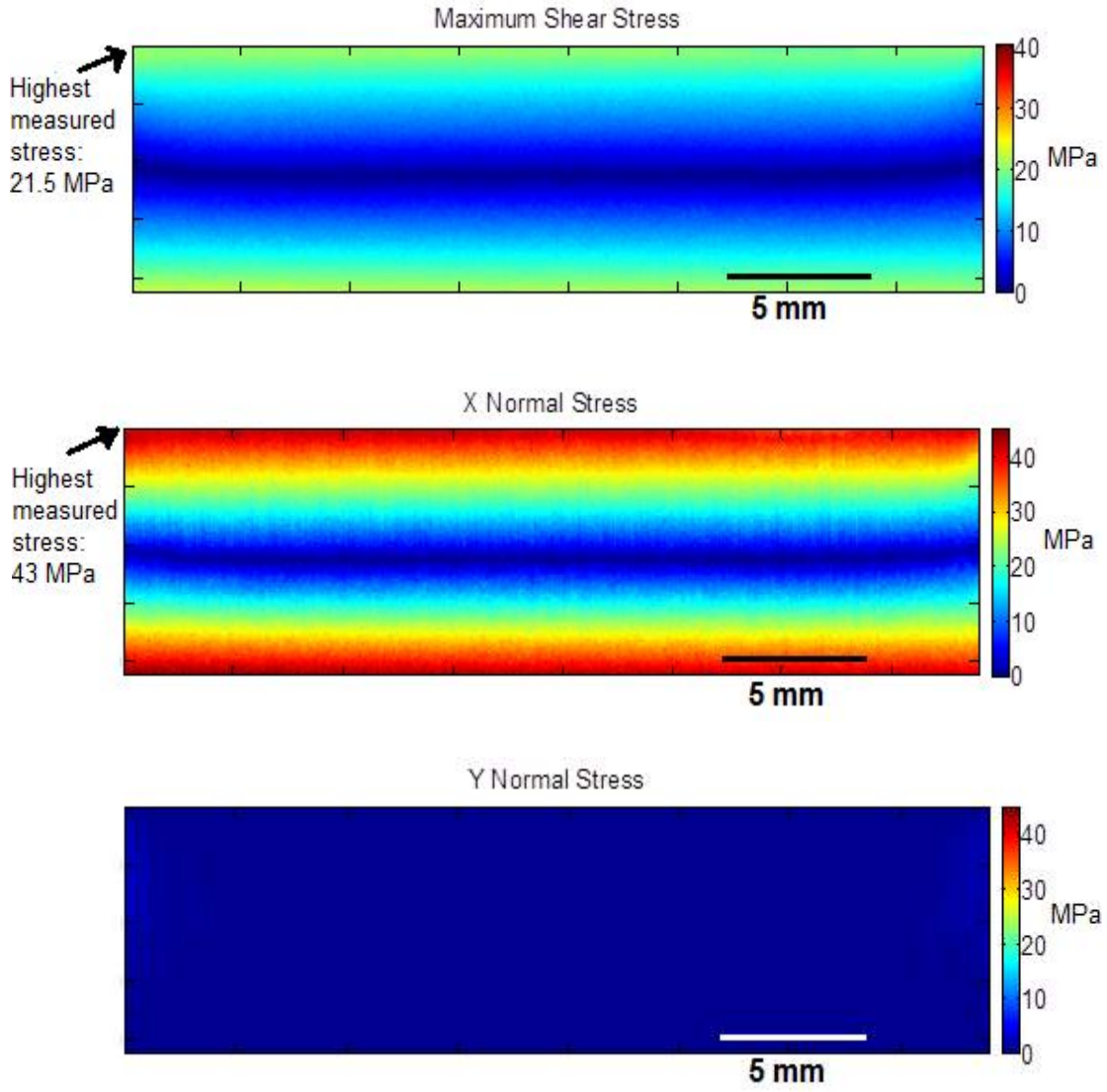

Figure 8-3: Stresses in single-crystal CZ beam in 4-point bending.

The results for the normal stress σx show a maximum value of 43 MPa and a linear progression such as the one in Figure 8-2. The experimentally measured results taken from any point on the beam agree within 1 MPa of analytically determined stress values calculated from Equation (27). The stress-optic coefficient is related to the slope $d\delta/dy$, which can be determined by plotting the retardation δ against the vertical location relative to the neutral axis of the beam as seen in Figure 8-4.

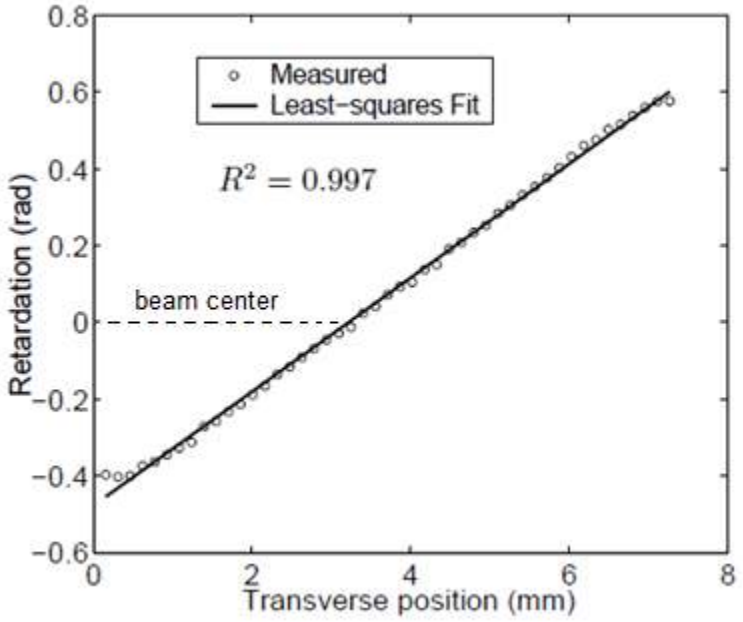

Figure 8-4: Retardation (rad) vs. y-position (mm) on a CZ beam in 4-point bending. [15]

The R^2 value for the line fitted to the data points is 0.997, indicating an extremely close data fit. The measured slope of the least-squares fit is then used to find C:

$$C = \frac{d\delta}{dy} \Big/ \frac{2\pi t}{\lambda} \frac{M}{I} \tag{28}$$

The beam is in a state of pure bending between the inner load points, which implies a σ_y of uniformly zero. This is accurately represented in the experimental results.

While there is some noise in the normal stress results due to the integration process, noise levels are on the order of ~3 MPa and do not interfere with the interpretation of the data.

However, it is also important to note that for the normal stress σ_x to be evaluated in a completely correct manner, the stresses above the centerline of the beam would be characterized as compressive or negative. The maximum shear stress value τ_{max} is the absolute value of the difference between the two principal normal stresses. No reliable method currently exists for determining whether the normal stresses are compressive or tensile during stress separation. While Li's previous research [16] uncovered a solution for the positive/negative stress separation question, the proposed solution was found to apply only to a narrow range of cases and was not used in this thesis.

8.2: Residual stresses surrounding Vickers indentations in CZ wafers

Cracks are an indication that residual stresses in wafers have been relieved. These cracks may be generated by stresses encountered in handling or manufacturing. Creating controlled cracks in silicon wafer is difficult, especially in thin, brittle wafers. One successful way to accomplish this is to use a pyramidal diamond to create an indentation in the surface of the wafer. This indentation will then be surrounded by a predictable crack and stress network. The stresses surrounding these cracks can then be predicted analytically or numerically and compared with experimental results from the polariscope. Figure 8-5 shows a typical example of a Vickers indentation in a polished CZ silicon wafer.

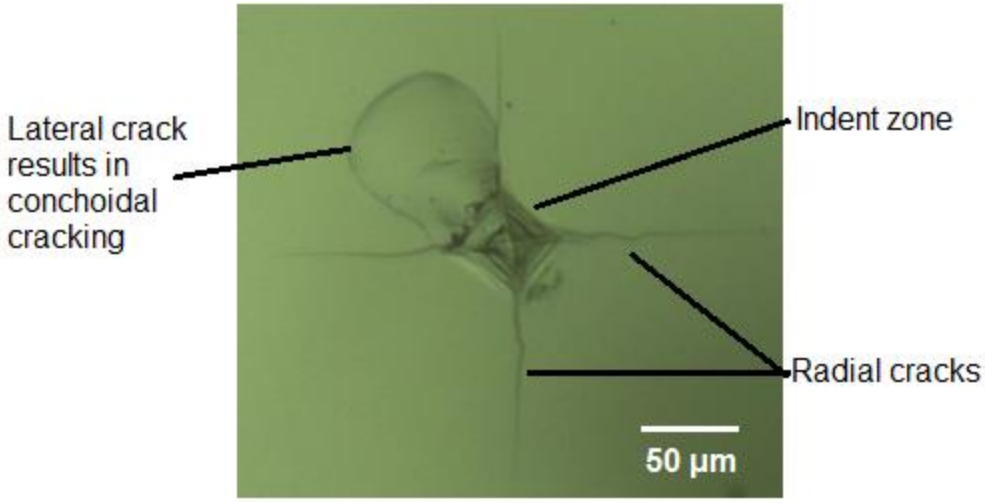

Figure 8-5: Optical micrograph of a Vickers indentation in single-crystal P-type semiconductor-grade CZ silicon wafer.

A Buehler microhardness tester equipped with a Vickers indenter was used for the creation of indentations and accompanying crack fields. The Vickers indenter, illustrated below in Figure 8-6, is a square pyramid with an included angle of 136º.

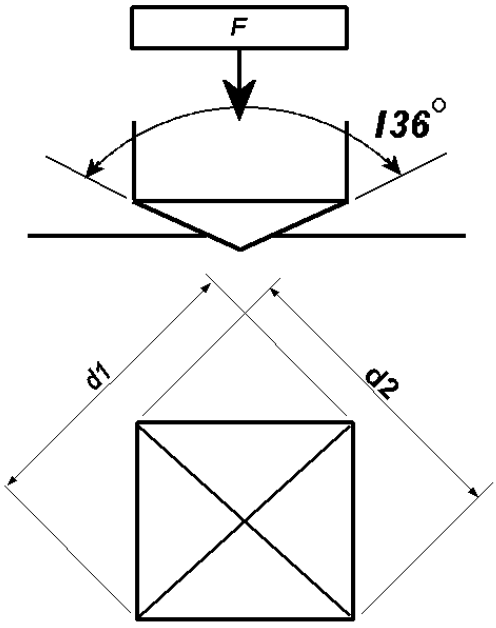

Figure 8-6: Diagram of Vickers indenter.

Indentation is a dynamic process. Compressive stresses are generated during loading, resulting in dislocations. During unloading, tensile stresses produce cracks such as those seen in Figure 8-5. After creating an indentation in the material surface, the length of the diagonals d1 and d2 of the indentation are used to determine the hardness of the material. For the purposes of this research, cracks and stresses surrounding the indentation have been evaluated.

Indentations were created in single-crystal CZ wafers of [100] crystallographic orientation. The wafers were 200 μm thick and had been etched to remove surface damage and debris from the wafering process. Average residual τ_{max} levels in the wafers were found to be 3.5 MPa before indentation. An oil film was placed on an etched wafer surface prior to indenting with a 2 N load. The diagonals of the Vickers diamond were aligned with edges parallel to the (110) plane. Figure 8-7 shows optical microscopy of one resulting indentation.

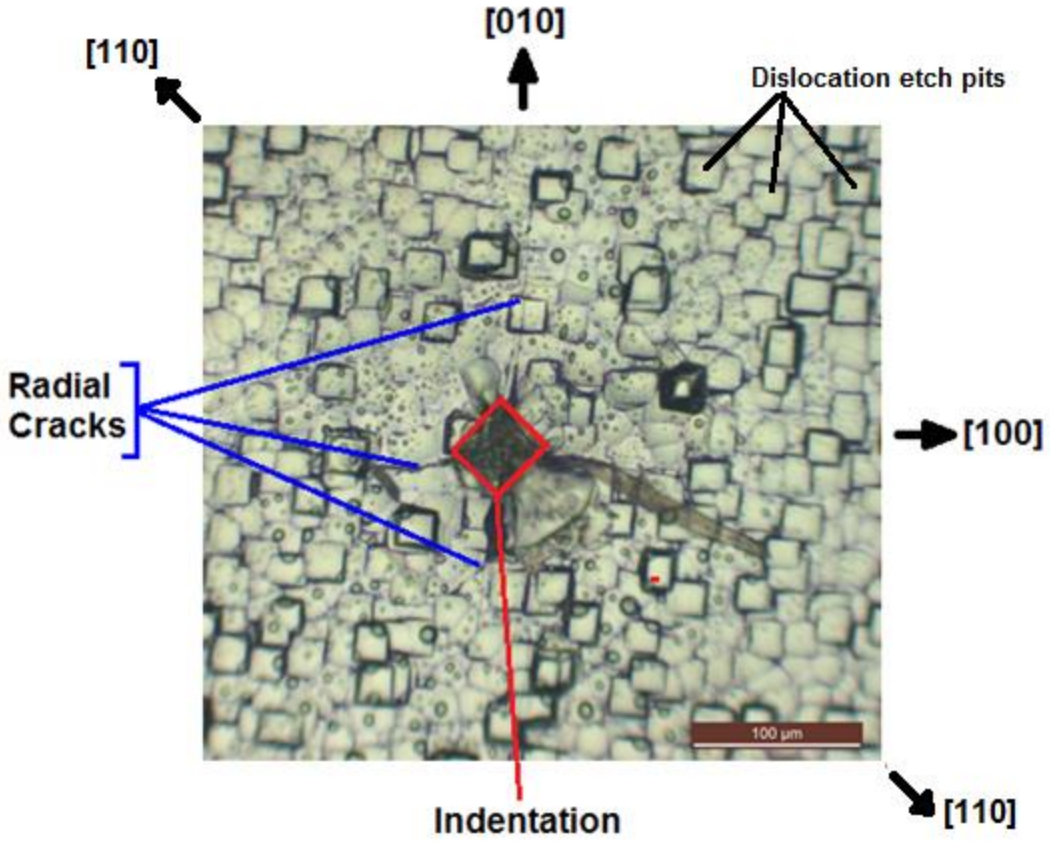

Figure 8-7: Optical micrograph of Vickers indentations in an etched [100] CZ wafer.

Multiple indentations were placed in a 4x4 array with a 2.5 mm space between each. NIR transmission images of two of these indentations are shown below.

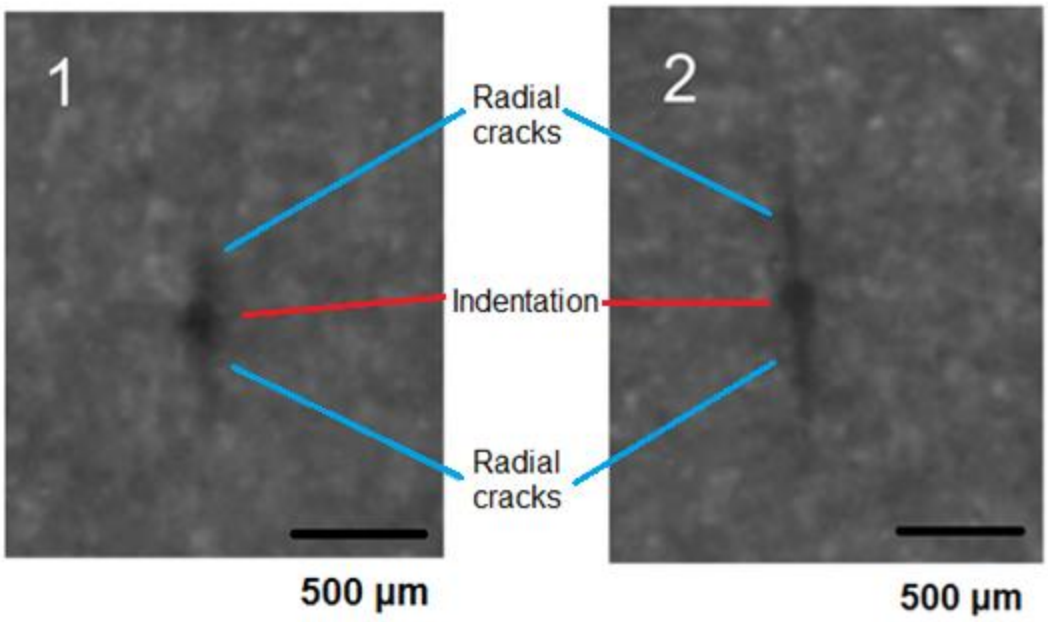

Figure 8-8: NIR transmission images of two Vickers indentations in single-crystal CZ silicon wafers.

Radial cracks extending from the corners of the indentation can be seen in the NIR transmission images. Each indentation was accompanied by a stress field of similar size, shape, and magnitude, as would be expected of indentations produced under near-identical conditions. The stress fields from the examples above are shown below in Figure 8-9. NIR images of the indentations have been placed next to the stress maps for comparison of features and areas of stress.

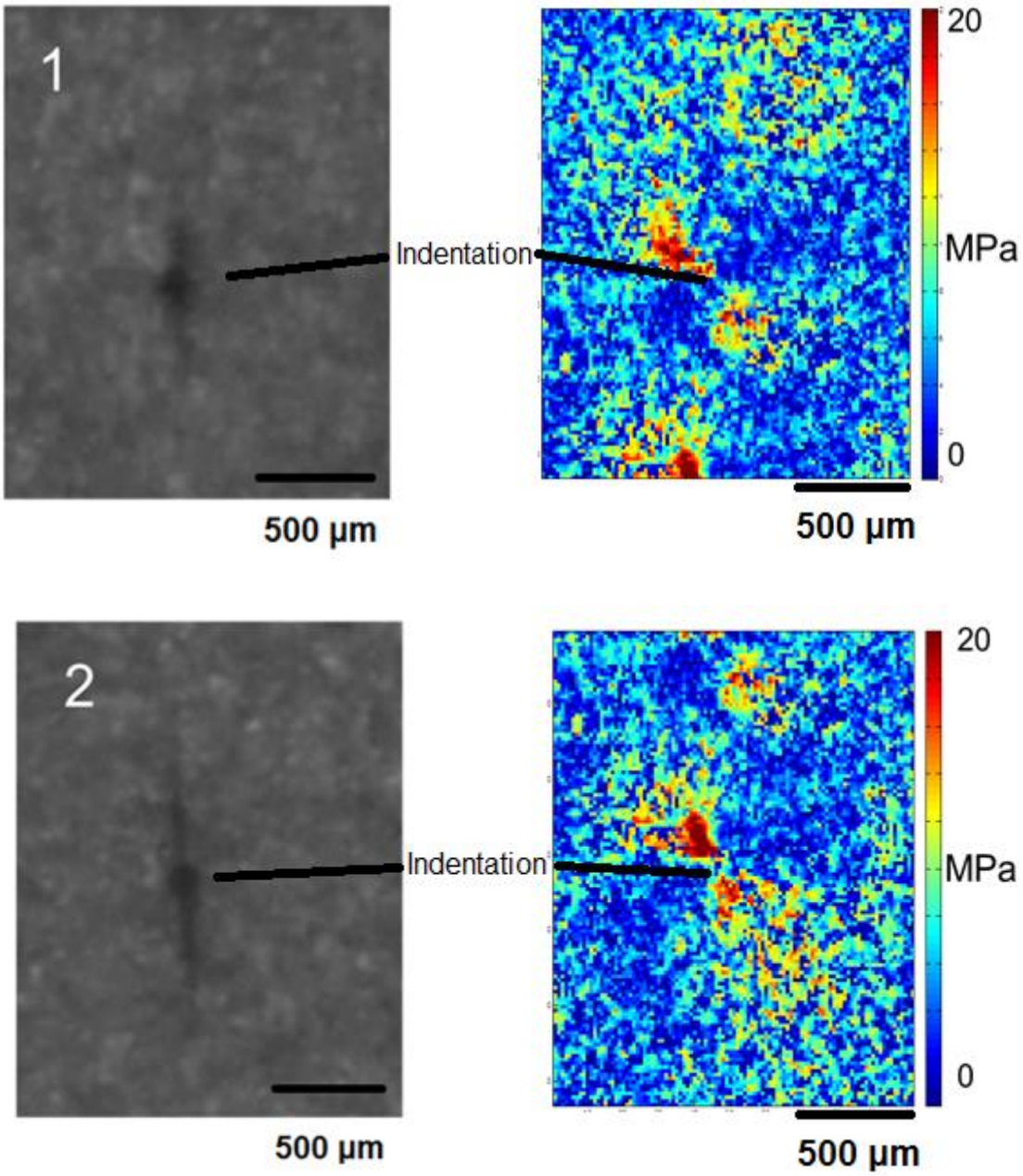

Figure 8-9: τ_{max} stress fields surrounding Vickers indentations.

The size, shape, and magnitude of the stress field surrounding each indentation are similar. The high-stress spots at the bottom of indentation (1) and at the top of indentation (2) are the stress fields from nearby indentations. Figures 8-10 and 8-11

present data on the size and magnitude of 16 indentations in the CZ [100] wafer. Each pixel in the affected zone is equal to an 18 x 18 μm square on the wafer surface.

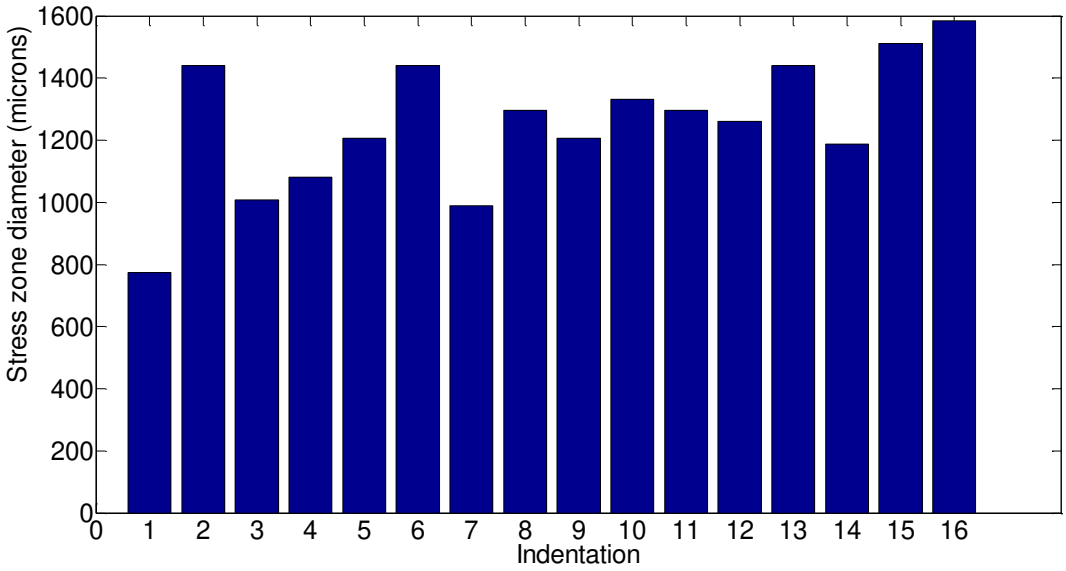

Figure 8-10: Diameter of affected zone (microns) around Vickers indentations in CZ silicon wafer.

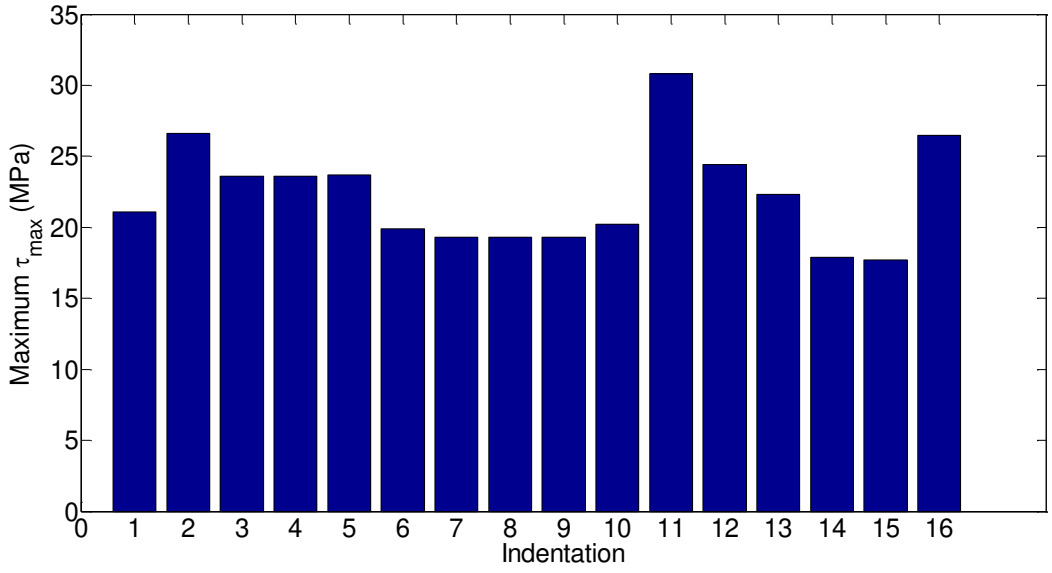

Figure 8-11: Highest τ_{max} stress (MPa) around Vickers indentations in CZ silicon wafer.

The extent of the affected zone was found by calculating the maximum size of a circle enclosing the area affected by the indentation. The "affected zone" was determined by marking pixels which were evaluated to have a τ_{max} value of 10 MPa greater than the residual stress in the wafer before indentation. Any area where the concentration of these pixels was greater than the unstressed wafer was included in the "affected zone." Figure 8-12 shows the "affected zone" of indentation 2 in Figure 8-9. The indentation is marked in black in the center of the circle.

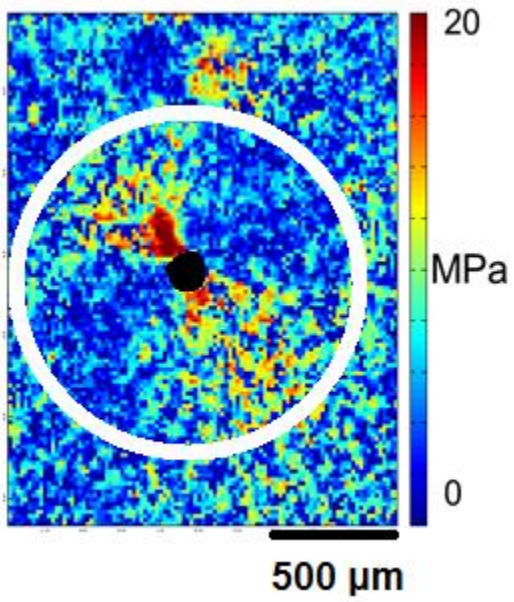

Figure 8-12: Determining the diameter of the stress-affected zone of an indentation.

The diameter of the area affected by the indentation is on the order of ~1 mm for every indentation. There is some variation in size and highest magnitude of the stress field, which can be explained by the fracture of silicon during the formation of cracks. A missing "chip" can be seen immediately below and to the right of the indentation in Figure 8-7. Variations in this behavior would be expected to affect residual stress levels

in the remaining material. Table 8-1 summarizes the results seen in Figures 8-10 and 8-11.

Table 8-1: Summary of indentation data.

	Mean	Standard Deviation
Stress Zone Diameter (μm)	1253.3	214.3
Maximum τ_{max} level (MPa)	22.3	3.6

It is reasonable to conclude from this data that a 2 N force in the form of a Vickers indentation creates a stress field which is considerably larger than the indentation itself. Examination of Figure 8-7 reveals that the indentation diagonals are only ~30 μm long, while the stress field created is nearly two orders of magnitude larger in diameter. The stresses created are also significantly higher than the surrounding area. Residual τ_{max} stresses in a single-crystal CZ wafer are normally on the order of 2-3 MPa. The maximum τ_{max} stresses shown in Figure 8-9 are surrounded by a larger area of stresses in the 15-20 MPa range, significantly higher than the unaffected wafer area.

8.3: Effects of proximity between Vickers indentations in CZ wafers

Arrays of 16 Vickers indentations in a 4x4 configuration were created in (100) CZ p-type wafers using the Buehler microhardness tester. The indentation load was set to 2 N, and an oil film was used to ensure consistent interface conditions between the Vickers diamond and the wafer surface. The spacing between indentations was set to 2.5 mm for the first array, 1.25 mm for the second array, and 0.65 mm for the third array.

The indentations in the 2.5 mm spacing array were each surrounded by a clearly defined residual stress field. Effects of adjacent indentations on the individual stress fields were minimal. Moreover, there is minimal cumulative effect on the wafer area surrounding the entire array. The average residual stress level of the wafer surrounding the indentation array remains unchanged with the exception of the area closest to the perimeter indentations. Figure 8-13 shows the residual stresses of the entire array along with the immediately surrounding wafer area.

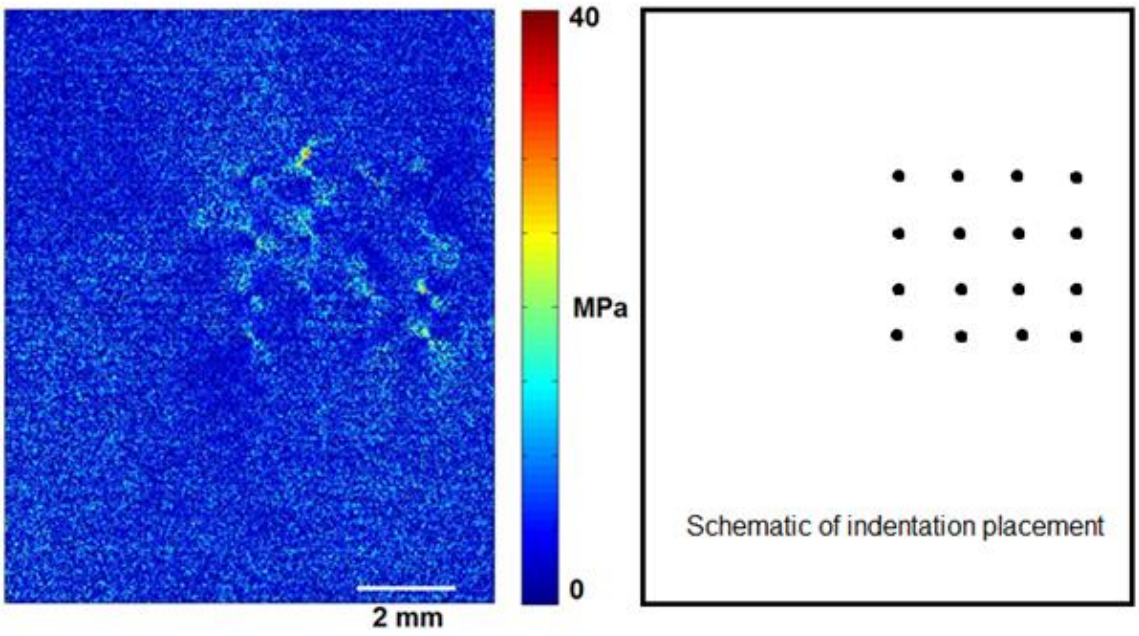

Figure 8-13: Schematic diagram and residual stress field τ_{max} surrounding an indentation array of 2.5 mm spacing.

Figures 8-13, 8-14, and 8-15 show that decreasing the spacing between indentations produces noticeable secondary effects. The stress fields of each individual indentation begin to interact, and much higher stress levels are found inside the array perimeter. Figures 8-14 and 8-15 display the stress levels around the two arrays with

closer indentation proximity. Maximum shear stress levels of nearly 50 MPa were found surrounding individual indentations.

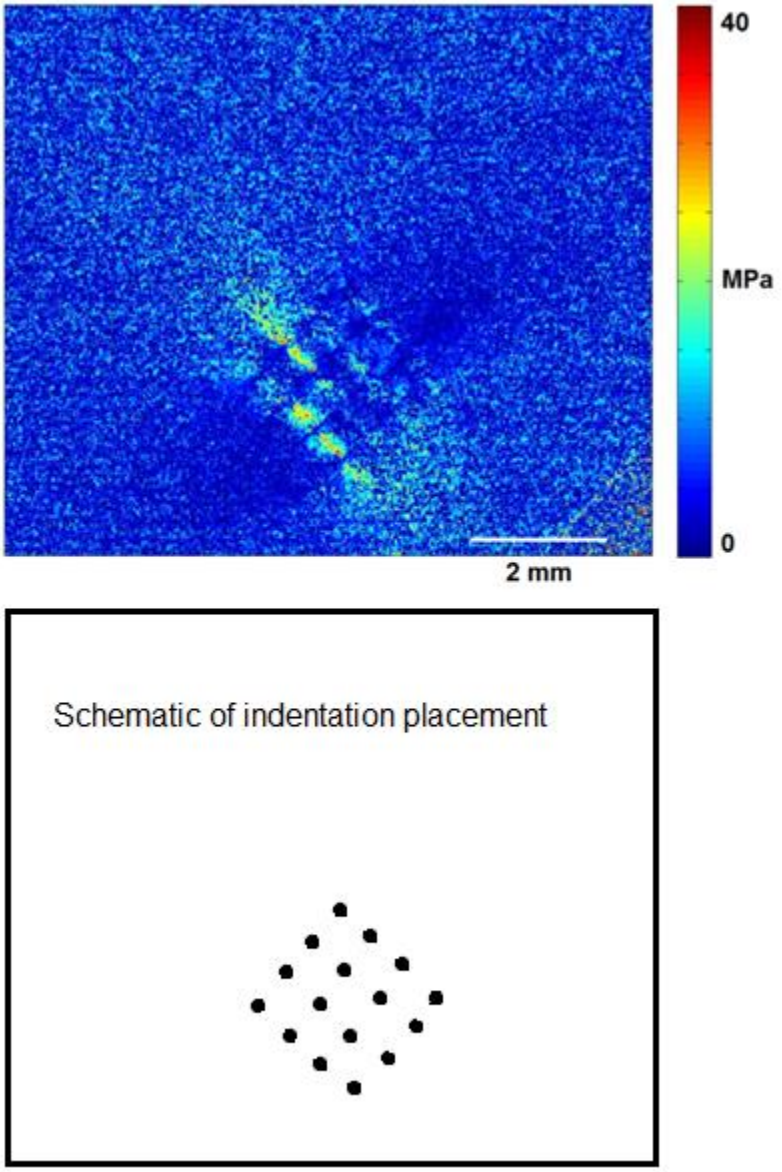

Figure 8-14: Schematic diagram and residual stress field τ_{max} surrounding an indentation array of 1.25 mm spacing.

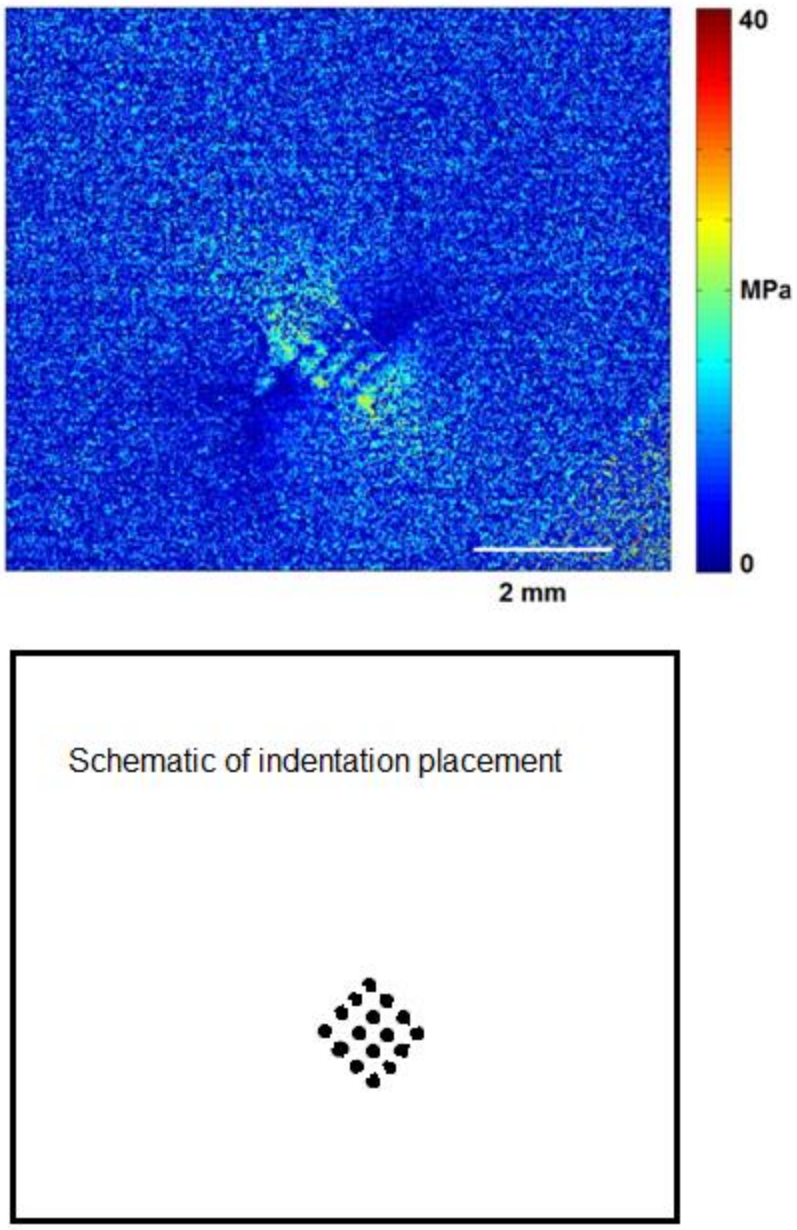

Figure 8-15: Schematic diagram and residual stress field τ_{max} surrounding an indentation array of 0.65 mm spacing.

Inspection of Figure 8-14 and Figure 8-15 also reveals that the array of indentations begins to behave as a single feature, with a secondary stress field surrounding the entire array. This stress field extends a considerable distance into the

surrounding wafer area, and the size and magnitude of the stresses generated by the array are such that the mechanical strength of the wafer is now critically compromised. This was illustrated by the high degree of difficulty in keeping samples unbroken after placement of the arrays.

A binary plot of white "high stress" and black "low stress" points was created for each array. These plots are presented in Figures 8-16 through 8-18, and illustrate the cumulative effect of the indentations as their proximity increases. A "high stress" point is defined as any point where the measured residual stress level is at least 10 MPa higher than the average residual stress of the unaffected wafer.

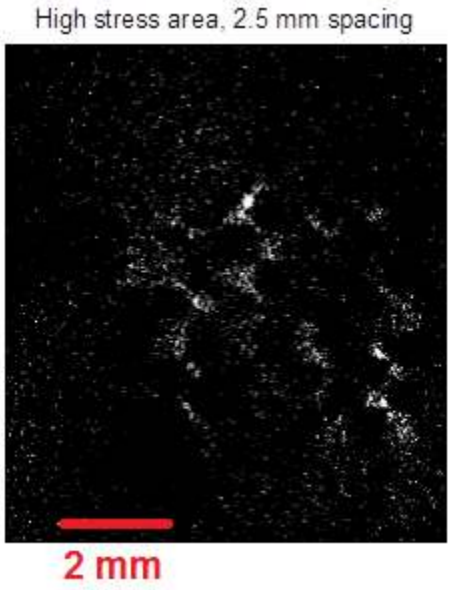

Figure 8-16: Binary high/low stress plot, Vickers indentation array, 2.5 mm spacing.

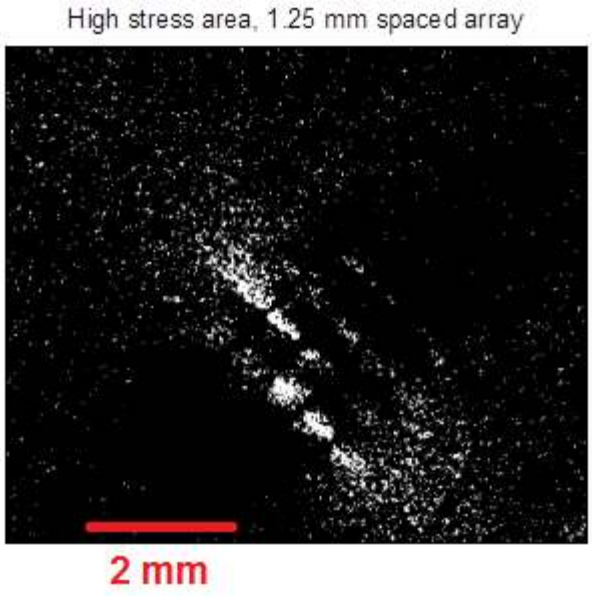

Figure 8-17: Binary high/low stress plot, Vickers indentation array, 1.25 mm spacing.

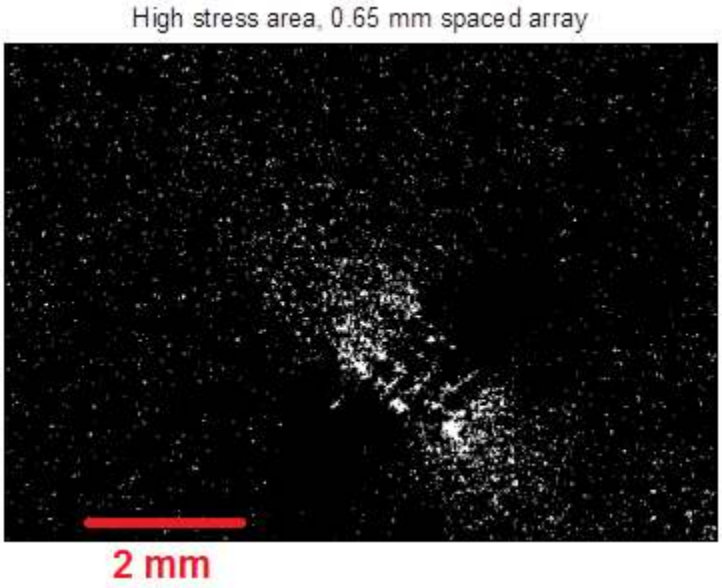

Figure 8-18: Binary high/low stress plot, Vickers indentation array, 0.65 mm spacing.

Examination of the stress field sizes and magnitudes reveals effects of increasing proximity between indentations. The size of the stress field created outside of the array

can be measured using the same method as a single indentation. A circle centered in the middle of the array is drawn around the entire affected area, and its diameter is measured. Each pixel is again equal to an 18 x 18 μm square of the wafer. Table 8-2 summarizes the results.

Table 8-2: Effects of indentation proximity.

Spacing	Array area (mm^2)	Stressed area (mm^2)	Stressed area outside array (mm^2)	Average τ_{max} in stressed area outside array (MPa)
2.5 mm	56.25	68.81	12.56	5.6
1.25 mm	14.06	47.05	32.99	9.2
0.65 mm	3.80	36.75	32.95	11.0

Table 8-2 shows that as proximity increases, a larger amount of wafer area outside of the indentation array is affected by the indentations, and the stress levels in these "affected areas" are higher than those found in less closely spaced arrays. Figure 8-19 presents the data regarding the size of the affected area, while Figure 8-20 addresses the magnitude of the residual stresses.

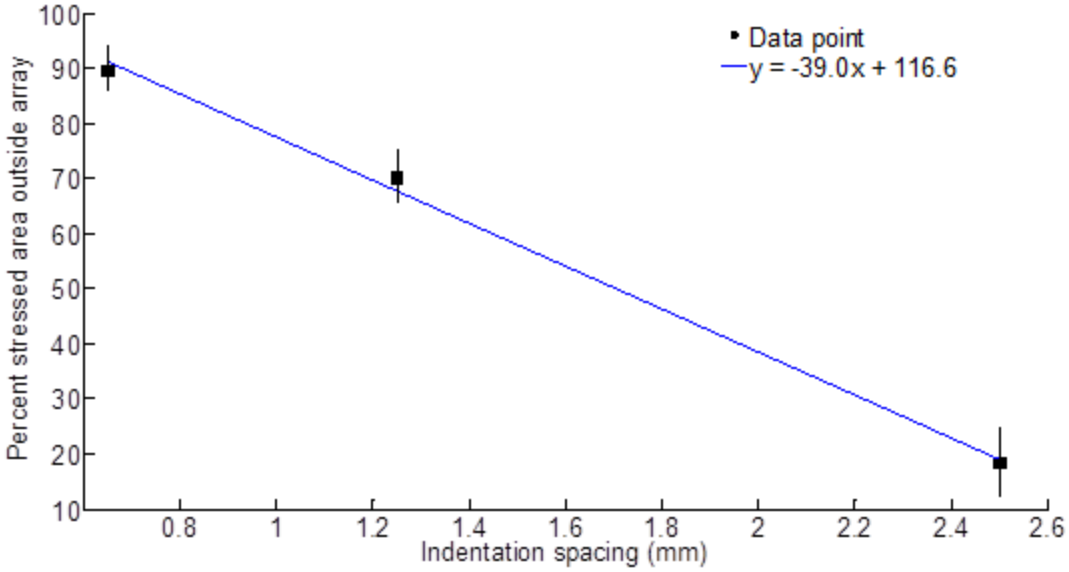

Figure 8-19: Percent of stressed area outside array vs. indentation spacing (mm)

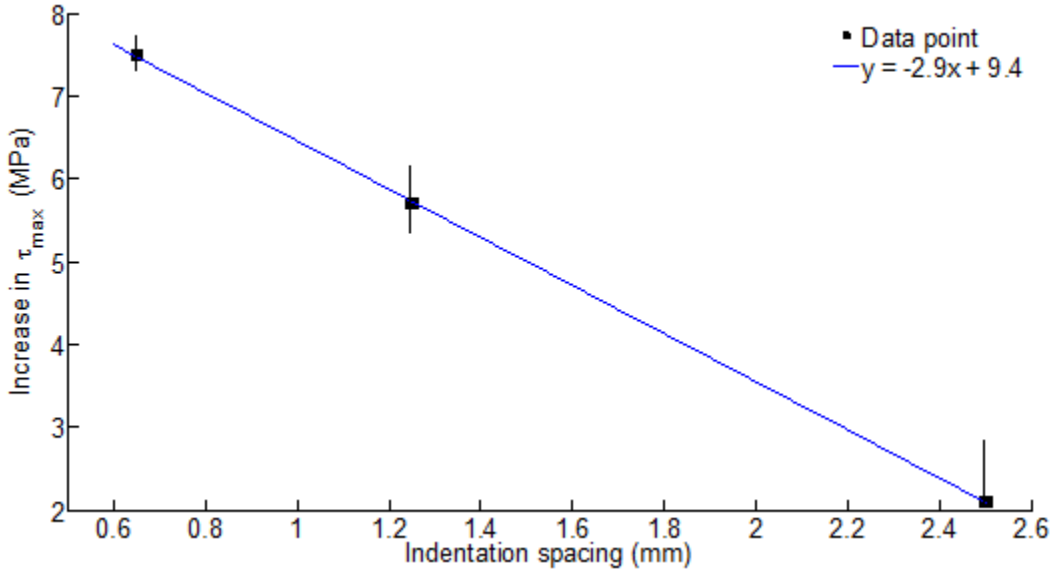

Figure 8-20: Increase in residual stress (MPa) vs. indentation spacing (mm).

The trend in Figure 8-19 is unreliable at spacing under 0.3 mm. Over 100% of the stressed area cannot exist outside of the array. However, the R^2 value for the lines in the

previous two figures is higher than 0.99, suggesting an extremely accurate fit. It must be assumed that some asymptotic behavior occurs as the spacing between stress concentrations becomes extremely small. There is a physical limit to the proximity of stress concentrations such as Vickers indentations. Beyond this limit the wafer will fracture or the stress concentrations will merge into one stress concentration of higher magnitude.

8.4: Grain boundaries and Vickers indentations

The grain boundaries of cast multicrystalline silicon wafers contain noticeably higher stresses than the grain interiors. A typical τ_{max} stress map of a cast multicrystalline wafer is displayed below in Figure 8-21.

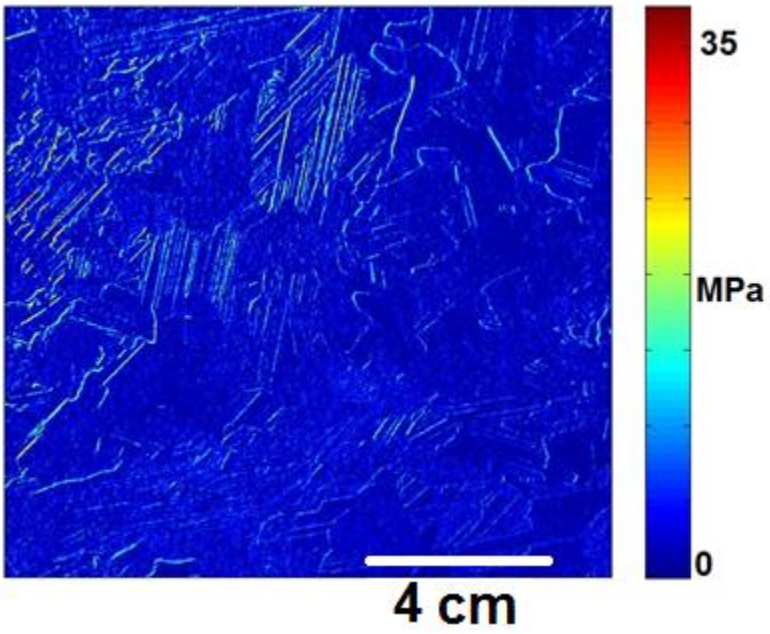

Figure 8-21: τ_{max} residual stress map of mc-Si wafer.

Residual stresses in grain interiors rarely rise above 5 MPa. However, Figure 8-21 shows numerous grain boundaries with residual stress levels of 30 MPa or more. A magnified view of several high-stress grain boundaries is presented below in Figure 8-22.

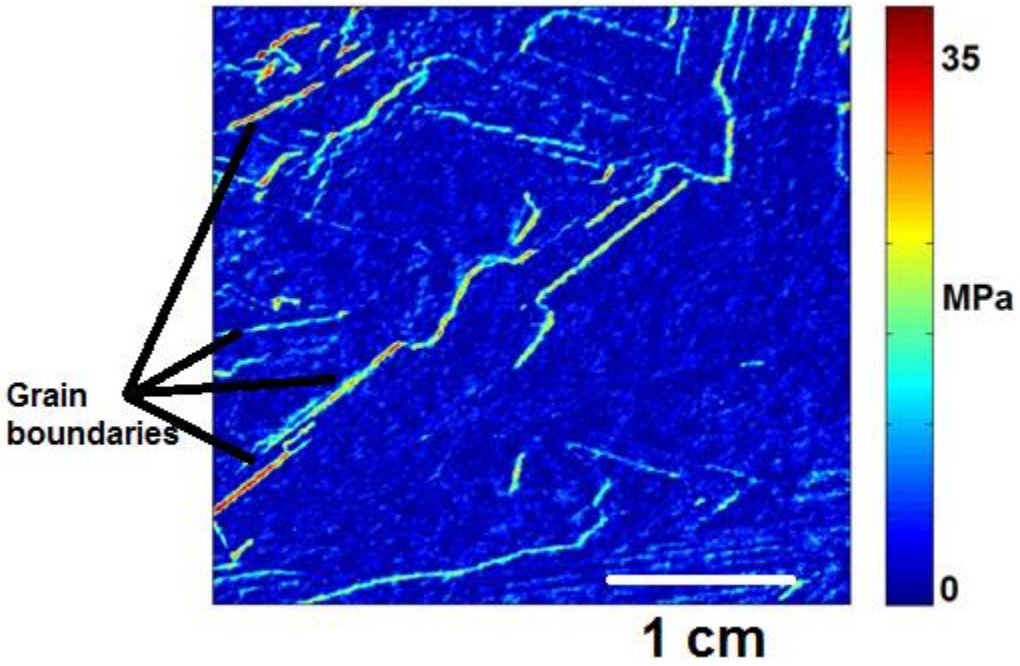

Figure 8-22: τ_{max} stress map of several grain boundaries in mc-Si wafer.

Multicrystalline beams were placed in four-point bending to demonstrate that the stresses detected at grain boundaries were not optical artifacts created by the system. Figure 8-23 shows the results from one of these beams.

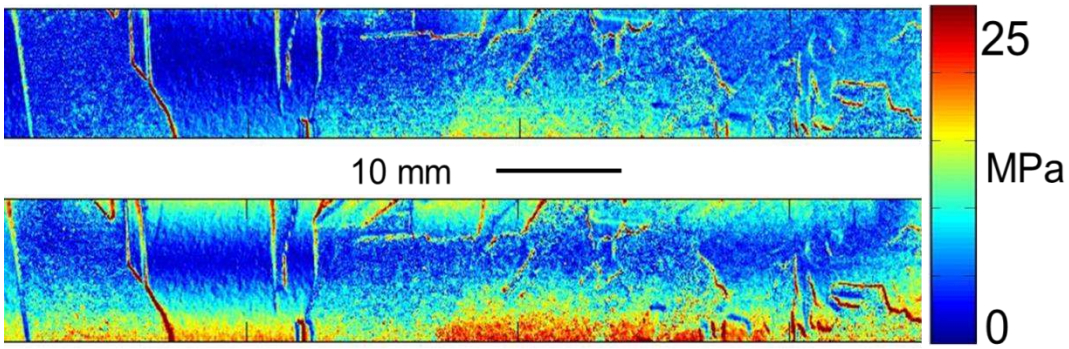

Figure 8-23: τ_{max} stress maps of unloaded (top) and loaded (bottom) multicrystalline silicon beams.

While the grain boundary stresses in Figure 8-23 are frequently higher than 25 MPa, the upper limit of the graph was chosen to clearly demonstrate high-stress grain boundaries. Figure 8-23 shows that stresses at grain boundaries increase in magnitude and affect a larger amount of wafer area. This behavior is in line with what would be expected of a residual stress subjected to an additional external load. It is thus reasonable to conclude that the stresses found by the NIR polariscope at grain boundaries are physical stresses and are not optical artifacts.

With this in mind, interaction between these grain boundary stresses and other stress sources becomes an important factor to consider in the manufacturing process. Defects or cracks which occur near a grain boundary may behave differently than those elsewhere in the wafer. Differences in the wafering process for single crystal and multicrystalline wafers may arise due to the presence of grain boundaries. To quantify the behavior of stress concentrations near grain boundaries, Vickers indentations were created in close proximity to a number of grain boundaries in several different cast multicrystalline wafers. The stresses in the grain boundaries were measured before and after indentation placement. Figure 8-24 is an optical micrograph of a polished and

etched multicrystalline silicon surface and of one grain boundary before and after indentation placement.

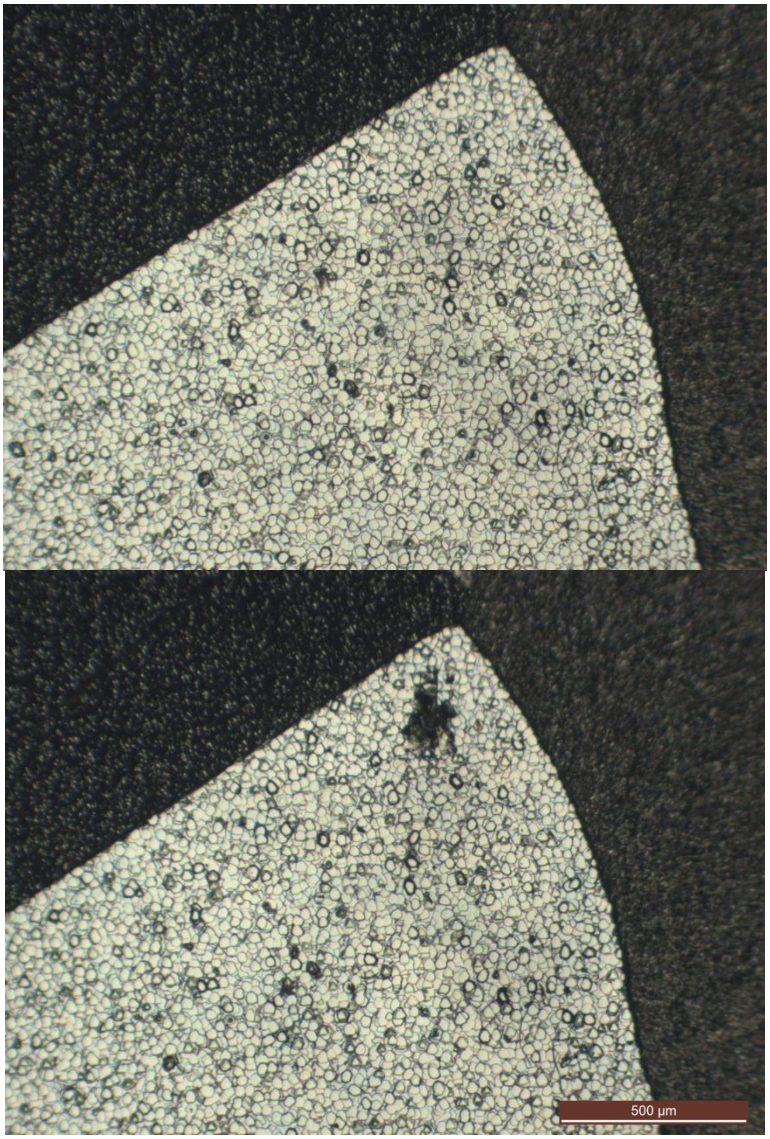

Figure 8-24: Optical micrographs of grain boundaries before and after nearby Vickers indentation.

Small indentation arrays were also placed closely to other grain boundaries to examine the effects of multiple indentations. Figure 8-25 displays one of these samples below.

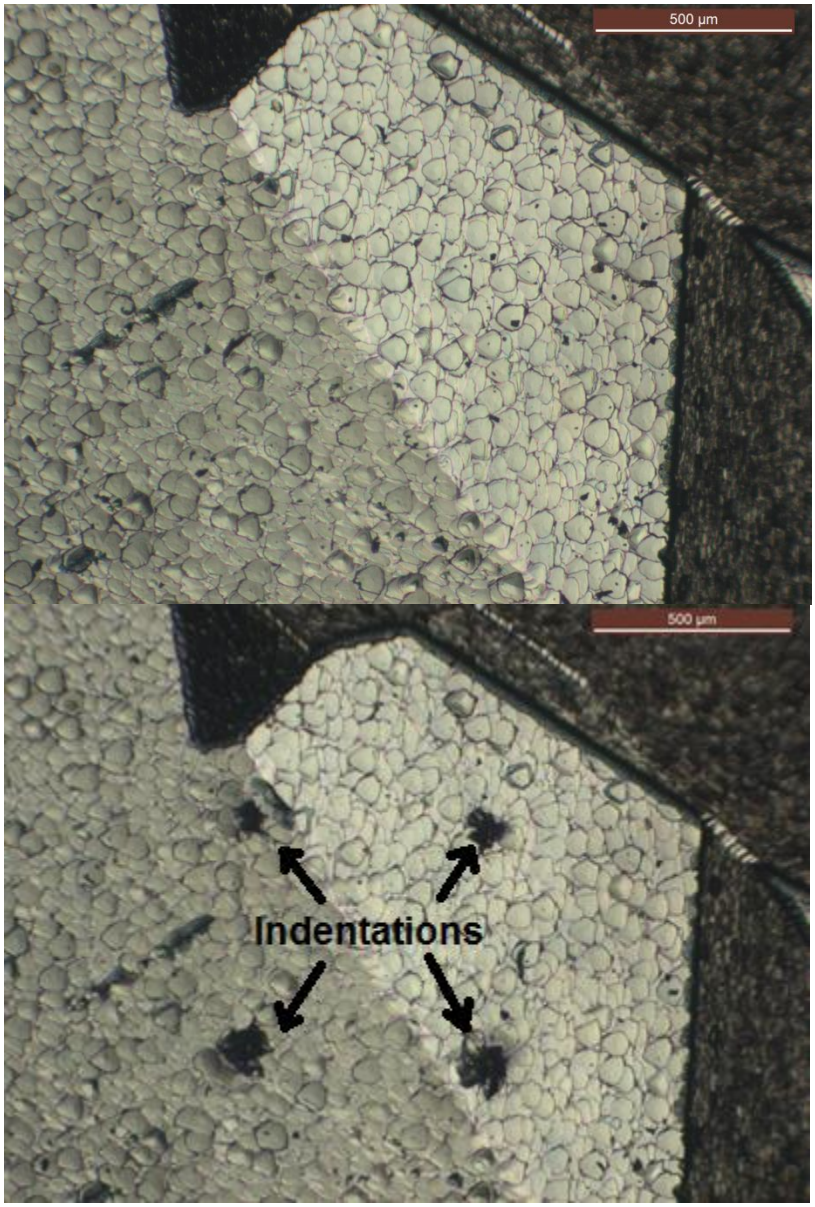

Figure 8-25: Optical micrograph of grain boundary before and after 2x2 Vickers indentation array.

The indentations were always placed within 300 µm of a grain boundary, ensuring that the boundary would be within the radius of even the smallest affected zone documented in Figure 8-10.

Stresses at and near the grain boundaries were evaluated with the NIR polariscope before and after the placing of Vickers indentations. Figures 8-26 and 8-27 show before and after stress analysis of a grain containing four indentations.

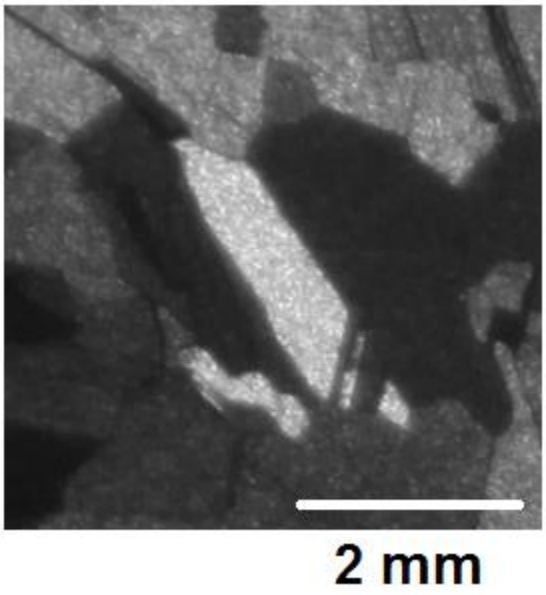

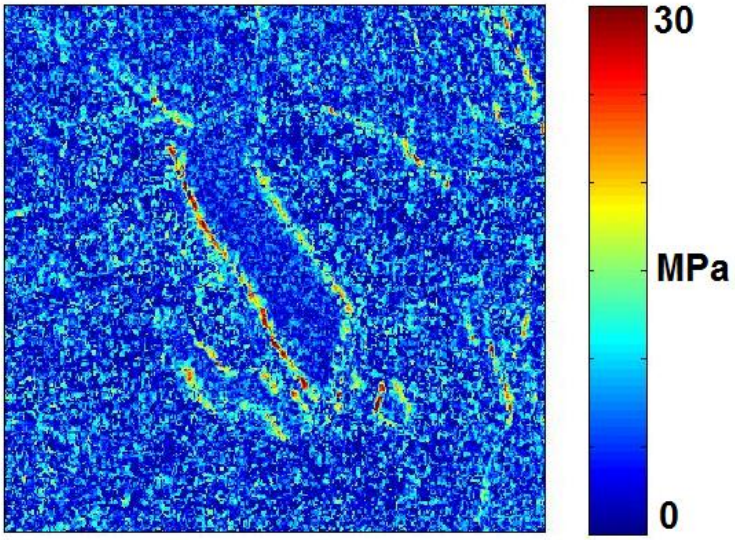

Figure 8-26: NIR transmission image and τ_{max} stress map of grain boundaries prior to Vickers indentation placement.

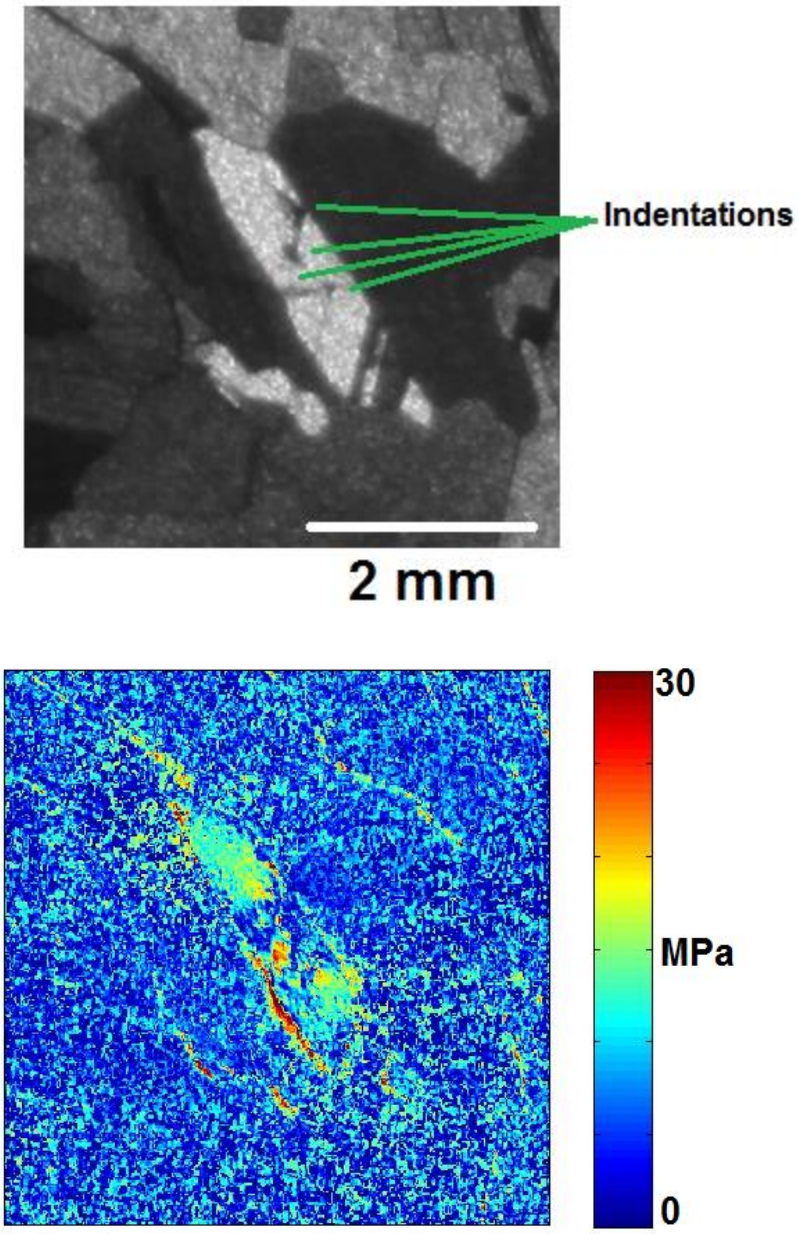

Figure 8-27: NIR transmission image and τ_{max} stress map of grain boundaries after Vickers indentation placement.

Several conclusions are supported by Figures 8-26 and 8-27. The stresses in the grain have significantly increased from residual stress levels (~4 MPa). The grain in which the indentations were placed now contains stresses in the realm of 15 MPa. However, there are no consistent or well-defined stress fields around each indentation

such as the ones seen in Figure 8-9. Rather, the stresses caused by the indentations have now spread out evenly over the entire grain. Second, these stresses are arrested by the grain boundaries and do not extend beyond the grain boundaries into neighboring grains. This is confirmed through examination of the isoclinic angle map of the same area, shown below in Figure 8-28.

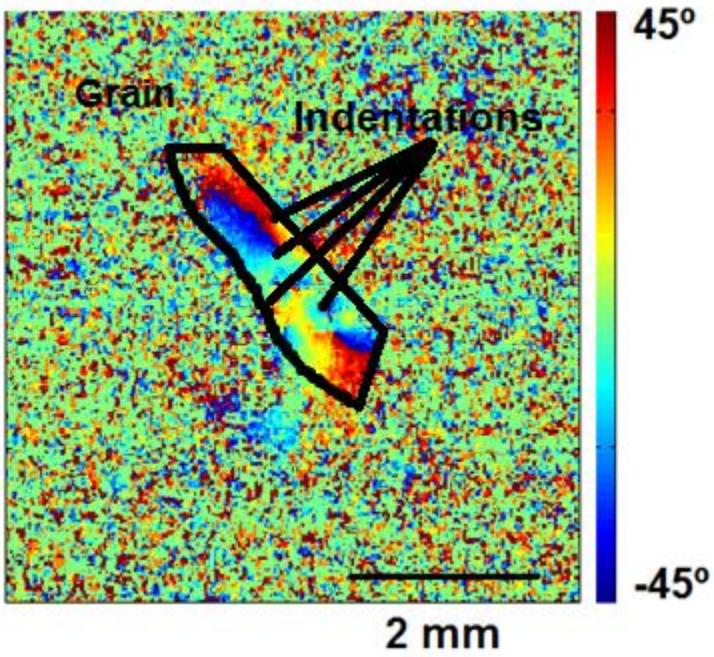

Figure 8-28: Isoclinic map of grain after placement of Vickers indentations.

The isoclinic parameter is noisy at regions outside of the grain in question, behavior which is in line with low stress levels. The grain containing Vickers indentations has a very well-defined isoclinic field indicative of high stress levels throughout the region. This well-defined region ends at the grain boundaries, supporting the statement that the high stresses in the grain do not extend past the grain boundaries.

Finally, the grain boundary stresses have been altered. This is most clearly observed along the left side of the grain. Before indentations, the τ_{max} stresses in the

grain boundary range from 15-30 MPa and the stressed area at the grain boundary is roughly 100 μm wide. After indentation placement, the grain boundary stresses in the lower left corner have risen to 25-50 MPa, and the stressed area has increased in size to 200 μm wide. The stresses in the upper left corner have dropped into the 5-20 MPa range, and in several areas are indistinguishable from the rest of the wafer. Figure 8-29 shows the maximum shear stress profile across the grain boundary before and after indentation placement. The black line in the stress map indicates the profile path.

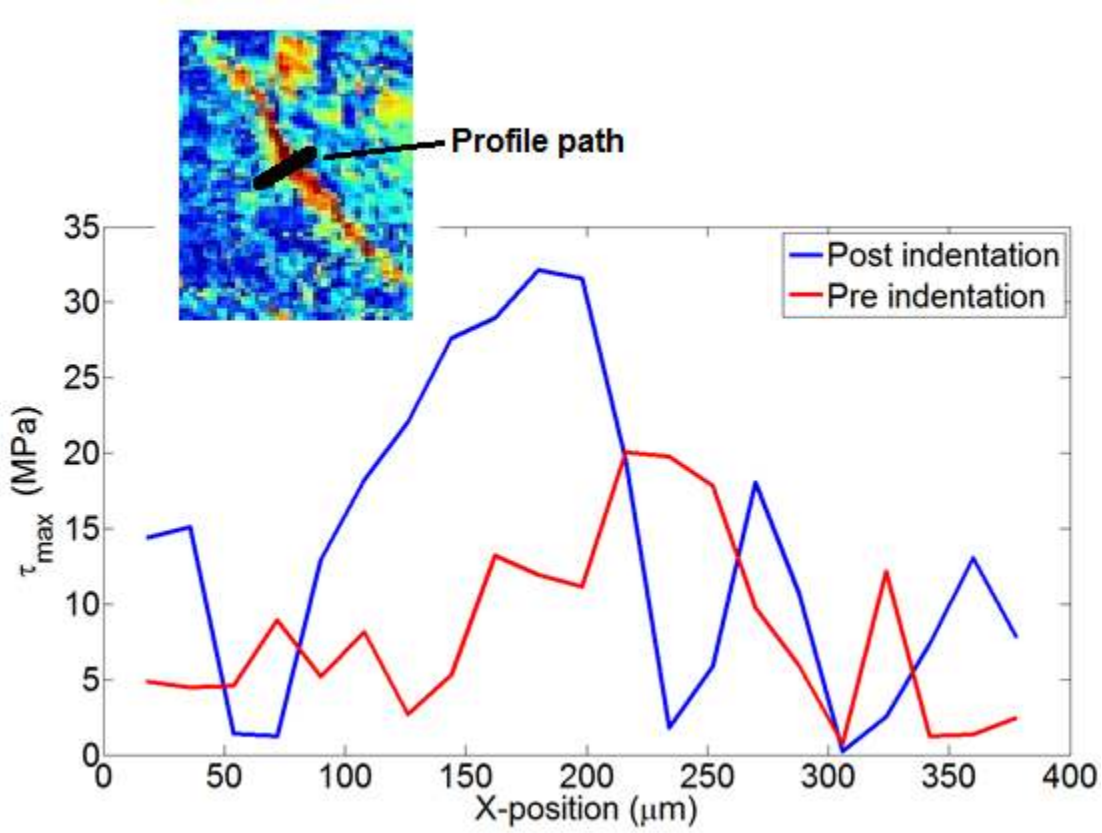

Figure 8-29: τ_{max} (MPa) vs. x-position (μm) across a grain boundary before and after placement of Vickers indentations

This variation in behavior can be explained by the definition of τ_{max}, which is the absolute value of the difference between the two principal normal stresses. The τ_{max}

stresses in the upper left corner of the grain boundary have decreased by the same quantity that the stresses in the lower left corner have increased. This indicates a case which causes the quantity $|\sigma_1 - \sigma_2|$ to increase in one area but decrease in another. Two possibilities exist: One, the stresses at the grain boundary change from tensile to compressive along the boundary length. Two, the change in positioning of the indentations with respect to the grain boundary brings the values of σ_1 and σ_2 closer together in some regions but further apart in others.

Based on this behavior, the effects of indentations on grain boundary stresses were only characterized in terms of absolute value. 32 grain boundaries were examined in 11 cast multicrystalline wafers. The highest and lowest τ_{max} stresses were measured in each grain boundary prior to indentation. Figures 8-30 shows the magnitude of the stress changes.

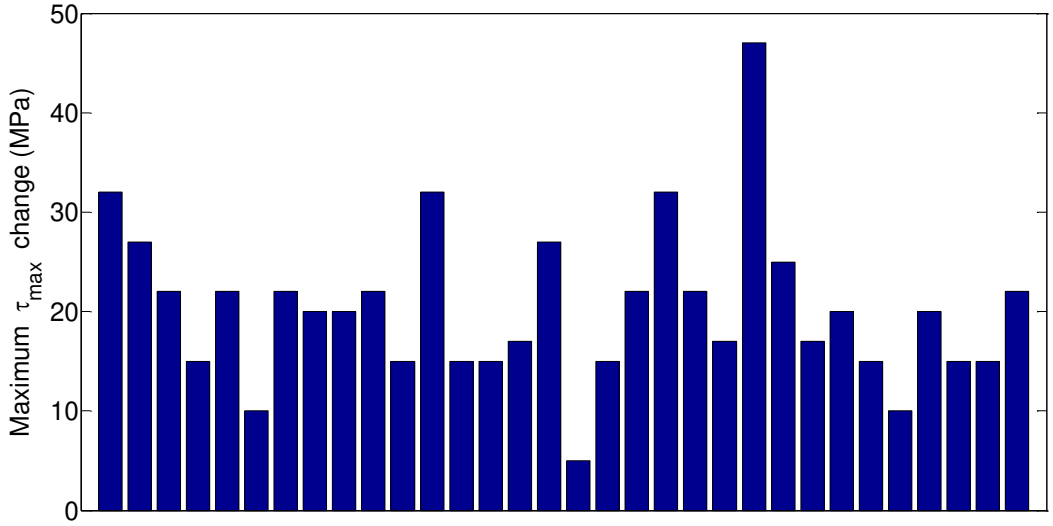

Figure 8-30: Change in highest measured τ_{max} residual stress levels in 32 grain boundaries after indentation.

Figure 8-30 is evidence of significant changes in grain boundary stresses caused by Vickers indentations. A 2 N Vickers indentation results in a grain boundary stress change of at least 10 MPa in all but two cases. Table 8-3 summarizes the data.

Table 8-3: Summary of grain boundary stress changes after Vickers indentation

	Mean	Standard Deviation
Magnitude of highest τ_{max} change (MPa)	20.4	8.0
Magnitude of lowest τ_{max} change (MPa)	14.6	5.5

There is no correlation between physical parameters such as number of indentations placed or grain boundary proximity to an indentation. The grain boundaries farthest from the indentations and the grain boundaries closest to the indentations were often equally affected. Figure 8-31 shows the NIR transmission image and stress map of multiple grain boundaries affected by a single indentation.

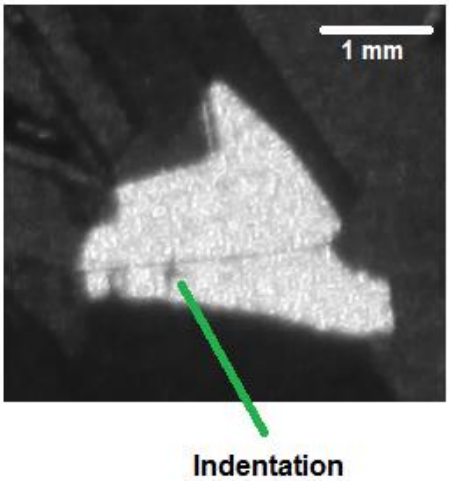

(a)

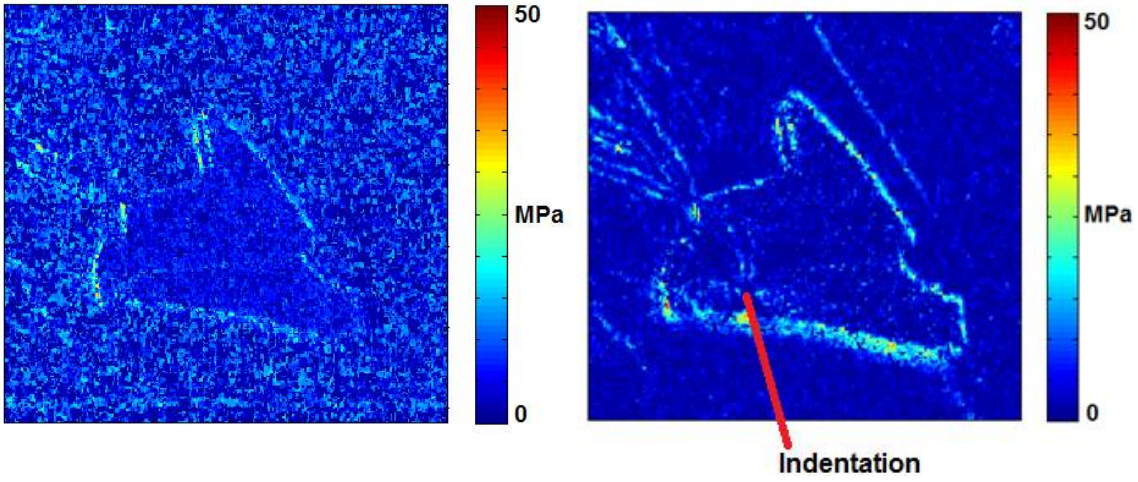

(b)

Figure 8-31: (a) NIR transmission image of a grain after indentation and (b) τ_{max} stresses at grain boundaries before and after placement of a single indentation.

The top right grain boundary undergoes an increase in stress nearly identical to the bottom grain boundary. This occurs even though the distance between the indentation and the two grain boundaries differs by an order of magnitude. Furthermore, the grains in Figure 8-27 and Figure 8-31 are of similar size. The effects on the grain boundary

stresses are quite similar despite one grain containing four Vickers indentations and the other grain containing only one. The number of indentations placed next to grain boundaries in the samples ranged from a single indentation to six indentations in a 2 x 3 array. No discernible relationship was observed correlating the distance between the grain boundary and indentation with stress changes in the grain boundary.

The τ_{max} patterns surrounding the indentations such as the ones in Figure 8-9 are not present after indentation in a grain. However, the binary isoclinic map of the grain reveals well-defined isoclinics, indicating the presence of high normal stresses. Figure 8-32 presents the isoclinic data of the grain in Figure 8-31.

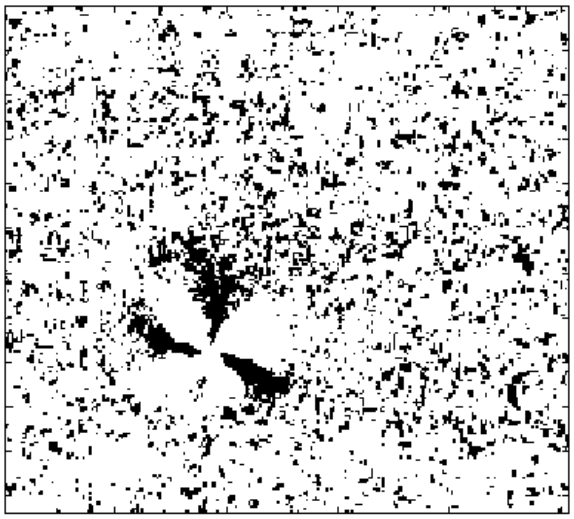

Figure 8-32: Binary plot of isoclinic behavior around single Vickers indentation.

The isoclinic information indicates that while the shear stresses in the grain are lower than expected, normal stresses are elevated. Furthermore, shear stresses in the grain boundaries have increased by the magnitude of the shear stress field surrounding individual indentations in the CZ wafer.

8.5 Conclusions

Vickers indentations in CZ silicon were found to produce residual stress fields surrounding the indentation. Multiple 2 N indentations resulted in residual stress fields 1.2 mm in diameter with a τ_{max} value of 22 MPa. Placing indentations in closely spaced arrays produces a secondary residual stress field around the array. The diameter and magnitude of this secondary residual stress field is related to the spacing between indentations. Grain boundaries in cast multicrystalline wafers were found to contain higher maximum shear stresses than grain interiors. Vickers indentations placed near grain boundaries altered the grain boundary stresses by 15-20 MPa. The stress fields created by the Vickers indentations were also arrested by the grain boundary. This effect is not related to the number of indentations placed or the grain boundary's proximity to the indentations.

CHAPTER 9
THEORETICAL ANALYSIS OF GRAIN BOUNDARIES AND INDENTATIONS

9.1: Grain boundary energy and stresses

Grain boundaries in multicrystalline materials are planar defects and extremely important to the mechanical properties of a material [53]. The transition regions between two grains of different crystallographic orientations can be represented as dislocation arrangements. If the misorientation between two grains is relatively small, the boundary is identified as a low-angle boundary and can be treated as a relatively simple configuration of dislocations. High-angle grain boundaries are considerably more complex and require detailed knowledge of particular atomic characteristics.

The grain boundaries considered in this research will be treated as low-angle grain boundaries with a misorientation angle θ of 10º, which is the highest misorientation angle at which low angle grain boundary theory still applies [54]. Each grain boundary is also assumed to be an arrangement of edge dislocations between two grains as illustrated in Figure 9-1.

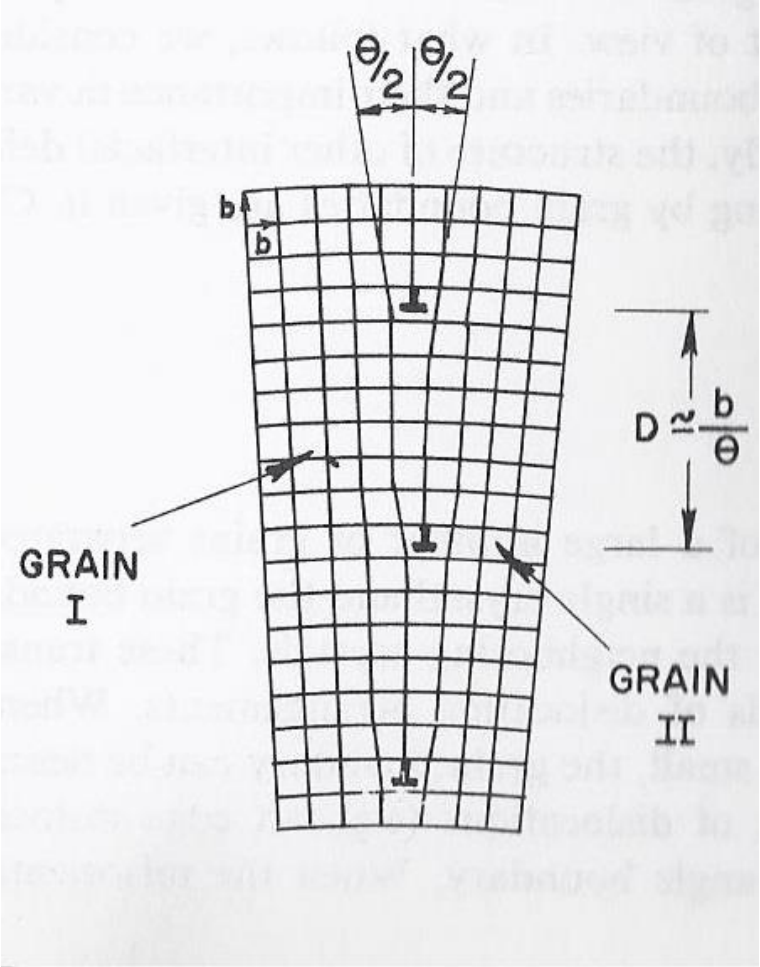

Figure 9-1: Low-angle tilt boundary. [54]

The Read and Shockley equation can be used to find the energy in a grain boundary such as the one in Figure 9-1 [53]:

$$E = E_0\theta[A - \ln\theta] \tag{29}$$

Where E_0 is defined as

$$E_0 = \frac{Gb}{4\pi(1-\nu)} \tag{30}$$

and A is an integration constant dependent on the unknown energy of atomic misfit. The stress components around an edge dislocation in an isotropic material can be defined as:

$$\sigma_x = -\frac{\tau_0 b}{r}\sin\theta\,(2+\cos 2\theta) \tag{31}$$

$$\sigma_y = \frac{\tau_0 b}{r}\sin\theta\cos 2\theta \tag{32}$$

$$\tau_{xy} = \frac{\tau_0 b}{r}\cos\theta\cos 2\theta \tag{33}$$

Where τ_0 is defined similarly to E_0 as

$$\tau_0 = \frac{G}{2\pi(1-\nu)} \tag{34}$$

For anisotropic materials such as silicon, the elastic constants C_{ij} and the orientations of the dislocation and Burgers vector must be taken into account. The shear stress τ is defined by the equation

$$\tau = \tau_0 \frac{b}{r} \tag{35}$$

where b is the lattice constant indicated in Figure 9-1 (0.543 nm for silicon) and r is the distance away from the dislocation. As r approaches infinity in all of the above cases, τ approaches zero. The value τ_0 now depends on the elastic constants. Eshelby, Read, and Shockley have solved several common cases, including a dislocation in an <001> direction with a Burgers vector in a (100) plane [55].

$$\tau_0 = \frac{1}{2\pi}\left[C_{44}\cos^2\alpha + \sin^2\alpha(C_{11}+C_{12})\sqrt{\frac{C_{44}(C_{11}-C_{12})}{C_{11}(C_{11}+C_{12}+2C_{44})}}\right] \tag{36}$$

The term α in Equation (35) represents the angle between the Burgers vector and the dislocation. Possible values of α are constrained by the crystal structure of the material in question. FCC structures such as silicon are limited to $\alpha = \pi/2$ or $\alpha = \pi/4$. A value of $\pi/2$ was chosen to model the scenario with the highest possible stresses. The

material constants for silicon can be found in literature [56] and are presented below in Table 9-1.

Table 9-1: Material constants C_{ij} for (100) silicon.

C_{ij}	C_{11}	C_{12}	C_{44}
C_{ij} (10^9 Pa)	165.6	63.9	79.5

Calculation of the theoretical shear stress present at a silicon grain boundary is straightforward from this point. Using the values in Table 9-1 in Equation (35) with an α value of $\pi/2$ results in an evaluation of τ_0 which can then be used in Equation (34) to plot the theoretical shear stress τ as a function of distance r away from the center of the grain boundary. The results from this analysis are shown in Figure 9-2.

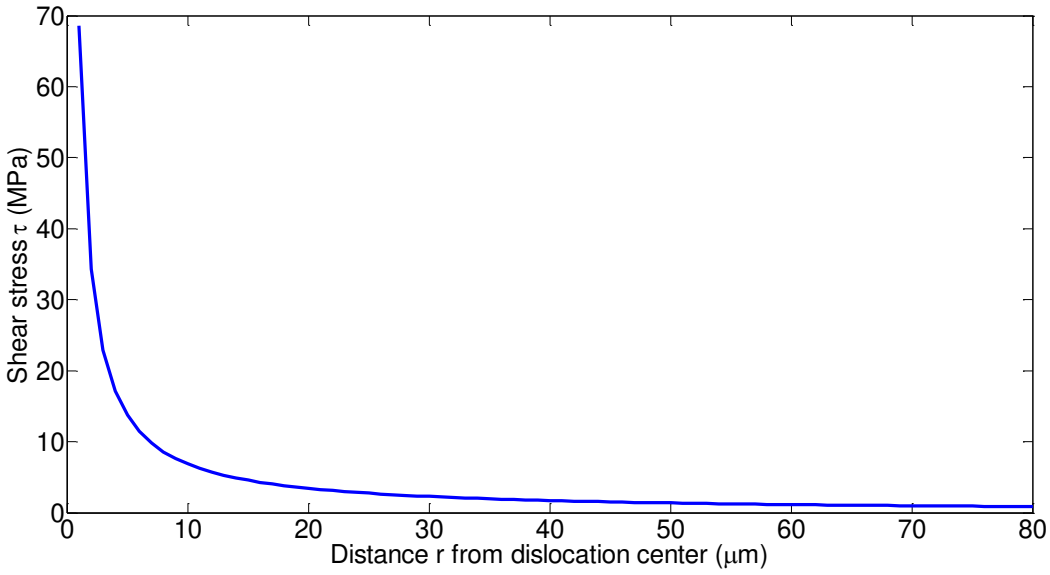

Figure 9-2: Dislocation stresses (MPa) vs r (μm).

Figure 9-2 shows that grain boundary shear stresses of at least 30-40 MPa should be expected for silicon. The higher stresses which should be present within 5 μm of the grain boundary center are below the spatial resolution of the NIR polariscope, which is 18 μm as currently constructed. Thus, the highest stresses in Figure 9-2 would not appear in photoelastic analysis of the grain boundaries. The higher stresses within 10 μm of the boundary on either side would appear as an averaged value over the width of a pixel.

Examination of Figure 8-26 shows that the shear stresses measured with the NIR polariscope at the grain boundaries are mostly in the 25-35 MPa range. This is consistent with the spatial averaging occurring below the minimum resolution of the system. The polariscope does detect stresses greater than predicted up to a radius of 40 μm. A stress multiplying phenomena has already been observed with larger point stresses as seen in Figure 8-19. The same behavior of clustered dislocation stresses at a grain boundary would explain the larger radius of high-stress area visible in Figure 8-26. Furthermore, the assumptions made about the direction of the dislocations and the crystallographic orientations involved will not hold true for every grain boundary. The experimental and theoretical results are within reasonable agreement.

9.2 Contact analysis of Vickers indentations

The stresses around two non-conforming surfaces such as a Vickers indenter and a silicon wafer may be estimated through Hertzian contact analysis. Figure 9-3 shows the general behavior on which this analysis is founded.

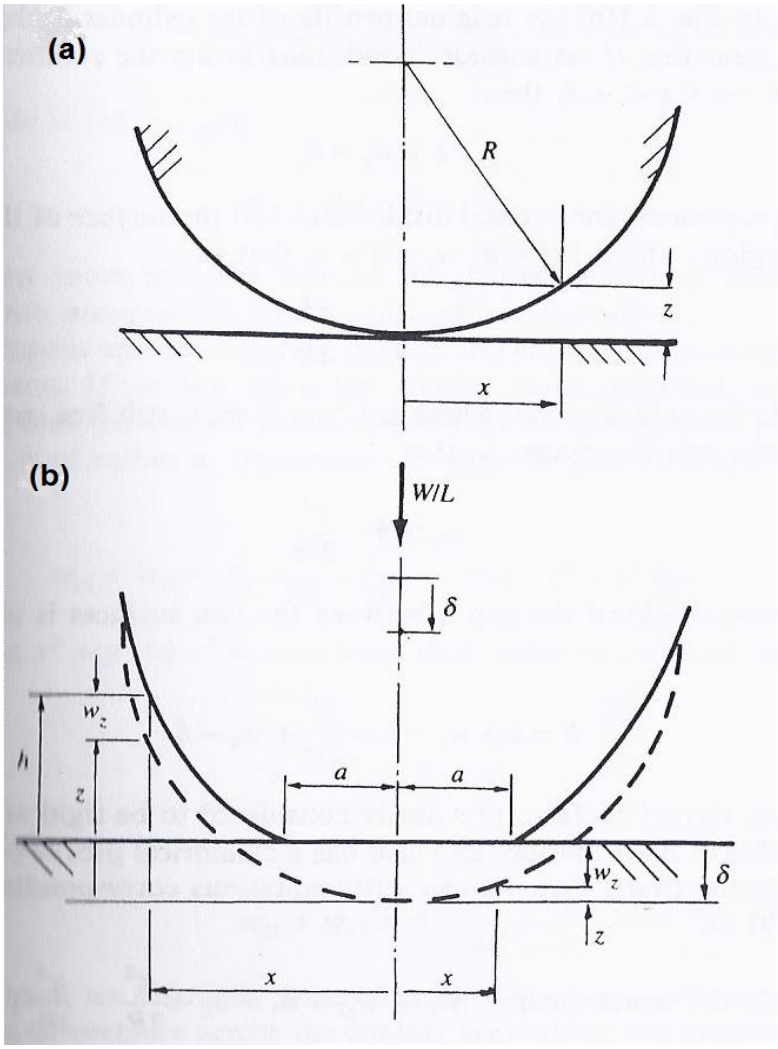

Figure 9-3: Contact geometry between (a) an unloaded long deformable cylinder and a rigid plane surface, (b) carrying a load per unit length of W/L. [57]

Figure 9-4 illustrates the same principles extended to a pair of spheres. This situation may be approximated if the Vickers indenter is modeled as a body with a very small radius and the silicon wafer is represented as a plate with infinite radius.

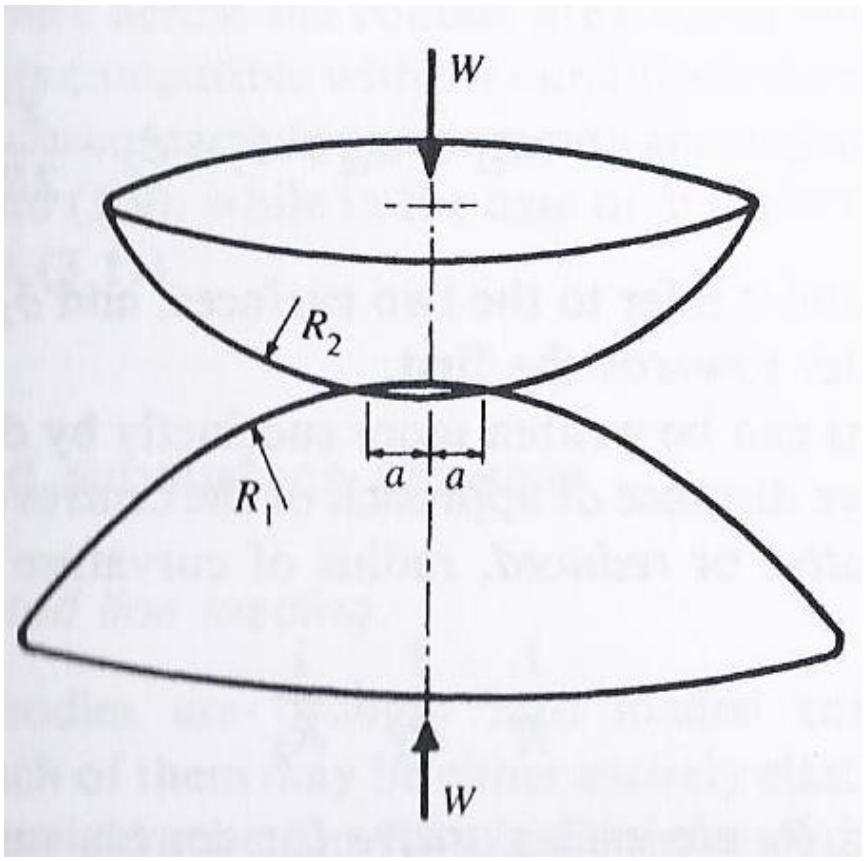

Figure 9-4: Contact between two deformable spheres. [58]

Assuming cylindrical coordinates, the circumferential stress $\underline{\sigma_\theta}$ around the point load is everywhere compressive, while the radial stress σ_r is compressive over nearly the entirety of the contact patch and tensile everywhere outside of it (that is, when $r > a$). The area outside of the contact patch is of main interest for this research. The components of stress σ_θ and σ_r in this area may be estimated by the following:

$$\sigma_r = -\sigma_\theta = \frac{(1-2\nu)a^2}{3r^2} p_0 \tag{37}$$

Here, a^2 is the radius of the contact area and can be found with

$$a^3 = \frac{3WR}{4E^*} \tag{38}$$

Where W is the applied load, R is the reduced radius of contact and E^* is the contact modulus, which are defined as

$$\frac{1}{R} = \frac{1}{R_1} + \frac{1}{R_2} \tag{39}$$

$$\frac{1}{E^*} = \frac{1-\nu_1^2}{E_1} + \frac{1-\nu_2^2}{E_2} \tag{40}$$

The approximate tip radius of a diamond pyramid indenter is around 100 nm, which increases with wear and use [58]. A tip radius of R_1 = 200 nm was used for calculations, since the diamond in the Buehler microhardness tester is several years old. The radius R_2 of the silicon wafer is infinite, thus $R = R_1 = 200$ nm. Values for Poisson's ratio and the Young's modulus of silicon [59] and diamond [60] are obtained from literature and are given below in Table 9-2.

Table 9-2: Material properties of diamond and silicon.

Material	Poisson's ratio ν	Young's modulus E (GPa)
Diamond	0.2	1220
Silicon	0.27	160

E^* can be determined from these values, and is evaluated as 152 GPa. Equation (37) can subsequently be used to find a, evaluated as 1.25 μm. The pressure term p_0 is found using

$$p_0 = \frac{3W}{2\pi a^2} \tag{41}$$

and is evaluated as 6.1×10^{11} Pa. A plot of σ_r against radius r can then be constructed for the area outside the contact patch. This data is shown in Figure 9-5. Data was not generated for $r < 20$ μm, which would be below the spatial resolution of the polariscope. The maximum shear stress τ_{max} will very closely approximate σ_r due to the relationship $\sigma_r = -\sigma_\theta$ in Equation (36).

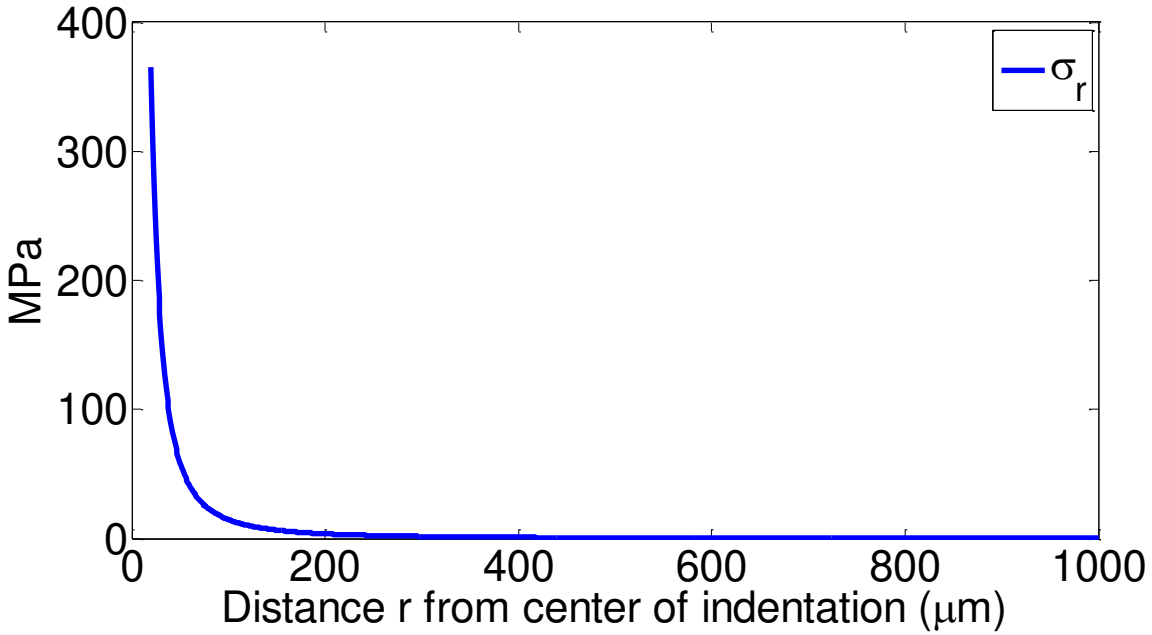

Figure 9-5: Radial stress σ_r (MPa) as a function of distance r (μm) from indenter.

Figure 9-5 shows stress values of around 350 MPa for σ_r during loading. Residual stresses of 30 MPa are thus reasonable to expect. However, the predicted stress field falls under 10 MPa at a distance of only 150 μm from the indentation center, which is a significant deviation from the results measured by the polariscope. Figure 9-6 compares the Hertzian prediction with the experimental results at $r > 100$ μm.

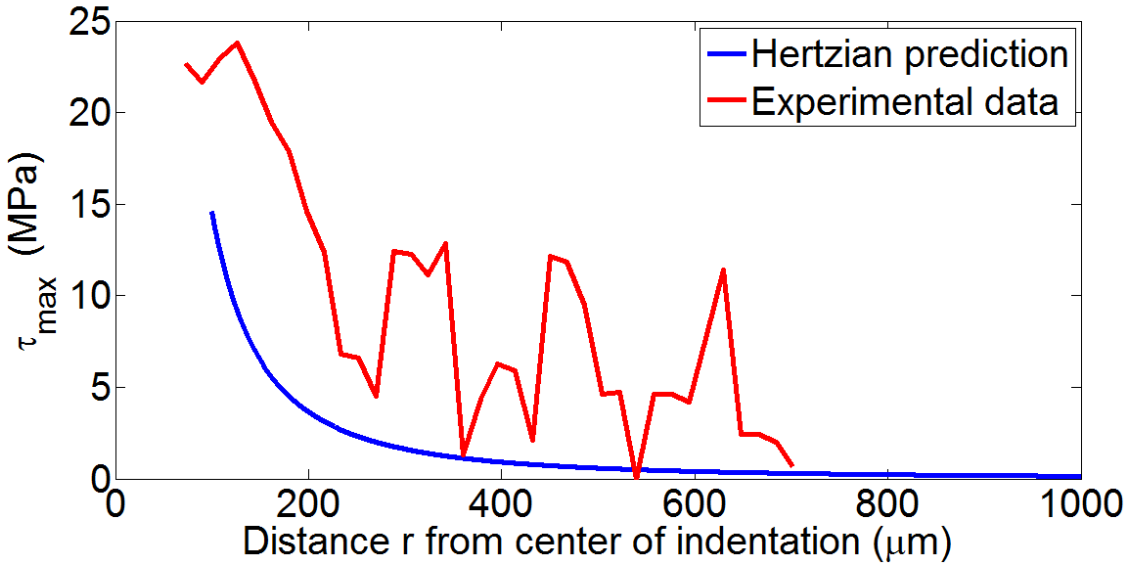

Figure 9-6: τ_{max} (MPa) vs. r (μm) for Hertzian model and experimental results

The experimentally measured stress fields are consistently greater than a millimeter in diameter.

The problem of a point load on an infinite isotropic 3D half space was first solved by Boussinesq in 1885 [61]. Boussinesq's solution takes the general form of a Green's tensor which goes to zero at infinity. In Cartesian coordinates, the solution tensor can be expressed as:

$$G_{ik} = \frac{1}{4\pi\mu}\begin{bmatrix} \frac{b}{r}+\frac{x^2}{r^3}-\frac{ax^2}{r(r+z)^2}-\frac{az}{r(r+z)} & \frac{xz}{r^3}-\frac{axy}{r(r+z)^2} & \frac{xz}{r^3}-\frac{ax}{r(r+z)} \\ \frac{yx}{r^3}-\frac{ayx}{r(r+z)^2} & \frac{b}{r}+\frac{y^2}{r^3}-\frac{ay^2}{r(r+z)^2}-\frac{az}{r(r+z)} & \frac{yz}{r^3}-\frac{ay}{r(r+z)} \\ \frac{zx}{r^3}+\frac{ax}{r(r+z)} & \frac{zy}{r^3}+\frac{ay}{r(r+z)} & \frac{b}{r}+\frac{z^2}{r^3} \end{bmatrix} \quad (42)$$

Where $a = 1-2\nu$, $b = 2(1-\nu)$, and r and z are the radial distance and depth from the point load. Lawn and Swain used the Boussinesq solution to study the behavior of point loads in brittle solids [62]. A diagram of the geometry and coordinate system involved for their investigation is shown below in Figure 9-7.

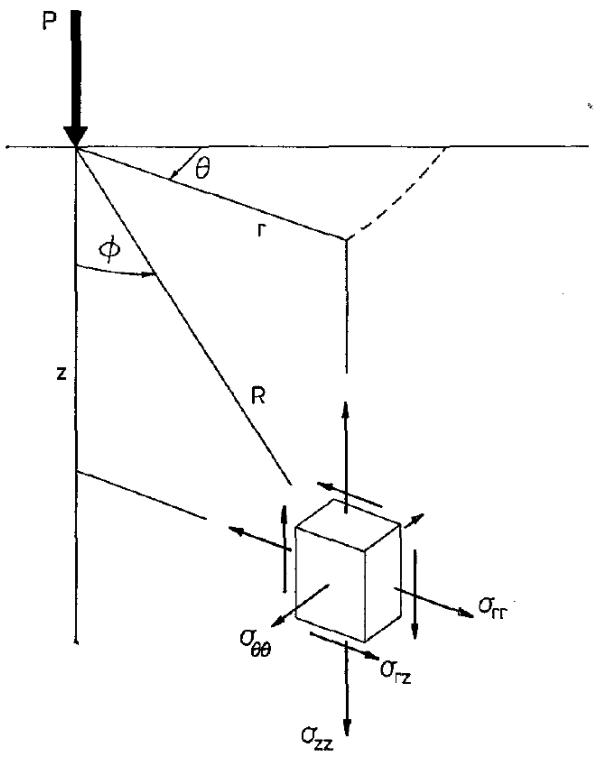

Figure 9-7: Curvilinear coordinate system used for Boussinesq analysis. [62]

Separating the solution matrix into its separate components and converting to curvilinear coordinates results in the following equations for stress evaluation.

$$\sigma_{rr} = \frac{P}{\pi R^2}\left\{\left(\frac{1-2\nu}{4}\right)\sec^2\frac{\phi}{2} - \frac{3}{2}\cos\phi\sin^2\phi\right\} \tag{43}$$

$$\sigma_{\theta\theta} = \frac{P}{\pi R^2}\left\{\left(\frac{1-2\nu}{2}\right)\left(\cos\phi - \frac{1}{2}\sec^2\frac{\phi}{2}\right)\right\} \tag{44}$$

$$\sigma_{zz} = \frac{P}{\pi R^2}\left\{-\frac{3}{2}\cos^3\phi\right\} \tag{45}$$

$$\sigma_{rz} = \frac{P}{\pi R^2}\left\{-\frac{3}{2}\cos^2\phi\sin\phi\right\} \tag{46}$$

$$\sigma_{r\theta} = \sigma_{\theta z} = 0 \tag{47}$$

Tensor transformations yield the directions and magnitudes of the resultant principal stresses. The principal normal stresses σ_{11} and σ_{33} are contained in a symmetry plane whose angle with the sample surface is given by

$$\tan 2\alpha = 2\sigma_{rz}/(\sigma_{zz} - \sigma_{rr}) \tag{48}$$

While the principal normal stress σ_{22} is perpendicular to the symmetry plane. The principal normal stresses can then be determined using these equations:

$$\sigma_{11} = \sigma_{rr}\sin^2\alpha + \sigma_{zz}\cos^2\alpha - 2\sigma_{rz}\sin\alpha\cos\alpha \tag{49}$$

$$\sigma_{22} = \sigma_{\theta\theta} \tag{50}$$

$$\sigma_{33} = \sigma_{rr}\cos^2\alpha + \sigma_{zz}\sin^2\alpha + 2\sigma_{rz}\sin\alpha\cos\alpha \tag{51}$$

The Vickers indentations are assumed to be point loads of 2 N. Surface stresses are found at an angle ϕ of 90º. These surface stresses are plotted in Figure 9-8. Data was not generated for R < 20 μm.

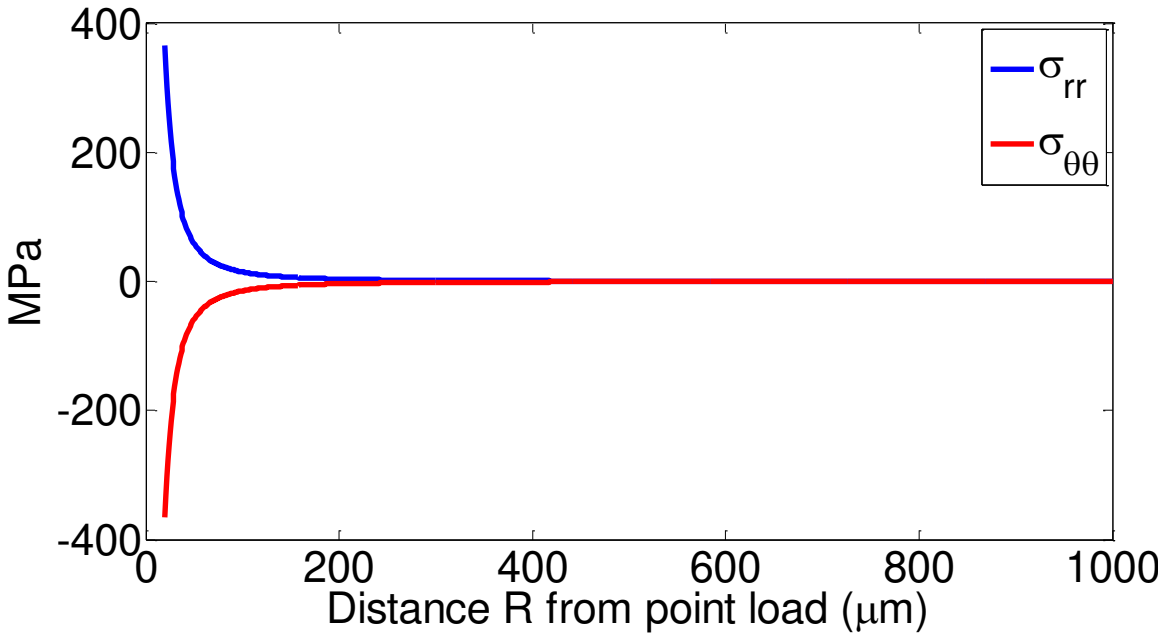

(a)

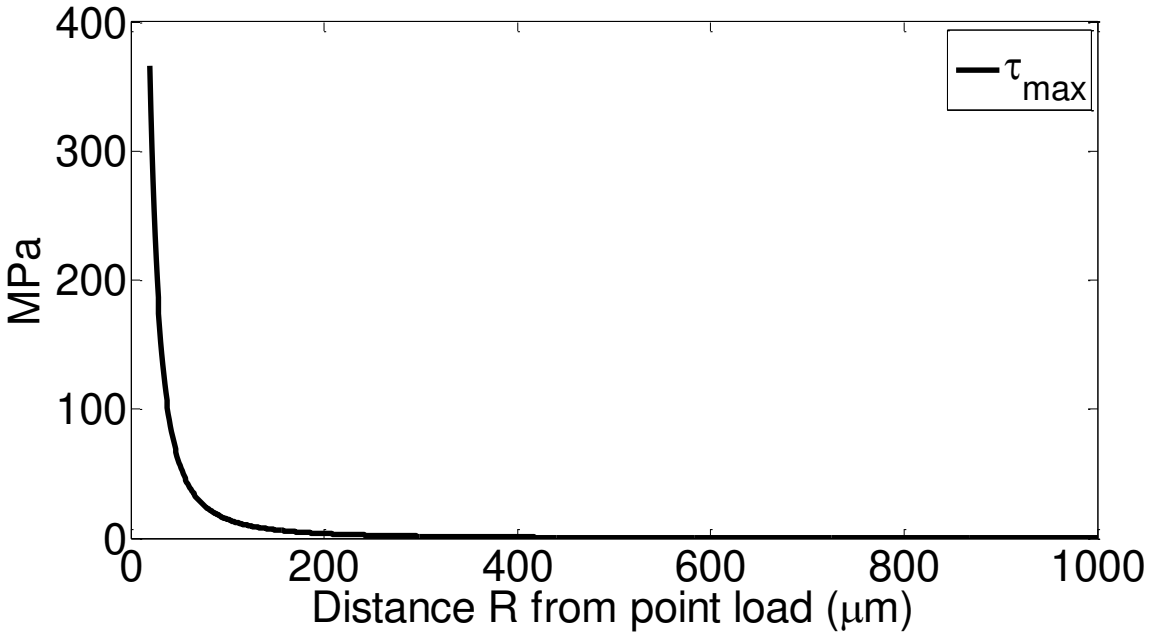

(b)

Figure 9-8: (a) σ_{rr} and $\sigma_{\theta\theta}$, (b) τ_{max} fields (MPa) vs. R (μm) predicted by the Boussinesq solution (ϕ = 90º).

Figures 9-5 and 9-8 show similar predictions from Hertzian theory and the Boussinesq solution. Stresses very near the point of contact reach levels of almost 400 MPa. However, the stress field decreases sharply as the distance from the point of contact increases. The radius of the stressed zone predicted by both contact analysis schemes does not match the radius of the residual stress field around a Vickers indentation detected by the NIR polariscope.

For $\phi = 90°$, the stresses σ_{rr} and $\sigma_{\theta\theta}$ are equal and opposite. The NIR polariscope is a through-thickness tool, and examination of the predicted stresses at a different angle ϕ is instructive. The predicted stresses are plotted in Figure 9-9 for $\phi = 75°$.

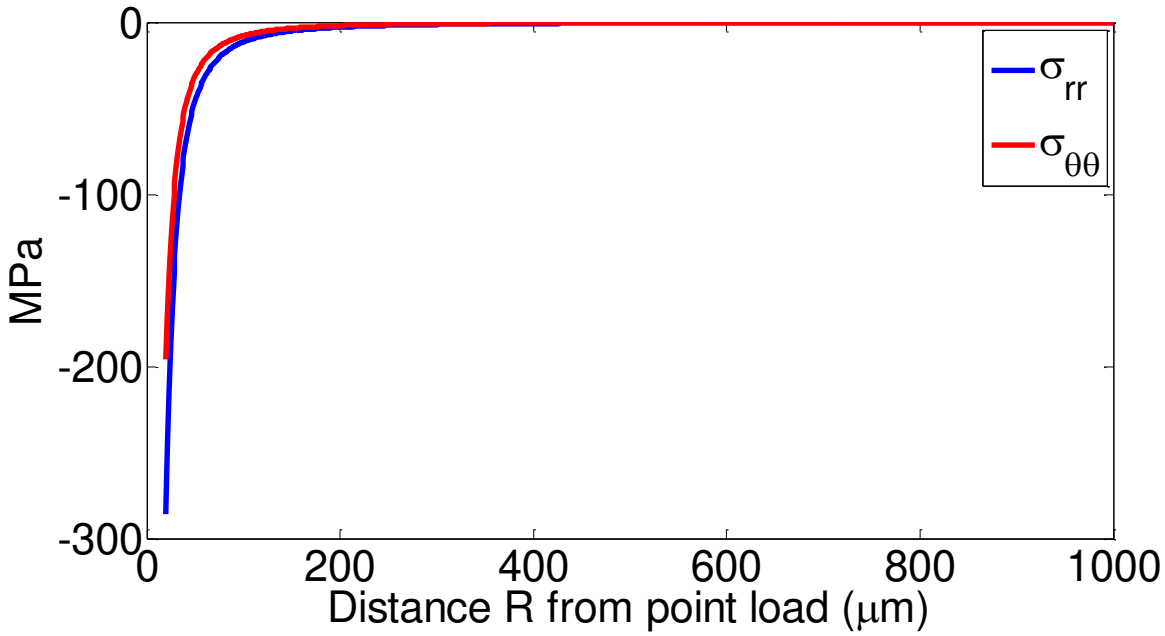

(a)

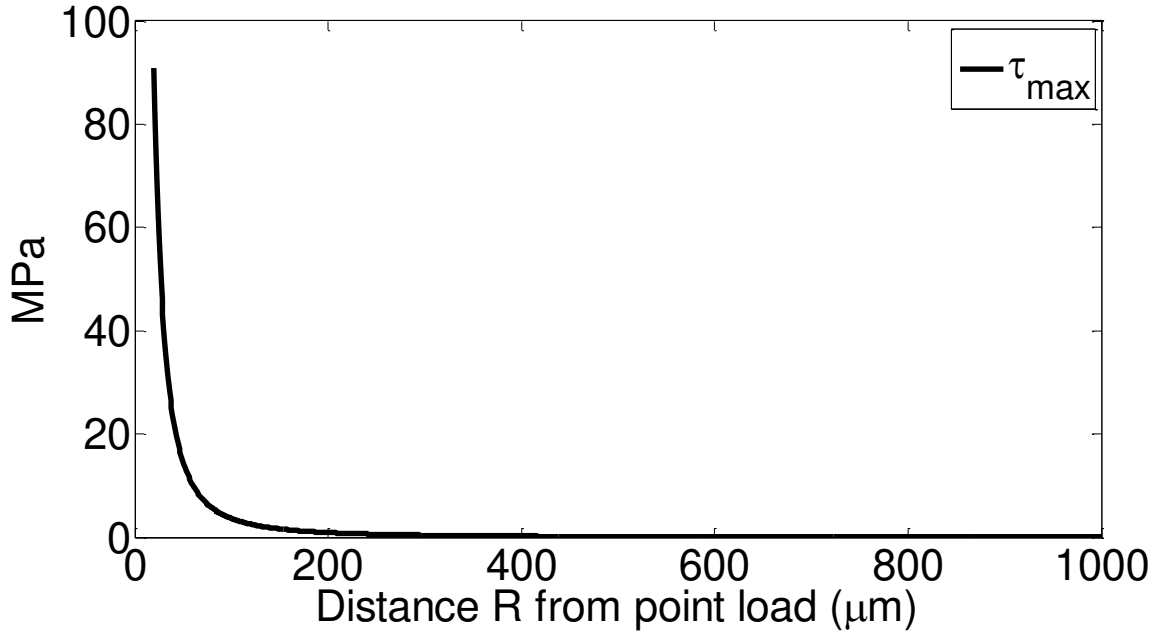

(b)

Figure 9-9: (a) σ_{rr} and $\sigma_{\theta\theta}$, (b) τ_{max} fields (MPa) vs. R (μm) predicted by the Boussinesq solution (ϕ = 75º).

While the stress fields have been altered, the diameter of the area affected remains smaller than 150 μm. The stress fields measured around individual Vickers indentations by the NIR polariscope were 1200 μm in diameter. This discrepancy of an order of magnitude is not easily dismissed.

As the indentation is created in the wafer, the contact point ceases to be on the surface of the wafer and moves into the interior. Mindlin derived the solution of a force at a point in the interior of a semi-infinite solid in 1936 [63]. This solution provides a more accurate representation of the final location of the contact point. The coordinate system through which this solution is defined is shown below in Figure 9-10.

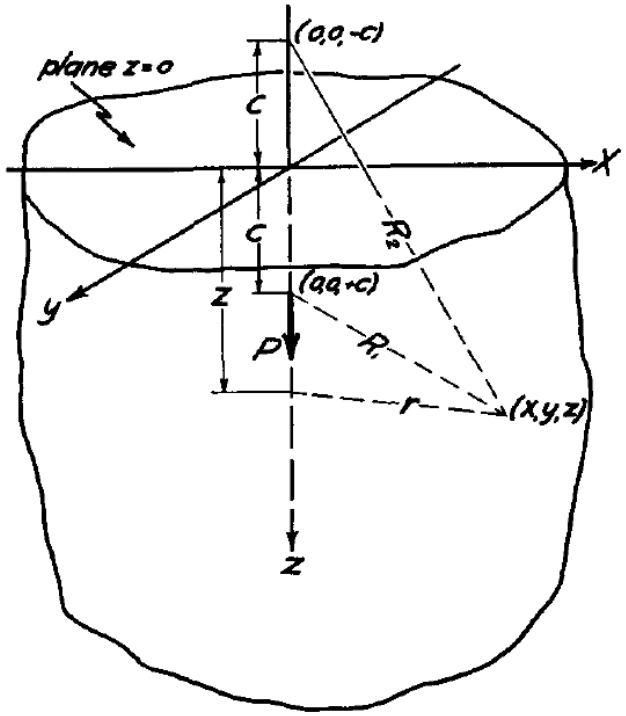

Figure 9-10: Coordinate system and variables used in Mindlin solution. [63]

Mindlin's solution was obtained by superposition of nuclei of strain for an unlimited solid. The semi-infinite solid is considered bound by the plane $z = 0$ as shown

in Figure 9-10. The normal force P is applied at a point (0, 0, +c) and acts in the positive z direction. A transformation to symmetrical cylindrical coordinates yields expressions for the displacements and stresses caused by the normal force P. These solutions are quite lengthy and are not reproduced here. Figure 9-10 illustrates the stress profile predicted on the surface of the silicon wafer using Mindlin's solution.

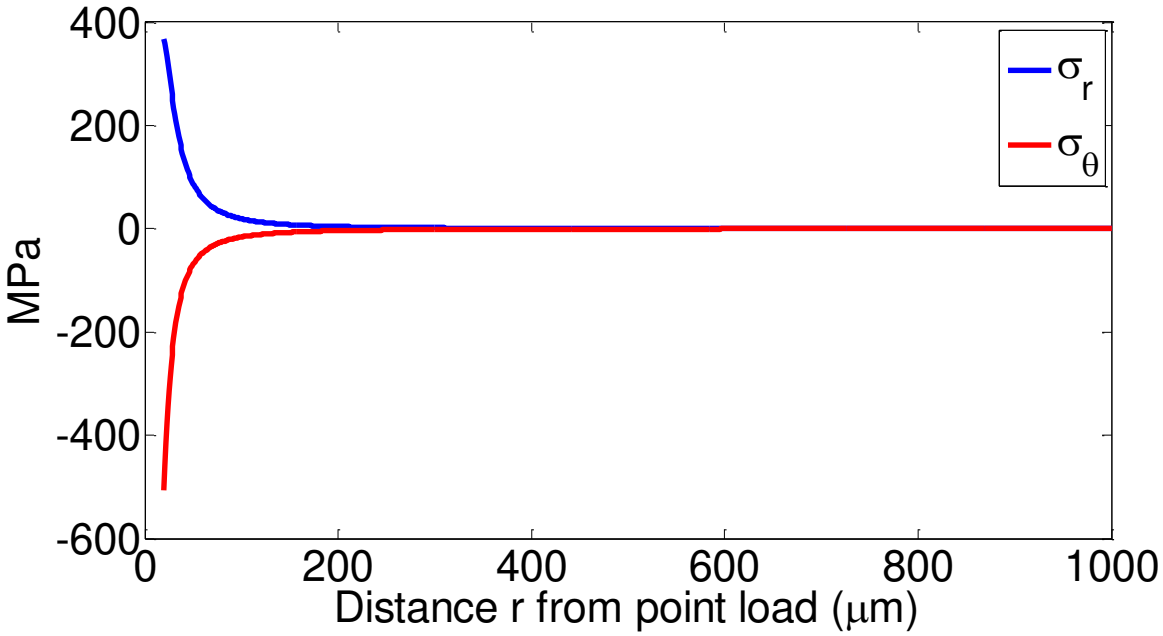

Figure 9-11: σ_r and σ_θ stresses (MPa) vs. r (μm) predicted by Mindlin solution.

The stress profile predicted by the Mindlin solution is similar to the stress profiles generated by Hertzian contact analysis and the Boussinesq solution of a point load on a surface. While the three theoretical stress fields agree with each other, none match the radius of the residual stress field generated by the Vickers indentation in the silicon wafer as measured by the NIR polariscope.

Research performed by Lucazeau in 1997 uncovered similar results using micro-Raman spectroscopy [64]. Boussinesq analysis of a 1 N Vickers indentation in a 1 μm

thick silicon layer predicted stress magnitudes of 250 – 650 MPa at a distance R = 10 μm from the load point, but all stresses had dropped to 8 MPa or lower at R = 100 μm. Micro-Raman analysis around the indentations revealed evidence of phase changes in the silicon and residual stresses much higher than predicted by contact mechanics. The tentative proposal to explain this difference noted displaced material in a "pileup region" immediately surrounding the indentation. Lucazeau hypothesized that areas of elastic displacement remain unrelieved and continue to exert stress on the aforementioned displaced material in the "pileup region." The exact mechanism governing the phase changes and residual stresses remains unknown, however.

Derivation of a new solid mechanics relationship solving the discrepancy between the experimental results and linear elastic theory is a complex problem outside the scope of this research. Wu and others have observed the material removal behavior of silicon changing between ductile and brittle under varying conditions [65-66]. The X-ray diffraction performed in Lucazeau's research also uncovered evidence of phase transformations to an amorphous state after indentation [64]. This behavior and the failure of linear elastic fracture mechanics to explain the residual stress fields measured experimentally support a complex relationship governing residual stresses in crystalline silicon.

9.3 Conclusions

Grain boundary theory confirms the residual stresses at grain boundaries measured by the NIR polariscope. Theoretical analysis with contact mechanics supports the experimentally determined magnitude of the residual stresses surrounding Vickers

indentations, but the diameter of the residual stress field measured by the NIR polariscope is larger than predicted by any contact mechanics solution. Prior experimental evidence has indicated phase changes and residual stresses higher than predicted by models. This prior work and the experimental results in this thesis indicate a complex and multi-faceted relationship governing the formation of residual stresses in silicon.

CHAPTER 10
DISCUSSION

Prior research conducted by Zheng, He, and Li found the NIR polariscope to be an effective tool for non-destructive evaluation of PV silicon. However, the poor resolution of the NIR camera in the polariscope severely limited studies of local stress phenomena. Replacement of the camera improved spatial resolution from 200 µm to 18 µm. This improvement in capability opened new possibilities, including investigation of stress concentrations.

Stress concentrations in silicon are created in a variety of ways. Grain boundaries in silicon are the most common source of stress concentrations. The improved spatial resolution of the NIR polariscope allowed for the examination of these grain boundaries. Initial inspection of grain boundaries with the new camera detected grain boundary stress levels higher than those in grain interiors. These results are shown in Figure 10-1.

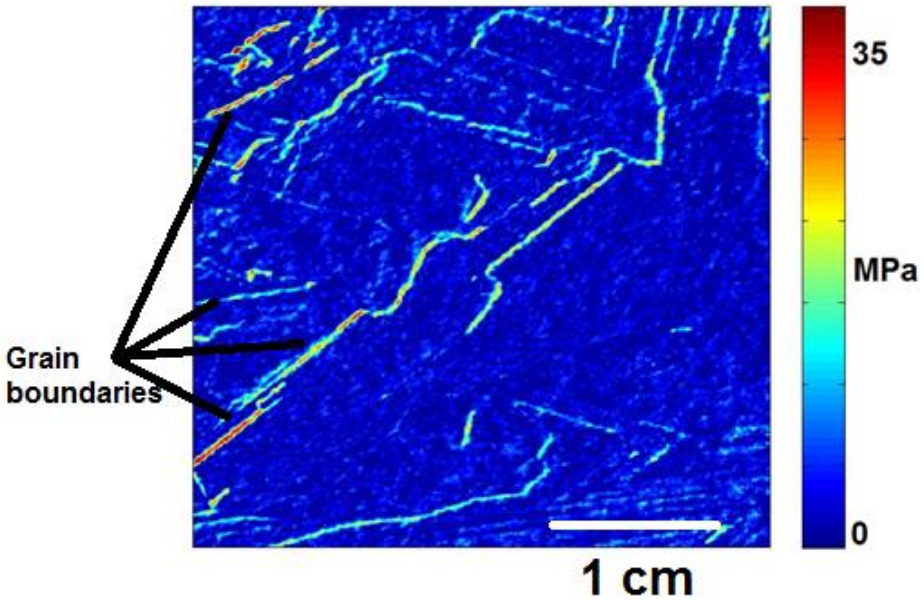

Figure 10-1: τ_{max} stress map of several grain boundaries in mc-Si wafer

Accurate determination of residual stresses in multicrystalline silicon wafers such as the one in Figure 10-1 poses three unique problems. First, the stress optic coefficient of silicon for evaluating maximum shear stress varies with crystallographic orientation. Thus, the crystallographic orientation of each grain in a multicrystalline wafer should be determined and the correct stress optic assigned for the highest accuracy. Second, noise in the grain interiors can obstruct real data and corrupt stress separation processes. Finally, no suitable boundary conditions existed for the separation of stresses within a single grain. Noise accumulation when starting from the free boundary of a wafer to separate the stresses within an interior grain produced unacceptable results.

The first problem was addressed using NIR transmission intensity. NIR transmission images of multicrystalline wafers show bright grains, dark grains, and a wide range of transmission intensity between the two extremes. The hypothesis that this difference in transmission intensity is related to crystallographic orientation was proposed and investigated. Figure 10-2 shows the NIR transmission image of a representative multicrystalline silicon sample.

Figure 10-2: NIR transmission image of multicrystalline silicon wafer.

The transmission intensity of single-crystal p-type CZ wafers of known orientation was measured for a baseline comparison. X-ray diffraction (XRD) was also performed on several grains to verify a relationship between transmission intensity and crystallographic orientation. The XRD and NIR transmission results supported the conclusion that grains with [111] crystallographic orientation are darkest, while grains with higher-order orientations such as [311] and [344] are brightest. An investigation of planar atomic density revealed a relationship between planar atomic density and NIR transmission intensity. This relationship is shown in Figure 10-3.

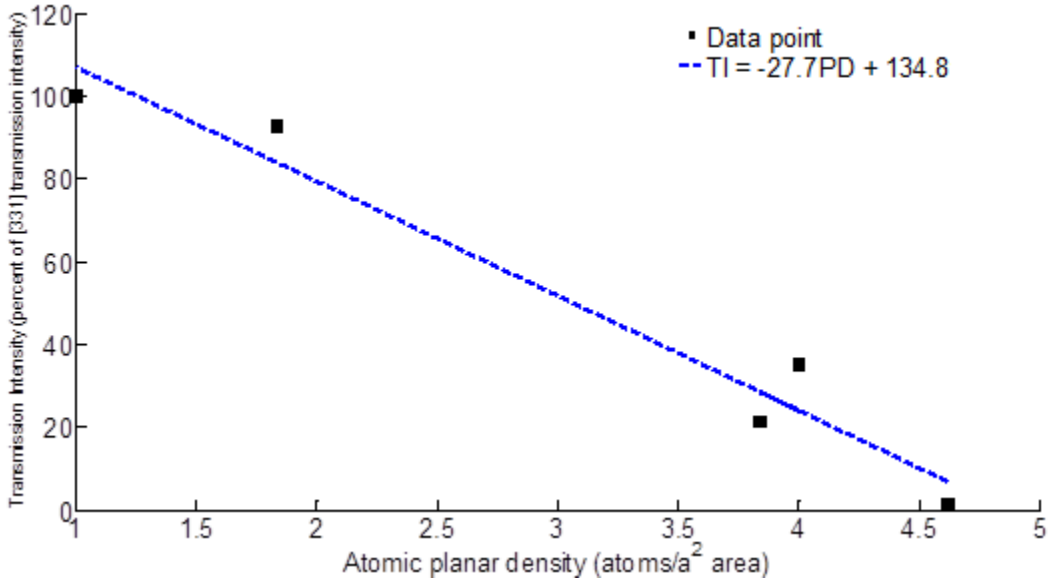

Figure 10-3: Transmission intensity (% of brightest measured grain) vs. atomic planar density (atoms/area).

Crystallographic orientations can be assigned based on NIR transmission intensity. Previous evaluation of multicrystalline silicon wafers used one stress optic coefficient for the entire wafer areas. Appropriate stress optic coefficients can now be assigned to individual grains, increasing the accuracy of stress evaluation.

The second problem was addressed by switching to the Ramji and Ramesh 10-step algorithm for data acquisition. The 10-step algorithm was found to reduce isoclinic oscillation between $-\pi/4$ and $\pi/4$ by 60% when compared to the previously used Patterson and Wang algorithm. This reduction in unpredictable isoclinic behavior lowered noise levels in the evaluated isoclinic parameter. Noise levels were further reduced by smoothing processes. While spatial averaging is quicker and less computationally expensive, least-squares RMS smoothing was found to be the most accurate. After smoothing, "streak formation" during stress separation no longer obliterates legitimate stress phenomena.

The final problem was solved with the discovery of a new boundary condition and the adaptation of the shear difference integration method to a quality-guided process. Points at which τ_{max} levels are found to be zero may contain equal principal normal stresses. These points are known as isotropic points. However, isotropic points are accompanied by a very particular isoclinic behavior. The absence of this behavior around a zero-stress point indicates that the normal stresses at that point are also zero. If all normal stresses at a point are known to be zero, that point is an acceptable boundary condition for the stress separation process. The shear-difference stress separation algorithm was then adapted to a quality-guided scheme such that noisy areas in the domain are evaluated last, minimizing noise propagation. This scheme also allows for the evaluation of an entire area from one starting point. Thus, individual grains in a multicrystalline wafer may now be integrated from a zero-stress point within the grain.

Once all of these problems had been addressed, the behavior of grain boundaries and their interaction with other local stresses could be examined. Vickers indentations

were chosen as a method of inducing a predictable stress concentration in the vicinity of grain boundaries. 2 N Vickers indentations were placed in an etched single-crystal p-type [100] wafer. These indentations created stress fields which were on average 1253.3 µm in diameter and had a maximum τ_{max} of 22.3 MPa. Moreover, grouping indentations in arrays was found to produce a multiplying effect which created a larger stress field around the entire array. The relationship between indentation proximity and the size of the stress field around the array is shown below in Figure 10-4.

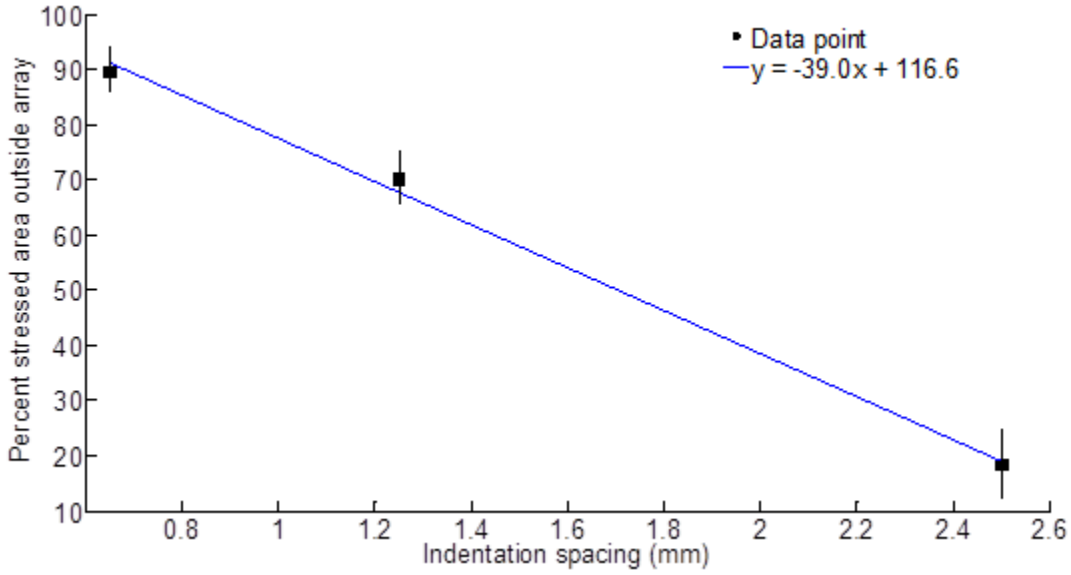

Figure 10-4: Percent of stressed area outside array vs. indentation spacing (mm).

A similar relationship was found for the increase in τ_{max} in the high-stress zone surrounding the indentation array.

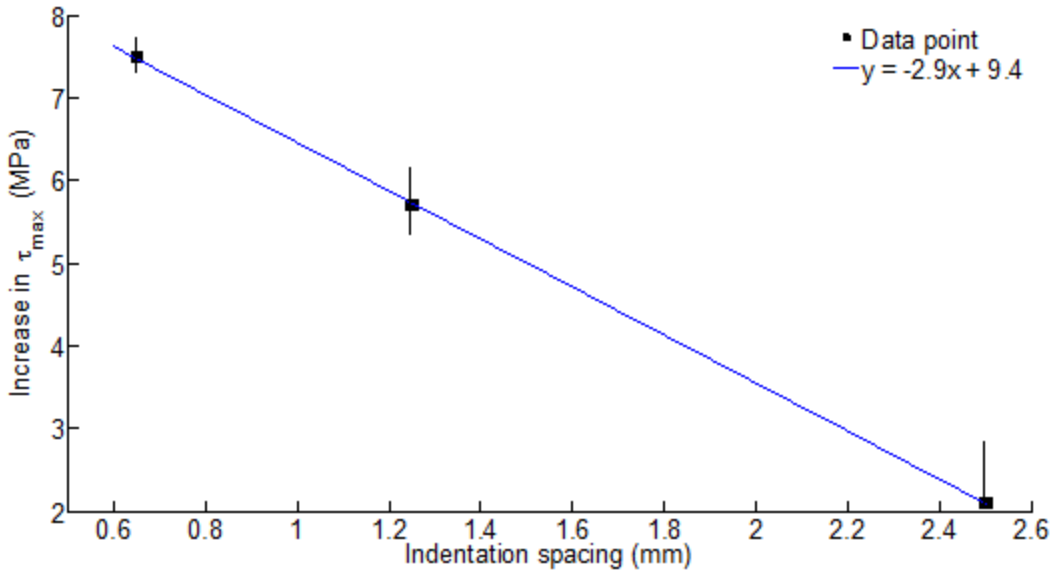

Figure 10-5: Increase in residual stress (MPa) vs. indentation spacing (mm).

Figures 10-4 and 10-5 illustrate the importance of detecting stress concentrations. Stress concentrations clustered together can affect areas significantly larger than the size of the group, compromising the mechanical integrity of the sample.

The stresses around Vickers indentations and around grain boundaries raise interest in interactions between the two. 2 N Vickers indentations were placed within 300 µm of grain boundaries to investigate these interactions, and the stresses around the indentations and grain boundaries were evaluated. The stress fields around the Vickers indentations were confined to the grain in which they were placed. These stress fields spread to the grain boundaries, but were arrested by the grain boundaries and did not progress into neighboring grains.

The grain boundary stresses were altered by the placement of Vickers indentations within the grain. Maximum shear stresses in the grain boundaries were found to consistently change by a magnitude of about 20 MPa. However, the shear stress

in some grain boundaries increased while others decreased. This behavior is believed to be related to differences in stress orientation in grain boundaries. Thus, indentation placement will sometimes increase the maximum shear stress $|\sigma_1 - \sigma_2|$, while in other cases the difference will decrease. The stress changes at the grain boundaries were also found to be independent of the number of indentations placed and the distance between the indentation and the grain boundary.

Grain boundary theory predicts shear stresses of 30 MPa or higher at silicon grain boundaries. This agrees with the experimental results from the NIR polariscope, which consistently detected maximum shear stresses of at least 25 MPa at grain boundaries in cast multicrystalline wafers. Stresses around the Vickers indentations are harder to explain. Hertzian contact analysis, the Boussinesq solution for a point load on a semi-infinite half space, and the Mindlin solution for a point load in the interior of a material all predict stresses which drop below 10 MPa at a distance of 100 µm from the load point. This disagrees with the experimental analysis from the NIR polariscope, which consistently found raised stress fields with a radius of 500 µm or greater. The discrepancy between theory and experimental results is for now unexplained. Prior research has found that silicon behaves in somewhat unpredictable ways when stressed, and experimentally determined stresses do not always match theoretical predictions.

The difference between theory and experimental results for the stress fields surrounding the indentations and the lack of a relationship between the stress change at a grain boundary and the number or location of indentations indicates a complex relationship governing stresses in silicon and their interaction. These relationships warrant further scrutiny.

CHAPTER 11
CONCLUSIONS

The conclusions of this thesis may be summarized as follows:

1. NIR transmission intensity through silicon is related to atomic planar density. X-ray diffraction and NIR transmission results support a linear relationship $TI = -30PD + 135$, where TI is normalized to a percentage of the brightest measured grain and PD is measured in atoms/area.

2. The relationship between NIR transmission intensity and atomic planar density allows for crystallographic orientation identification based on NIR transmission. Grains separated by transmission intensity can be assigned proper stress-optic coefficients for stress evaluation.

3. The 10-step phase-shifting algorithm is superior to the Patterson and Wang 6-step algorithm. The 10-step algorithm produces less noise in evaluated isoclinics and reduces isoclinic oscillation between $-\pi/4$ and $\pi/4$ by 60%. It is also more likely to correctly resolve stresses of zero magnitude.

4. Noise in the isoclinic parameter is a primary contributor to noise accumulation during the shear difference stress separation process. Smoothing isoclinic values resulted in a 70% reduction in noise levels after stress separation for a multicrystalline silicon beam.

5. The inherent ambiguity in τ_{max} values of zero was resolved. Points at which the principal normal stresses are equal and non-zero are accompanied by a

characteristic isoclinic behavior. The absence of this isoclinic behavior indicates a value of zero for both principal normal stresses.

6. Points at which all stresses are zero can be used as acceptable boundary conditions for stress separation with the shear difference integration process.

7. Shear difference integration was adapted to a quality-guided process which can use points of zero stress as a boundary condition. This enables the separation of an entire spatial domain from one starting point, and enables the separation of specific areas in the wafer interior which cannot be accurately evaluated using a free boundary as the integration starting point.

8. Residual stresses surrounding 2 N Vickers indentations in CZ wafers were found to reach an average of 22 MPa and affect an area 1.3 mm in diameter.

9. Indentations placed in closely spaced arrays generated secondary stress fields around the array. The size of the stress field around the array follows the relationship $A = 39x + 117$, where A is the percentage of the stress field outside the array boundaries and x is the indentation spacing. The increase in residual stress magnitude follows the relationship $\tau_{max} = -3x + 9.5$, where τ_{max} is the stress increase in MPa and x is the indentation spacing.

10. Grain boundaries in multicrystalline wafers contain stresses on the order of 30-35 MPa, while residual stress levels in grain interiors rarely rise above 8 MPa.

11. Placement of 2 N Vickers indentations near grain boundaries resulted in a 15-20 MPa change in the stress state of the grain boundary. This behavior was unaffected by the number of indentations placed or the distance between the indentation and the grain boundary.

12. The stress fields caused by the Vickers indentations were arrested by the grain boundaries and did not extend into neighboring grains.

13. Grain boundary stresses measured by the NIR polariscope agree with grain boundary theory. The magnitude of the stress fields surrounding the Vickers indentations is explained by contact mechanics, but the diameter of the stress fields is larger than predicted by analytical models.

APPENDIX A: ALIGNMENT OF THE NIR POLARISCOPE

Proper alignment of the components of the NIR polariscope is critical to accurate results. An aperture is used to reduce the tungsten lamp to an approximate point source. From this point, the first lens is placed such that the aperture is at the focal point. The light is now collimated after passing through the first lens, and the second lens can be placed any desired distance away such that there is room for the sample fixture between the lens pair. Once the second lens has been placed, the camera is positioned so the focal point of the second lens is coincident with the camera's aperture opening. From this point, the polarizer and input quarter waveplate can be placed between the light source and the first lens, and the analyzer and output quarter waveplate can be placed between the second lens and the camera. The positioning of the polarizers and waveplates is less sensitive. These optics may be located anywhere such that the beam passes through without being impeded by the edges of the mounting ring. The final setup should resemble Figure A-1.

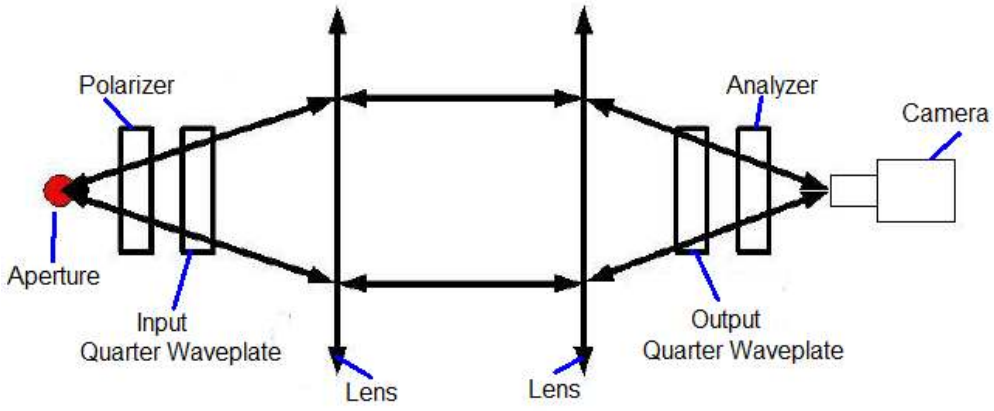

Figure A-1: Schematic of light path through properly aligned polariscope.

Light passing through crossed polarizers which is not perfectly collimated produces a characteristic pattern known as an extinction cross. Figure A-2 is an image of this phenomenon.

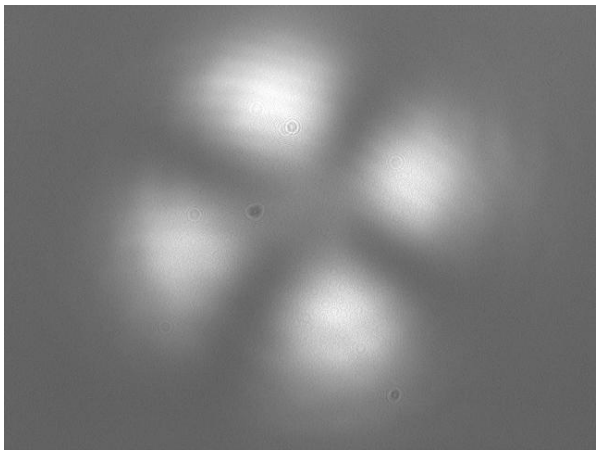

Figure A-2: Extinction cross created by light passing through crossed polarizers.

Waveplates can be used to nullify the extinction cross. During the phase shifting process, the angles between the polarizers and the waveplates must be carefully maintained, or the cross pattern in Figure A-2 will create systemic error in the stress analysis. Figure A-3 is the phase map of a single-crystal CZ wafer. The input waveplate was 5º out of alignment for each step in the phase shifting process.

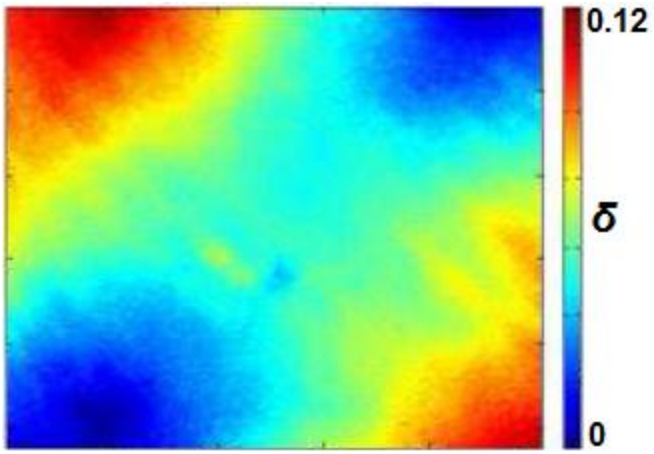

Figure A-3: Phase map of CZ wafer, 5º misalignment in input quarter waveplate.

Proper evaluation of the orientation of the polarizers and waveplates eliminates the extinction cross phenomenon seen in Figures A-2 and A-3. Any error that remains in the τ_{max} map may be subtracted out if desired.

The angular misalignment in the waveplates and polarizers when using the Patterson and Wang method was analyzed by He [15]. Ramji and Prasath compared several phase shifting methods and found that the 10-step phase shifting algorithm was not significantly affected by angular misalignments of up to ±2º [67]. Adoption of the 10-step method thus greatly reduces the effects of angular misalignments in the NIR polariscope.

APPENDIX B: RESIDUAL STRESS CORRELATION WITH SURFACE CONDITION AND GROWTH RATE

The most common method of wafering silicon ingots is wire sawing, illustrated in Figure 2-6. Photovoltaic industry standard has gravitated to two types of wire sawing: slurry-cut, in which the wire is dragged through a slurry of abrasive particles before passing through the ingot, and fixed abrasive diamond wire, in which diamond particles are permanently affixed to the wire prior to the sawing process. Wu studied the differences in wafers cut with the two methods and found them to be comparable in many respects [66]. Key differences included surface morphology, prevalence of microcracks within the wafer subsurface, and residual stress levels. A comparison of residual stresses in wafers cut by slurry sawing and fixed abrasive diamond wire sawing is shown below in Figure B-1.

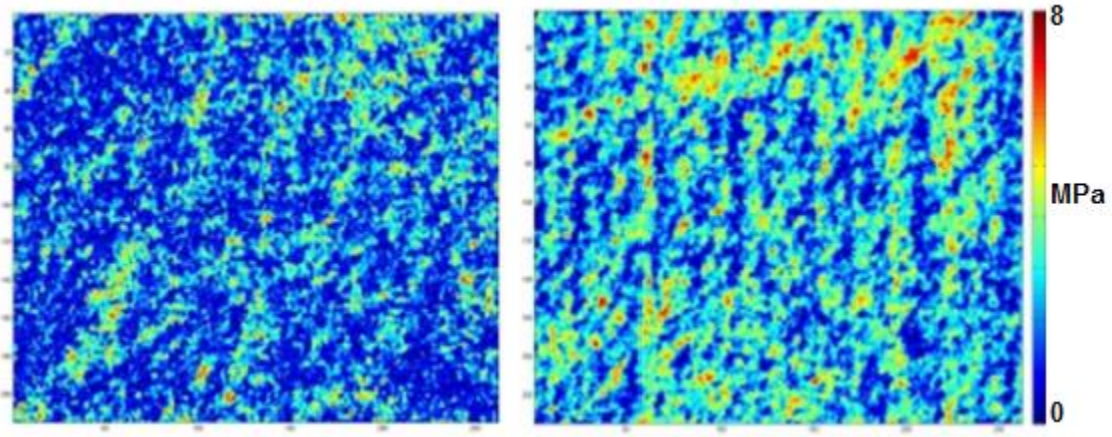

(a) (b)

Figure B-1: Residual τ_{max} stresses in a 15mm x 15mm area of (a) slurry-sawn and (b) diamond wire sawn wafers. [66]

While the average residual stress values across the entire surface of the wafers were comparable between the two wafering methods, streaks of high stress are clearly visible in the wafer cut with fixed abrasive diamond wire. Moreover, the wafers cut with fixed abrasive diamond wire exhibited significantly more variation in fracture strength, as shown in Figure B-2:

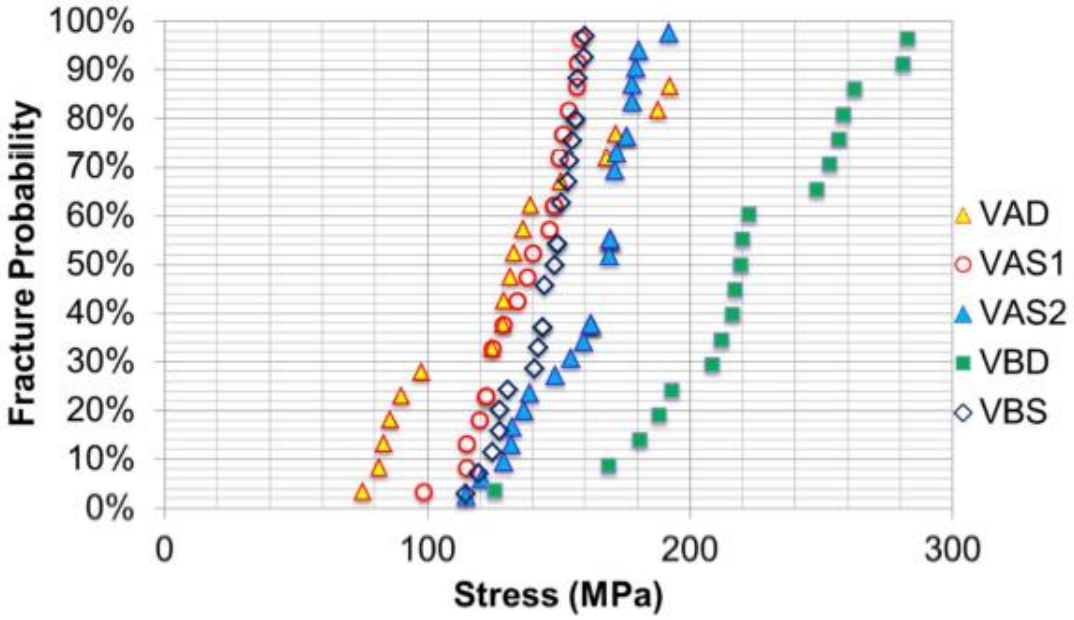

Figure B-2: Fracture probability in four line bending tests. [66]

VAD and VBD represent wafers from Vendor A and Vendor B cut with fixed abrasive diamond wire, while VAS1, VAS2, and VBS indicate wafers cut with a slurry process.

Further research by Yang et al. on the relationship between residual stresses and fracture strength in silicon found that the fracture strength of fixed abrasive diamond wire sawn wafers was highly dependent upon physical orientation when using four line bending tests [22]. Wafers tested with four line bending parallel to the cutting direction exhibited lower fracture strength than wafers tested with bending perpendicular to the cutting direction. The difference is presented graphically in Figure B-3.

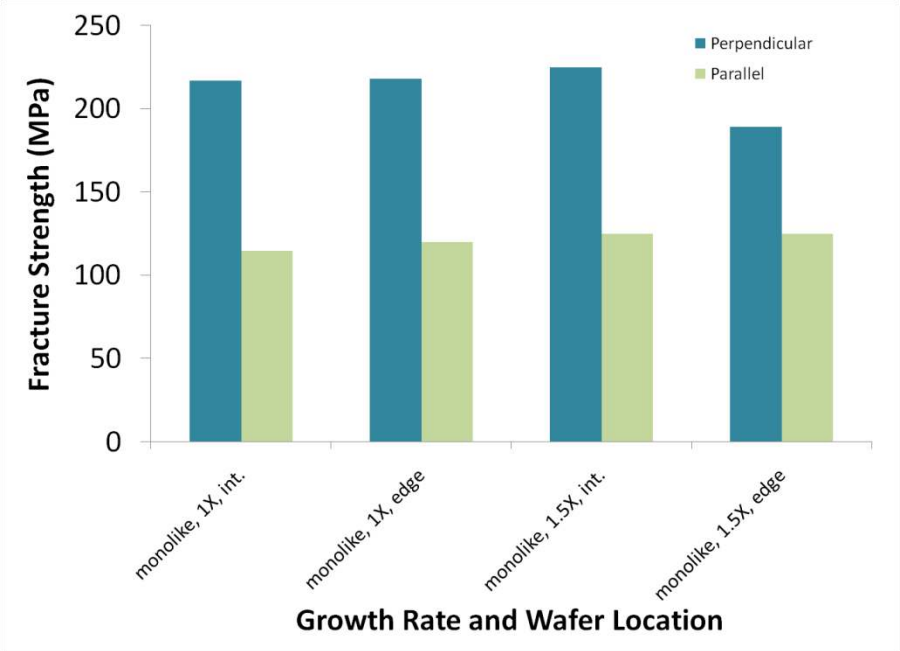

Figure B-3: Fracture strength of fixed diamond wire sawn wafers tested with four line bending parallel and perpendicular to cutting direction. [22]

Regardless of growth rate or location in the silicon brick, fracture strength tested perpendicular to the sawing direction is consistently 50-80% higher than parallel. The source of this discrepancy was explained by Yang as a product of the microcracks generated by the fixed abrasive diamond wire sawing process and the residual stresses generated such as the ones in Figure B-1.

If the stresses seen in Figure B-1 are a product of the diamond wire sawing process and contribute to the lower fracture strength of the wafers, removal of these stresses would correspond to an increase in fracture strength. An etching process was used to remove 5 μm from each face of the wafer to test the hypothesis that the residual stresses measured were surface stresses. The pre-etch and post-etch residual τ_{max} results are shown below in Figure B-4.

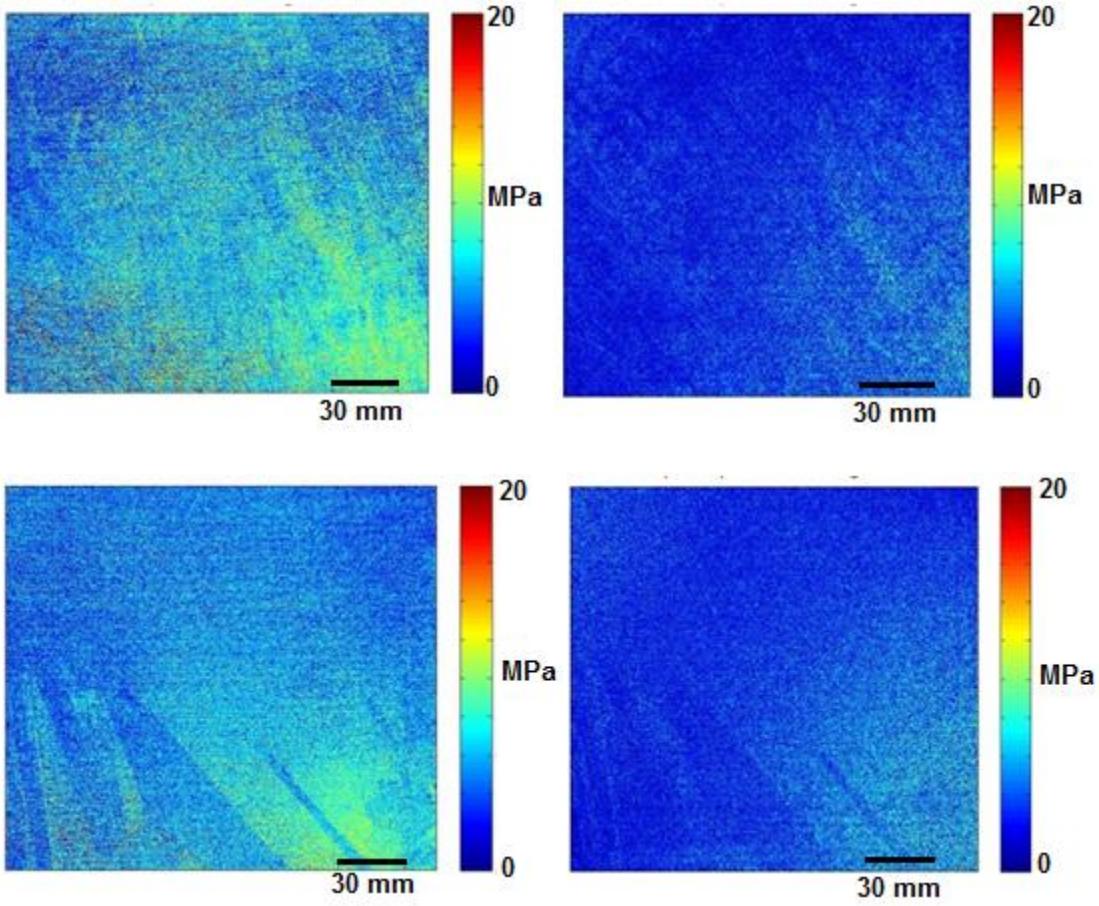

Figure B-4: Residual τ_{max} stress maps for cast mono-like (a) pre-etch and (b) post etch; cast multicrystalline (c) pre-etch and (d) post-etch. [22]

Residual stresses have been considerably reduced by the etching process. The average value of τ_{max} over the entire wafer was lowered from 5.6 to 3.2 MPa for the mono-like wafers and from 6.7 to 2.9 for the multicrystalline wafers. Moreover, the "streaks" along the cutting direction seen in Figure B-1 are now less noticeable. This reduction in residual stress is correlated with an increase in fracture strength. Figure B-5 demonstrates the trend.

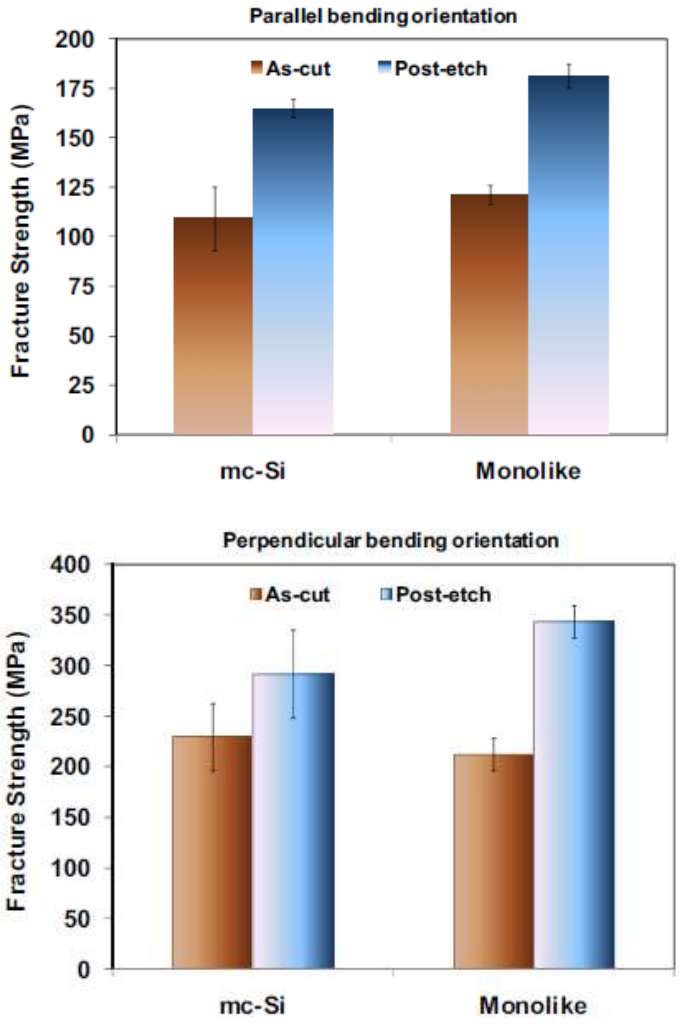

Figure B-5: Fracture strength before and after etching. [22]

Residual stress levels have decreased while fracture strength has increased for all wafers in both testing orientations. Such a correlation is intuitive and lends credence to the hypothesis that residual stresses in fixed abrasive diamond wire sawn wafers such as seen in Figure B-1 are close to the wafer surface, and removal of these stresses has a beneficial effect on the mechanical properties of the wafer.

Removal of 5 μm also served to lower the residual stresses related to differing growth rate. A comparison of multicrystalline wafers revealed a noticeable difference

between the measured residual stress levels of wafers grown at normal rate and wafers grown at twice normal rate. Figure B-6 shows the difference.

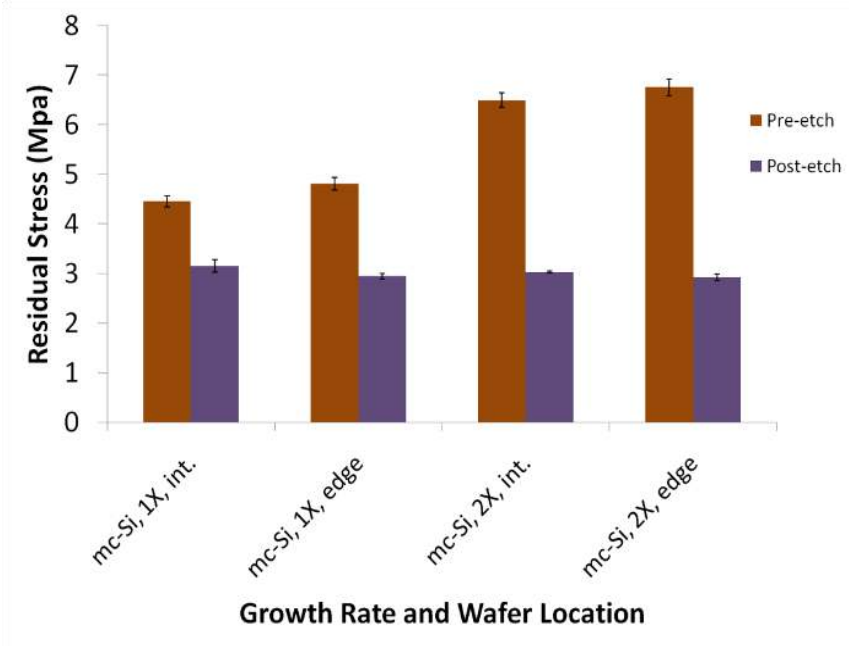

Figure B-6: Residual stresses before and after etching of wafers grown at a normal rate and twice the normal rate. [22]

The same wafers were also shown to have a lower fracture strength when grown at twice the normal rate, as illustrated below in Figure B-7.

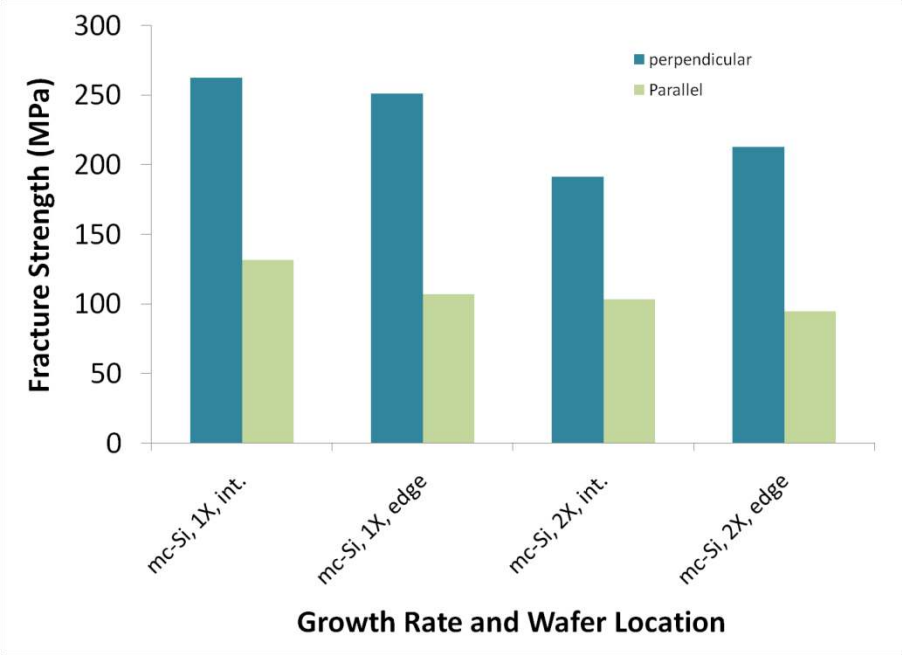

Figure B-7: Fracture strength of wafers grown at normal rate and twice normal rate. [22]

Note that the 1X growth wafers have higher fracture strengths (in both testing orientations) and lower residual stress than their 2X growth rate counterparts. This correlation between higher fracture strength and lower residual stress is again intuitively correct. A higher growth rate than normal is also expected to result in more pronounced thermal gradients throughout the wafers, resulting in higher residual stresses and lower fracture strengths.

REFERENCES

1. D. Brewster, "On the communication of the structure of doubly refracting crystals to glass, muriate of soda, flour spar and other substances by mechanical compression and dilatation," *Phil. Trans. Roy. Soc.*, vol. 105, no. 60, pp. 156-178, 1816.

2. F. Neumann, "Die Gesetze der Doppelbrechung des Lichtes in komprimierten oder ungleichformig erwarmten unkrystallinischen Korpern," *Abh. d. Kon. Akad. d. Wissenschaften zu Berline, Pt. II*, 1-254, 1841.

3. J. Maxwell, "On the equilibrium of elastic solids," *Trans. Roy. Soc. Edinb.*, vol. 20, pp. 87-20, 1853.

4. E. Coker and L. Filion, *A Treatise on Photoelasticity.* New York: Cambridge University Press, 1931.

5. L. Bergmann and E. Fues, *Naturwiss,* vol. 24, p. 492, 1936.

6. J. Dally and W. Riley, *Experimental Stress Analysis*. United States of America: McGraw-Hill, Inc, 1965.

7. W. Bond and J. Andrus, "Photographs of the stress field around edge dislocations," *Phys. Rev.*, vol. 101, p. 1211, 1956.

8. S. Lederhandler, "Infrared studies of birefringence in silicon, "*J. of Appl. Phys.*, vol. 30, no. 11, pp. 1631-1638, 1959.

9. R. Dixon, "Photoelastic properties of selected materials and their relevance for applications to acoustic light modulators and scanners," *J. of Appl. Phys.,* vol. 38, no. 13, pp. 5149-5152, 1967.

10. H. Kotake and S. Takasu, "Quantitative measurement of stress in silicon by photoelasticity and its application," *J. Electrochem. Soc.,* vol. 171, no. 1, pp. 179-184, 1980.

11. K. Date, "Stress measurement with high sensitivity in wafers using infrared photoelasticity," in *Advances in Electronic Packaging,* W. Chen and H. Abe, Eds. New York: American Society of Mechanical Engineers, 1992, pp. 985-989.

12. H. Liang et al, "Two-dimensional state of stress in a silicon wafer," *J. of Appl. Phys.,* vol. 71, no. 6, pp. 2863-2870, 1992.

13. Y. Niitsu, T. Ikeda, and T. Tadokoro, "Accuracy evaluation of stress measurement in silicon crystal by microscopic Raman spectroscopy," in *International Electronics Packaging Conference,* San Diego, CA, 1993, pp. 255-259.

14. T. Zheng, "A Study of Residual Stresses in Thin Anisotropic (silicon) Plates," Ph.D. dissertation, School of Mech. Eng., Georgia Institute of Technology, 2000.

15. S. He, "Near Infrared Photoelasticity of Polycrystalline Silicon and its Relation to In-plane Residual Stresses," Ph.D. dissertation, School of Mech. Eng., Georgia Institute of Technology, 2005.

16. F. Li, "Study of Stress Measurement Using Polariscope," Ph.D. dissertation, School of Mech. Eng., Georgia Institute of Technology, 2010.

17. C. V. Raman, "A new radiation," *Ind. J. of Phys.*, vol. 2, pp. 387-398, 1928.

18. G. Placzek, E. Teller, "Die rotationnstruktur der Ramanbanden mehratomiger molekule," *Z. Phys.*, vol. 81, pp. 209-258, 1933.

19. A. Schönecker, L. J. Geerligs and A. Müller, "Casting Technologies for Solar Silicon Wafers: Block Casting and Ribbon-Growth-on Substrate," *Diffusion and defect data, Part B: Solid state phenomena,* vol. 95, pp. 149-158, 2004.

20. J.P. Kalejs, B.H. Mackintosh, and T.Surek, "High-speed EFG of wide silicon ribbon," *J. of Cryst. Growth,* vol. 50, no. 1, pp. 175-192, 1980.

21. C. Yang et al., "On the residual stress and fracture strength of crystalline silicon wafers," *Appl. Phys. Lett.*, vol. 102, no. 021909, 2013.

22. J.P. Kalejs, "Modeling contributions in commercialization of silicon ribbon growth from the melt," *J. of Cryst. Growth,* vol. 230, no. 1-2, pp. 10-21, 2001.

23. W. S. Radeker, S. Cunningham, "A Hierarchy of Slurry Reprocessing Options," in *The Materials, Metals, and Materials Society 139th Annual Meeting and Exhibition,* Seattle, 2010, pp. 561-564.

24. V. Garcia, "Effect of Dislocation Density on Residual Stress in Edge-Defined Film-Fed Growth Silicon Wafers," M.S. thesis, School of Mech. Eng., Georgia Institute of Technology, 2008.

25. K. Skenes, F. Li, and S. Danyluk, "Analysis of residual stress in thin silicon wafers with an NIR polariscope," in *26th European PV and Solar Energy Conference and Exhibition*, Hamburg, 2011, pp. 2082-2085.

26. K. Skenes, R.G.R. Prasath, and S. Danyluk, "Measurement of Residual Stresses around Vickers Indentations on Silicon Surfaces via NIR Polariscope," in *28th European PV and Solar Energy Conference and Exhibition,* Paris, 2013, pp 242-245.

27. J. Maxwell, "A Dynamical Theory of the Electromagnetic Field," *Phil. Trans. of the Roy. Soc. of London*, Vol. 155, pp. 459-512, 1865.

28. F. Sears and M. Zemansky, *University Physics, 2nd edition*. Reading, MA: Addison-Wesley Publishing Company, Inc, 1955.

29. A. Redner, "Photoelastic measurements by means of computer-assisted spectral contents analysis," in *5th International Congress on Experimental Mechanics,* Montreal, Canada, 1984, pp. 421-427.

30. C. Quan, P. Bryanston-Cross, and T. Judge, "Photoelasticity stress analysis using carrier fringe and FFT techniques," *Opt. Lasers Eng.,* vol. 20, pp.135-140, 1993.

31. Y. Morimoto, Y. Morimoto Jr, and T. Hayashi, "Separation of isochromatics and isoclinics using Fourier transform," *Exp. Mech.,* vol. 18, no. 5, pp. 13-18, 1994.

32. T. Ng, "Photoelastic stress analysis using an object step-loading method," *Exp. Mech.,* vol. 37, no. 3, pp. 137-141, 1997.

33. F. Hecker and B. Morche, "Computer-aided measurement of relative retardations in plane photoelasticity," in *Experimental Stress Analysis.,* H. Wieringa, Ed. Hingham, MA: Kluwer Academic Publishers, 1986, pp. 535-543.

34. E. Patterson and Z. Wang, "Advantages and disadvantages in the application of phase-stepping in photoelasticity," in *Applied Solid Mechanics,* vol. 4, A. Ponter and A Cocks, Eds. London: Elsevier Applied Science, 1991, pp. 358-373.

35. M. Ramji and K. Ramesh, "Whole field evaluation of stress components in digital photoelasticity – issues, implementation, and application," *Opt. Laser Eng,* vol. 46, no. 3, pp. 257-271, 2008.

36. R.G.R. Prasath, K. Skenes, and S. Danyluk, "Comparison of phase shifting techniques for measuring in-plane residual stresses in thin, flat silicon wafers," *J. of Elec. Mat.,* vol. 42, no. 8, pp. 2478-2485, 2013.

37. *The book of photon tools,* Oriel Instruments, Inc., 1999

38. S. He, T. Zheng, and S. Danyluk, "Analysis and determination of stress optic coefficients of thin single crystal silicon samples," *J. of Appl. Phys.*, Vol. 96 (6), pp. 3103-3109, 2004.

39. C. Reimann et al., "A new characterization tool for the investigation of the crystal structure of directionally solidified crystalline silicon," presented at the 5th International Workshop on Crystalline Solar Cells, Boston, MA, 2011.

40. E. Organick, *A FORTRAN IV Primer*. Reading, Massachusetts: Addison-Wesley, 1966.

41. G.M. Brown and J. L. Sullivan, "The computer aided holophotoelastic method," *Exp. Mech.,* vol. 30, pp. 135–144, 1990.

42. A. Ajovalasit, S. Barone, and G. Petrucci, "A method for reducing the influence of the quarter-wave plate error in phase-shifting photoelasticity," *J. Strain Anal. Eng. Design*, vol. 33, pp. 207–216, 1998.

43. M. Ramji and K. Ramesh, "Isoclinic parameter unwrapping and smoothening in digital photoelasticity," in *International Conference on Optics and Optoelectronics*, Dehradun, 2005.

44. M.J. Ekman and A.D. Nurse, “Completely automated determination of two-dimensional photoelastic parameters using load stepping,” *Opt. Eng.*, vol. 34, pp. 1845-1851, 1998.

45. N. Plouzennec, J.C. Dupre, and A. Lagarde, “Whole field determination of isoclinic and isochromatic parameters,” *Exp. Tech.*, vol. 23, pp. 30-33, 1999.

46. H. Aben, L. Ainola, and J. Anton, “Half-fringe phasestepping with separation of the principal stress directions,” *Proc. of the Estonian Acad. Sci. Eng.*, vol. 5, pp. 198-211, 1999.

47. J.A. Quiroga and A. Gonzalez-Cano, “Separation of isoclinics and isochromatics from photoelastic data using regularized phase-tracking technique,” *Appl. Opt.*, vol. 39, pp. 2931-2940, 2000.

48. D.C. Ghiglia and M.D. Pritt, *Two-Dimensional Phase Unwrapping: Theory, Algorithms and Software*. New York: Wiley-InterScience, 1998.

49. M. Ramji and K. Ramesh, “Quality aided isoclinic phase unwrapping in digital photoelasticity,” in *International Conference on Photonics*, Hyderabad, 2006.

50. M. Ramji and K. Ramesh, “Adaptive quality guided phase unwrapping algorithm for whole-field digital photoelastic parameter estimation of complex models,” *Strain*, vol. 46, pp. 184-194, 2010.

51. K. Skenes, R.G.R. Prasath, and S. Danyluk, “Polariscopy measurement of residual stresses in thin silicon wafers,” *Infrared Imaging, Hybrid Techniques and Inverse Problems, Volume 8 : Proceedings of the 2013 Annual Conference on Experimental and Applied Mechanics*, pp. 79-85, 2013.

52. M.M. Frocht, *Photoelasticity Vol. II*. New York, NY: John Wiley & Sons, Inc., 1948.

53. W.T. Read, *Dislocations in Crystals.* New York, New York: McGraw-Hill, Inc., 1953.

54. M. Meyers and K. Chawla, *Mechanical Metallurgy: Principles and Applications.* Englewood Cliffs, New Jersey: Prentice-Hall, Inc., 1984.

55. J.D. Eshelby, W.T. Read, W Shockley, “Anisotropic elasticity with applications to dislocation theory,” *Acta Metallurgica,* vol. 1, no. 3, pp. 251-259, 1953.

56. M.A. Hopcroft, W.D. Nix, and T.W. Kenny, "What is the Young's Modulus of Silicon?," *J. of Microelectromechanical Sys*, vol. 19, no. 2, pp. 229-238, 2010

57. J. Williams, *Engineering Tribology.* Oxford, New York: Oxford University Press, 1994.

58. A. Fischer-Cripps, *Nanoindentation, 3rd Edition*. Springer Science and Business Media, 2001.

59. P. Hess, “Laser diagnostics of mechanical and elastic properties of silicon and carbon films,” *Appl. Surf. Sci.*, vol. 106, pp.429-437, 1996.

60. *Synthetic Diamond - Emerging CVD Science and Technology*, K. Spear and J. Dismukes, Eds. New York: John Wiley & Sons, Inc., 1994.

61. L.D. Landau and E.M. Lifshitz, *Theory of Elasticity 3rd Edition*. Oxford, England: Butterworth Heinemann, 1986.

62. B.R. Lawn and M.V. Swain, “Microfracture beneath point indentations in brittle solids,” *J. of Mat. Sci.,* vol. 10, pp. 113-122, 1975.

63. R.D. Mindlin, “Force at a point in the interior of a semi-infinite solid,” *J. of Appl. Phys.*, vol. 7, pp. 195-202, 1936.

64. G. Lucazeau and L. Abello, “Micro-Raman analysis of residual stresses and phase transformations in crystalline silicon under microindentation,” *J. of Mat. Res.,* vol. 12, no. 9, pp. 2262-2273, 1997.

65. H. Wu, “Fundamental investigations of cutting of silicon for photovoltaic applications,” Ph.D. dissertation, School. of Mech. Eng., Georgia Institute of Technology, 2012.

66. H. Wu et al, “Analysis of slurry and fixed abrasive diamond wire sawn silicon wafers,” in *21st National Renewable Energy Laboratory Workshop,* Breckenridge, CO, 2011.

67. M. Ramji and R.G.R. Prasath, “Sensitivity of isoclinic data using various phase shifting techniques in digital photoelasticity towards generalized error sources,” Optics and Lasers in Eng,, vol. 49, pp. 1153-1167, 2011.